NLC “Academician E.A. Buketov Karaganda University”

Dyusembaeva A.N.

MATHEMATICAL MODELING OF WIND POWER PLANTS WITH COMBINED BLADES

Karaganda, 2024

UDC 510:621.3 (035.3)
LBC 22.1:32.8
D 98

Recommended for publication by the academic council
E. A. Buketov KarU
(Protocol No. 14 of 27.06. 2024)

Reviewers:

Doctor of Technical Sciences, professor of Sh. Ualikhanov Kokshetau University
S.M. Mukhamedin;

PhD, Associate Professor of E.Buketov Karaganda University
D.A. Afanasyev;

PhD, Associate Professor of E.Buketov Karaganda University
Zh.T. Kambarova.

D 98 **Dyusembaeva A.N.**

Mathematical modeling of wind power plants with combined blades: monograph. – Astana: Altyn Kitap, 2024 – 116 p.

ISBN 978-601-7611-21-7

For the first time, the monograph presents data on numerical modeling of wind power plants with combined blades. The features of modeling the turbulent flow around a combined element - a cylinder and a fixed blade - are taken into account. The universal aerodynamic quantitative dependence of wind turbines is obtained using a mathematical model, which is compared with experimental data obtained from experimental samples.

For students of higher educational institutions, teachers, undergraduates, PhD students of technical specialties and researchers.

This study was funded by the Science Committee Ministry of Science and Higher Education of the Republic of Kazakhstan (IRN AP14972704 " Numerical study of a new design of wind turbine blades with a horizontal axis of rotation").

UDC 510:621.3 (035.3)
LBC 22.1:32.8

ISBN 978-601-7611-21-7

CONTENTS

DEFINITIONS, DESIGNATIONS AND ABBREVIATIONS

In this monograph, the following terms are used with appropriate definitions:

A wind wheel is the working body of a wind power plant that is used to convert the kinetic energy of the incoming air flow into mechanical energy to rotate the axis of the wind generator.

A wind turbine is a device that converts wind energy into rotational motion.

The following designations and abbreviations are used in this monograph:

WPP	- wind power plant;
WW	- windwheel;
WT	-wind turbine;
WEUC	-wind energy utilization coefficient;
HAWT	-horizontal axis rotation wind turbine;
VAWT	-vertical axis rotation wind turbine;
RES	-renewable energy sources.

INTRODUCTION

Worldwide, interest in renewable energy sources is growing rapidly every year. The reason for this is the limited reserves of minerals and energy resources, as well as the high demand from the global economy for new types of energy sources. The main prerequisites for the development of alternative energy are the creation and provision of energy and environmental security, the preservation of ecology for the future generation.

The Republic of Kazakhstan is rich in territorial area, which in turn makes it beneficial for the development of alternative energy, including wind energy.

As is known, in most of the country (55%) there are wind flows with an average speed of 4-5 m/s, and in some areas the wind speed reaches up to 10 m/s. The presented data are an excellent prospect for the country's wind energy industry, as well as for replacing existing energy facilities. Separately, it is necessary to note the central, northern, southern, southeastern regions, as well as the adjacent territories of the Caspian Sea.

Wind farms with several thousand MW can operate in Kazakhstan, due to the energy density of wind farms of 10 MW/km^2. 1820 billion kWh annually, the country's wind potential is estimated at such figures.

Due to the geographical features of Kazakhstan, the potential of the country's renewable energy sources (RES) is huge. Currently, the country's leadership pays great attention to the development of RES projects in the Republic.

On July 4, 2009, the Law of the RK No. 165-IV "On Promoting the use of RES" was adopted.

Confirmation of the potential of renewable energy sources, such as solar energy, wind and water in the alternative RK energy sector is the approved program in August 2014 aimed at industrial development of the RK for 2015-2019.

The Government of the RK has established the Department of Renewable Energy (a structural unit of the Ministry of Energy). In turn, the Department has developed a number of regulatory legal acts aimed at completing the tasks set in the field of renewable energy as soon as possible.

A forecast map was also developed up to 2030 with the planned capacity for each renewable energy facility. It is planned to rise the quantity of RES to 32 facilities with a total capacity of 2.4 GW by 2030.

The development of wind energy in Kazakhstan is an important factor in the country's strategy for the transition to sustainable development and diversification of the energy balance. The introduction of wind farms will not only help reduce dependence on fossil fuels and improve the environmental situation by reducing greenhouse gas emissions, but also bring socio-economic benefits by creating new jobs and stimulating economic growth.

However, the development of wind energy faces a number of technical, financial and logistical challenges and requires overcoming resistance to change from traditional society and energy. The successful development of the wind energy sector requires the coordination of efforts by the State, the private sector and the international community.

Thanks to the support of the state and private individuals, wind energy is developing in the form of initiatives and the prospects are promising. Our country has every chance to take a leading position in the alternative energy sector, thereby guaranteeing an independent energy future for its people.

First of all, the payback of their investments plays an important role for the development of wind energy for investors as in competing in the energy market.

Also, for the development of wind energy, the role of the state plays an important role in the form of the creation and implementation of special incentive programs aimed at both production and proper consumption of generated energy from wind farms.

One of the essential factors, for the development of wind energy, first of all, the determining factor is the WPP location, in this regard, Kazakhstan is a rich territory that is favorable for the generation and collection of wind energy. The country's territory is located in the leeward zone of the northern hemisphere, where strong winds from the South-west and North-east directions are observed. However, in existing electricity market conditions, the resources of

the wind power industry in Kazakhstan have not been practically mastered.

The first and most important fundamental problem is the direct dependence of the power of most modern wind turbines on wind speed. There is a dependence in the form that if the actual wind speed is 2 times less than the speed shown in the installation passport, then the output power will be 8 times less, if 3 times less, then the power in this case will be 27 times less.

Based on this, it is necessary to develop and research wind power plants operating at low wind speeds, starting from 3 m/s. One of the wind turbines operating at low wind speeds of 3 m/s is Magnus WPP.

Due to the combined use of two power elements, in the form of a rotating cylinder and a fixed blade, an increase in lifting force is observed, which in turn increases the output power of the installation at the outlet.

1 METHOD OF MATHEMATICAL MODELING OF WIND POWER PLANTS

1.1 Equations describing gas dynamics

Gas dynamics is a branch of hydroaeromechanics that explores the movement of minor moveable media (gas, liquid and solids - under the rapid action of very high pressure) with the expectation of their compressivity. In a broad spectrum, gas dynamics includes acoustics, kinetic meteorology, electrical and magnetic dynamics, dynamics of inert gases, plasmodynamics [1-4]. The theory of inertial gases and plasmas uses statistical descriptions of the behavior of particles that make up the environment. In individual tasks, motion is studied in a continuous model together, using the average values of mass, momentum and energy of a small volume.

Many areas of existing technology are the theoretical basis of gas dynamics. Solving problems of gas dynamics are the basis for the development and creation of such objects as: flying such as airplanes and missiles, as well as their components and elements, artillery shells in wells and their orbits in the atmosphere; energy, including when calculating turbines and compressors; gorenje processes and explosive waves, description of collisions. In turn, the need for technologies contributes to the rapid growth of gas dynamics and the expansion of the problems studied in them. Gas dynamics has a significant impact on the development of many areas of mathematics - the theory of continuous solutions of differential equations.

Under the condition that the temperature and pressure of the gas change with the exclusion of thermal effects from the external environment, while the speed is low, kinetic energy is consumed to compress the working air [3,4]. In the case when a high velocity is observed, the kinetic energy exceeds it. Even the slightest changes in speed entail significant variations in temperature ranges, as well as pressure and density.

Therefore, gas dynamics examines gas flows that occur at high pressure and temperature differences, as well as at high speeds. The connection of gas dynamics with thermodynamics is also due to the need to take into account compression, that is, the change in the state of the gas during movement [3-5].

When solving many problems related to gas dynamics, the air environment moves. If we consider these problems from a theoretical point of view, air in many cases can be considered an ideal gas with constant heat transfer. In some cases, when the pressure is high and the temperature is low, intermolecular interactions will be a difference between air and ideal gases; in cases where the pressure is low and the temperature is high, the difference arises due to ionization and dissociation. For air of normal density, dissociation up to temperatures of ~ 2000 K and ionization up to 10000 K are insignificant. When the temperature is above 500 K, but less than the temperature, in the case when the dissociation process begins, air is considered a gas with ideal thermal stability, since by stimulating the freedom of molecular vibrations, the heat capacity of the air increases [5-7].

The theoretical study of the problems of aerodynamics is difficult, because the nature of the description of differential equations is nonlinear, due to the existing complexity of aerodynamic features. The distribution of a gas perturbation with a finite speed is one of the main parameters of the gas flow. Some faintly visible gas streams can travel at the speed of light (Fig. 1.1).

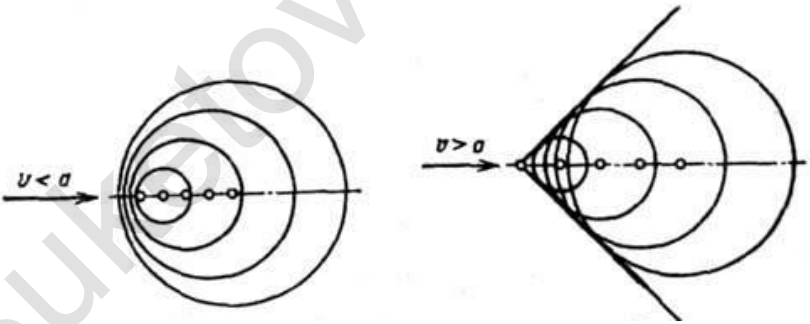

a) *b)*

Fig.1.1. Low perturbations distribution of:
a)- in subsonic stream, *b)*- in supersonic stream

The solution equation systems of the Navier-Stokes, which includes four independent equations (1.1-1.8), requires the problem

of gas dynamics [2-6]:

1. The equation of succession (conservation of mass)

$$\frac{\partial p}{\partial t}\nabla \bullet (\rho \overset{\text{r}}{V}) = 0\,, \qquad (1.1)$$

2. Equation of the number of motion (conservation of momentum)

$$\frac{\partial(\rho \overset{\text{r}}{V})}{\partial t} + \nabla \bullet (\rho \overset{\text{r}}{V} \otimes \overset{\text{r}}{V}) = -\nabla p + \nabla \bullet \tau + \overset{\text{r}}{S}_M\,, \qquad (1.2)$$

where τ - the stress tensor, written as:

$$\tau = \mu\left[\nabla \overset{\text{r}}{V} + (\nabla \overset{\text{r}}{V})^T - \frac{2}{3}\delta \nabla \bullet \overset{\text{r}}{V}\right], \qquad (1.3)$$

where δ - Kronecker's delta function

$$\delta = \begin{bmatrix} 1 & 0 & 0 \\ 0 & 1 & 0 \\ 0 & 0 & 1 \end{bmatrix}. \qquad (1.4)$$

3. The equation of energy (conservation of energy)

$$\begin{aligned} &\frac{\partial(p h_{tot})}{\partial t} - \frac{\partial p}{\partial t} + \nabla \bullet (\overset{\text{r}}{V} h_{tot}) \\ &= \nabla \bullet (\lambda \nabla T) + \nabla \bullet (\overset{\text{r}}{V} \bullet \tau) + \overset{\text{r}}{V} \bullet \overset{\text{r}}{S}_M + S_E \end{aligned}\,, \qquad (1.5)$$

where

$$h_{tot} = h_{stat} + \frac{\overset{\text{r}}{V}^2}{2}\,, \qquad (1.6)$$

$$h_{stat} = h_{stat}(T, p)\,. \qquad (1.7)$$

4. Equation of state

$$\rho = \rho(T, p) \qquad (1.8)$$

The following designations are used to record ratios 1.1-1.8: p - pressure; ρ - density; V - speed; T - temperature; t - time; h_{tot} - total enthalpy; h_{stat} - static enthalpy; $\vec{S}_M$ -the pulse source term; S_E - an energy source member; μ - dynamic viscosity coefficient; λ - thermal conductivity coefficient; ∇ - operator of Hamilton (nabla); $\vec{V}$ - denotes a vector quantity.

The above systems of equations are used to theoretically describe the behavior of liquids, gases and flows.

However, in practice, it becomes need to describe the equations of the perturbation model in order to solve the aerodynamic problem in full.

From the conclusion concluded in the study of systems of equations 1.1-1.8, the conclusion arises that all the main variables obey the general conservation law [4, 8].

Below is the form of writing the differential equation, in the case of the designation of the variable:

$$\frac{\partial}{\partial t}(\rho\phi) + \nabla(\rho\vec{V}\phi) = \nabla(\Gamma\nabla\phi) + S \qquad (1.9)$$

where Γ - diffusion coefficient; S - source member.

The general differential equation consists of four elements: non-constant, convective, diffusive and initial. Various variables, in the form of a component of velocity, temperature, etc., are denoted by a dependent variable ϕ. Nevertheless, for each variable, the original expression S and the diffusion coefficient Γ must have an appropriate value.

During the analysis of the above equations and their systems, it can be argued that they contain equations of both the first and second order. Another distinctive feature is the dependence of the nonlinear nature of the equation conditions on variables [4-6].

Every year, thanks to the development of science, simpler

systems of equations are being developed.

Table 1.1 shows the classification of currents existing in hydrodynamics.

In Table 1.1. the flows are divided according to density and viscosity. As can be seen from the table, inviscid flows, in the case when the viscosity coefficient is 0, are associated with flows whose velocity is lower than the speed of sound, i.e. M = 1.In the case when there is a large difference in temperature in the flow, i.e. when the compressible one must take into account all the equations ($M>0.1$).

Depending on the viscosity coefficient, there are three types of flow. When compressed streams are considered, depending on the number $M<1$ or $M>1$, they must be divided into layers [7-9].

Table 1.1

Current classification

Viscosity	Density	
	Incompressible ($\rho = \text{const}$)	Compressible ($\rho \neq \text{const}$)
Inviscid currents ($\mu = 0$)	Potential currents ($\mathbf{rot}\vec{V}=0$)	Gas dynamics ($\lambda = 0$)
Flow in boundary layers (viscosity is significant near the surface)	Laminar flows (very small numbers *Re*) Turbulent flows (large numbers *Re*)	Heat transfer is essential
Breakaway currents (viscosity is essential everywhere)	Laminar flows (small numbers *Re*) Turbulent flows (very large numbers *Re*)	Heat transfer is essential

A direct consequence of the inability to accurately solve the system of Navier-Stokes equations is an attempt to find a tool for finding an approximate solution to problems of gas dynamics, even in the most general formulation.

1.2 Basic methods for solving equations of gas dynamics

Creating a numerical solution for some equations for which it is not possible to find an exact solution is the only option for solving them. The block diagram of the numerical solution is shown below in Figure 1.2.

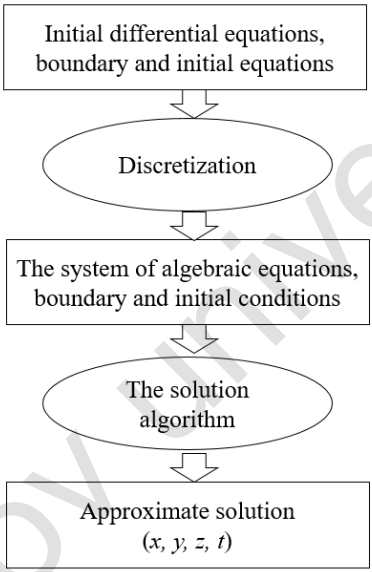

Fig.1.2. The process of constructing a numerical solution

The first step in creating a numerical solution is discretization. Which uses discrete initial equations describing a continuous process, as well as initial and boundary conditions to convert them into discrete equations.

Using conversion methods, it is possible to convert them into a system of algebraic equations or a system.

When choosing a differentiation method, it is necessary to pay attention to such factors as whether time-dependent derivatives or space-dependent derivatives are taken into account [8-10].

In solving practical problems, the differentiated method is

mainly used [7]. For discrete spatial derivatives [5, 7, 11, 12], methods of both finite differentials, elements and volumes are used.

Based on the differentiation method, in the equations, the values of the desired variable are combined with a set of points of neighboring nodes [4, 7].

The control volume method (CVM) is very simple to understand and allows for physical interpretation [5, 6, 7, 11, 12, 13]. The estimated area is divided in such a way that some sections do not intersect the controlled areas. Differential equations are integrated into each controlled volume. For integration, the built-in controller uses Shape functions that describe the change of each variable of interest between the separation points. As a result, discrete analog differential equations consist of values at many different points. The control volume control center has been adopted as a computing node in CVM [4, 5, 7, 11, 12, 13,14].

The resulting discrete analog describes the law of conservation of a finite control volume, since the differential equation denotes the law of conservation of an infinite control volume [4].

To obtain the mathematical formula CVM, it is necessary to apply the basic differential relations (1.10) - (1.18). The continuous equation, the degree of motion and the total differential (1.19), written as coordinates, take the following form [10-13]:

$$\frac{\partial \rho}{\partial t} + \frac{\partial}{\partial x_i}(\rho V_i) = 0 \ , \qquad (1.10)$$

$$\frac{\partial}{\partial t}(\rho V_j) + \frac{\partial}{\partial x_i}(\rho V_i V_j) = -\frac{\partial P}{\partial x_j}\left[\mu\left(\frac{\partial V_j}{\partial x_i} + \frac{\partial V_i}{\partial x_j}\right)\right], \qquad (1.11)$$

$$\frac{\partial}{\partial t}(\rho\phi) + \frac{\partial}{\partial x_i}(\rho V_i \phi) = \frac{\partial}{\partial x_i}\left[\Gamma\left(\frac{\partial \phi}{\partial x_i}\right)\right] + S \qquad (1.12)$$

Then, according to the above equations, each expression (1.10) - (1.12) should be included in the control volume. At the same time, using the Ostrogradsky-Gauss theorem, it is convenient to transform

some volume integrals into surfaces. The corresponding derivatives can be removed from the sign of the integrals in the absence of deformation during the control time (the calculation grid does not change with time):

$$\frac{d}{dt}\int_{\Omega}\rho d\Omega+\int_{S}\rho V_i dn_i=0\,, \qquad (1.13)$$

$$\frac{d}{dt}\int_{\Omega}\rho V_j d\Omega+\int_{S}\rho V_i V_j dn_i= \\ -\int_{S}P dn_i+\int_{S}\mu(\frac{\partial V_j}{\partial x_i}+\frac{\partial V_i}{\partial x_j})dn_i+\int_{\Omega}S_{Vj}d\Omega \qquad (1.14)$$

$$\frac{d}{dt}\int_{\Omega}\rho\phi d\Omega+\int_{S}\rho V_i\phi dn_i=\int_{s}\Gamma(\frac{\partial\phi}{\partial x_i})dn_i+\int_{\Omega}S d\Omega \qquad (1.15)$$

where Ω is the control volume; S - a control surface that limits the control volume; dn_i - the differential of the Cartesian component of the vector of the external normal to the surface.

In integral proportions, volumetric integral determine the numerical level of volume variables.

Then the exact integral equations (1.13) — (1.15) must be transformed into a discrete form, which uses a number of different sampling schemes. Thus, CVM is reduced to an integral form before discrete fundamental differential equations. Using approximations of variables, the volume components are transformed into separate cell segments (Figure 1.3), and then integrated into each volume segment, forming a control volume together. The components of the surface (flow) are first calculated for integer points located in the center of the surface segment into which the control volume is inserted, and then the total change is calculated by integrating the obtained lines along each side [7].

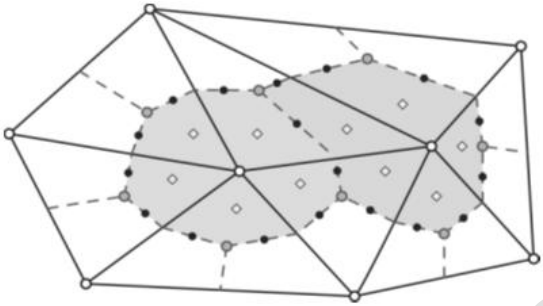

Fig.1.3. Creation of a control volume on the basis of a gridded model

Integral relations's discrete forms can be obtained (Euler approximation scheme using a first-order postdifferentiation):

$$\Omega(\frac{\rho-\rho^0}{\Delta t})+\sum_{ip}(\rho V_i \Delta n_i)_{ip}=0, \qquad (1.16)$$

$$\Omega(\frac{\rho V_j-\rho^0 V_j^i}{\Delta t})+\sum_{ip} m_{ip}(V_j)_{ip}= \sum_{ip}(P\Delta n_j)_{ip}+\sum_{ip}(\mu(\frac{\partial V_j}{\partial x_i}+\frac{\partial V_i}{\partial x_j})\Delta n_i)+\bar{S}_{Vj}\Omega, \qquad (1.17)$$

$$\Omega(\frac{p\phi-\rho^0\phi^0}{\Delta t})+\sum_{ip} m_{ip}\phi_{ip}=\sum_{ip}(\Gamma(\frac{\partial \phi}{\partial x_i})\Delta n_i)+\bar{S}\Omega. \qquad (1.18)$$

where Δt is the time step; Δn_i - increment of the Cartesian component of the vector of the external normal to the surface; index "$_{ip}$" means calculation for the integration point and summation over all integration points of this control volume; index "^{0}" indicates that the value corresponds to the previous time value.

The mass change m_{ip} (mass flow rate) through the surface of the bulk element is obtained as follows

$$m_{ip} = (\rho V_i \Delta n_i)_{ip}, \qquad (1.19)$$

The values received in the solving can lead to the centers of the control volume However, some expressions of the equation require solutions for integer points. Approximate functions (Shape functions) of finite elements are used to find values inside a network element.

The changes for each variable in the range can be written as

$$\phi = \sum_{i=1}^{n} N_i \phi_i, \qquad (1.20)$$

where N_i is the approximating function for the i th node; ϕ_i - the value of the variable in the i st node; n - the number of nodes of the element.

Summarizing is performed on all nodes of the element. In this situation, the approximated has the followings properties:

$$\sum_{i=1}^{n} N_i = 1, \qquad (1.21)$$

for the j st node $N_i = \begin{cases} 1, & i = j; \\ 0, & i \neq j. \end{cases}$

The content of precise integral quantities, such as mass, volume of motion and energy, for any control group of volumes and, therefore, for the entire computational domain is an important feature of CVM. This property manifests itself for any number of nodes, not just for a very large number of constraints. Therefore, even the solution on the initial lattice corresponds to the correct integral balances [4, 5, 7].

There are two basic kinds of CVM, which are characterized by the position of the volume relative to the initial grid elements (geometry) (Fig. 1.4) in the middle of the node and in the middle of the cell [4, 11, 12, 13].

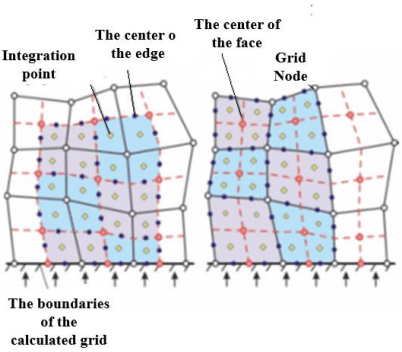

Fig.1.4. A control volume diagram centered at a node (left) and centered in a cell (right)

Computational algorithms can also use so-called spatial (chess) or combined networks. This is due to the different ways in which the pressure field is calculated.

1.3 Solving problems of gas dynamics using computer programs

To implement a mathematical model - the Navier-Stokes system, including for solving problems of gas dynamics, such tools as numerical methods. The development and creation of various numerical methods has facilitated the work of hydrogasdynamics researchers, thanks to the possibility of modeling and reproducing the behavior of liquids or gases under various conditions. For this purpose, special software algorithms for numerical calculation have been developed, but their use is limited by the specification of researchers and engineers whose field of activity is computational fluid dynamics [13-15].

Based on this, for the development of hydrogas dynamics, it is necessary to create computer packages and programs designed for a wide audience, which will be interesting both for students and for more wholesale users. Due to global digitalization, the use of numerical methods for solving problems of hydrogas dynamics is becoming popular. Also, the use of computer packages to solve problems eliminates the use of time-consuming methods.

When calculating the problems of hydrogas dynamics, it is necessary to take into account such factors as the type and number of models of behavior of liquids and gases, as well as the level of complexity of the problem itself. Based on this, existing computer programs for numerical modeling should be divided according to the level of tasks to be solved[15]:

1.The so-called "heavy" packages are high-end packages designed for both scientific and technical tasks, using various mathematical methods capable of solving the most complex problems. Such well-known commercial packages as CFD-ANSYS CFX (ANSYS, Inc.), Star-CD (CD-adapco), fluent (together with ANSYS, Inc. Fluent, Inc.) can be attributed to the "heavy" class. Such complex tasks, taking into account Gorenje, chemical reactions, multiphase flow, support of various types of grids, etc., can be solved by all these packages, using various turbulent models.

2. A middle class designed for engineering calculations. However, the models offered in this class are significantly expensive. These include software packages such as ANSYS FLOTRAN (ANSYS, Inc.),STAR-CCM+ (CD-adapco), Cosmosfloworks (SolidWorks Co.).

3. The so-called "light" computer packages, which differ from the other two classes in their low accuracy, can therefore be used for educational and methodological purposes, or for a narrow task.

The basis for solving problems in all types of computer packages is CVM.

The process of solving problems embedded in the database of computer packages consists of the following stages:

1. The first stage is a preparatory one for the calculation model, consisting of:

a) Development of a computational model of the problem under study with specified boundary conditions.

b) Splitting the computational model into grids to obtain an accurate result.

c) Setting the input, output and boundary conditions as well as the calculation model.

2. Choosing the solver to perform the calculation.

3. Getting the calculation results and discussing them.

4. If we are satisfied with the results obtained, then we can change the number of grids and cells of the calculation model, set the parameters as well as the calculation model.

Also, the study of the influence of the number of grids and cells on the quality of calculations, operating costs and convergence of grids can serve as a prerequisite for correcting the results obtained [13-15].

1.4 Analysis and review of existing approaches, methods of numerical simulation of wind power plants

Researchers from all over the world continue to develop and optimize wind power plants in order to eliminate the disadvantages associated with low operating efficiency under various climatic conditions, and to effectively use numerical research methods for this purpose by creating mathematical models of installations.

By the present time, all wind power plants used in practice are divided into horizontal and vertical axes of rotation. Figure 1.5 below shows comparative power output data depending on the linear dimensions of installations with a horizontal axis of rotation [16].

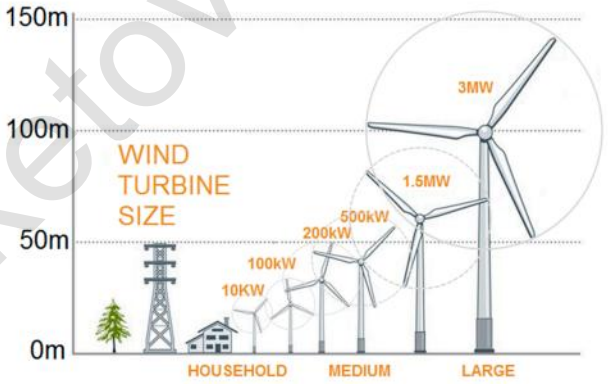

Fig.1.5. Comparative power output data depending on the linear dimensions of installations with a horizontal axis of rotation [16]

There are a number of scientific papers aimed at studying the power elements of wind turbines of various capacities using CFD and programs for designing and calculating blades based on a traditional pulse element, to eliminate problems such as high turbulence, low speed and a change in wind direction that directly affect the performance of installations [16].

One of the most effective installations designed for densely populated cities, or for areas with low winds, are low-power multi-purpose wind turbines (Figure 1.6) [17]. The advantages of such installations are the generation of energy without losses for the transmission of electricity.

Fig.1.6. Variants of low-power wind turbines: (a) Darrieus wind turbine; (b) A three-bladed propeller with a horizontal axis of rotation; (c) A Savonius rotor with a vertical axis of rotation [17]

The paper simulates a 3.7 kW wind turbine with a vertical axis of rotation based on the CFD method (Figure 1.7).

Studies of the power efficiency of the installation at low wind speeds have been carried out. Using CFD analysis, an rise in the power efficiency of the installation is shown from the addition of a convergent duct to a Darrieus VAWT. It is shown that the power factor increases by almost 125%, with an average wind speed of 8 m/s.

In [19], numerical results of an investigation based on the k-ε turbulence model of a low-power wind turbine operating flanged diffuser to increase electricity generation are presented. Numerical

results showed the formation of vortices on the on the windward side of the flange, thereby reducing the pressure values. It is indicated that the right flange with an angle of 15° it is the most efficient in terms of accelerating the flow at the entrance to the diffuser.

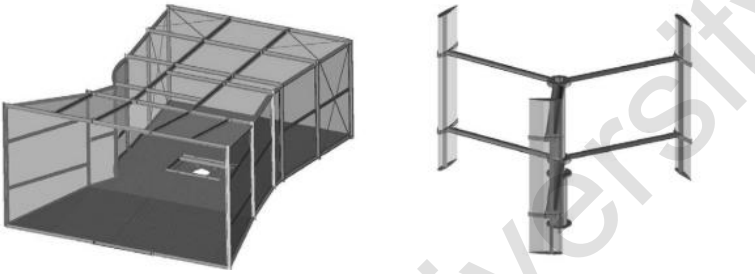

Fig.1.7. A wind turbine with a low-power vertical axis of rotation with a convergent channel [18]

One of the problems that worsen the aerodynamic performance of wind turbines operating in cold, humid conditions is the icing of the blades, as a result of which ice with a thickness of 30 cm can accumulate at the ends of their blades. The study [20] presents a new approach to predicting the build-up of ice, as well as its shape on a VAWT. Using the FENSAP-ICE modeling tool (Figure 1.8), the results of the shape of the ice accretion in the range of angles of attack from -25° to 25° were obtained. It is indicated that the installation loses up to 60% of its power to the process of frost formation.

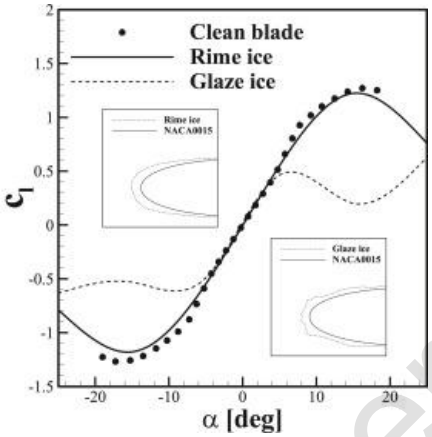

Fig.1.8. Dependence of the lift coefficient on the attack angle for blades under various conditions [20]

One of the problems with the operation of wind power plants of various configurations is the noise generated by turbines. The work' authors [21] calculated the aerodynamic noise from the operation of a double blade with a power of 3.0 MW using the acoustic model FW-H, based on a computational fluid dynamics program, and a turbulence model with simulation of large vortices. In accordance with the distribution of the static pressure field (Figure 1.9) and the flow vectors, the discrete characteristics of the tip noise spectrum are separated.

The number of blades in wind power plants plays a huge role in the output energy performance. The study [22] shows the results of experimental and computational investigations of number's effect of blades on the power and thrust coefficients of a wind turbine with a low-power horizontal axis of rotation. CFD modeling was performed using the SST k-ώ turbulence model, which was compared with experimental data. It is determined that a 3-blade wind turbine has a maximum power factor compared to installations with 5 and 6 blades (Figure 1.10).

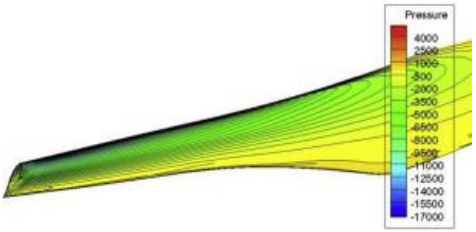

Fig.1.9. Distribution of the static pressure field around the blade [21]

For densely populated cities and areas with small wind corridors, there is a problem in developing suitable wind power plants operating in low winds. For this purpose, numerical and experimental studies have been conducted in the last decade to develop Magnus wind turbines, which have rotating cylinders instead of traditional blades.

The authors conducted an aerodynamic analysis to estimate the power of a wind turbine with a horizontal axis of rotation (Figure 1.11), the blades of which are ribbed with a spiral [23]. The calculated power factor reflects the ideal aerodynamic behavior, and is It is used for analyzing data on characteristics of the installation. Studies have also been conducted on the effect of various blade shapes (without an edge, with a straight edge and with a spiral edge) on the lift coefficient. Figure 1.12 shows that the shape of the blades with ribs is more efficient than without ribs.

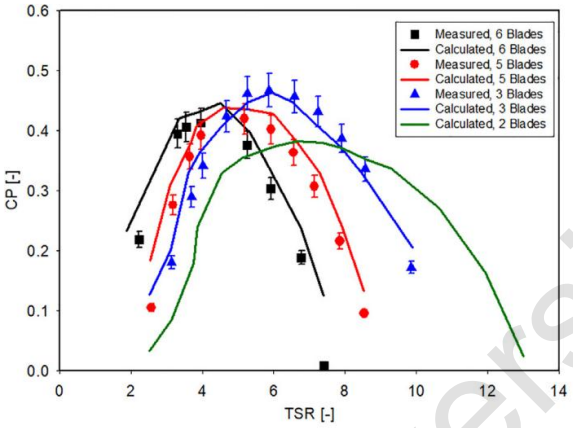

Fig.1.10. Power curves of numerical and experimental studies for 2, 3, 5, 6-blade wind turbines at a wind speed of 8 m/s [22]

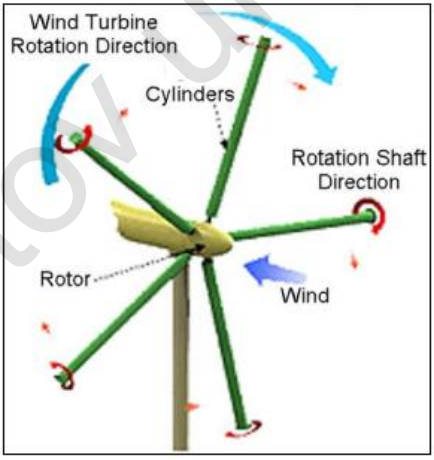

Fig.1.11. Magnus wind turbine with a horizontal axis of rotation, the blades of which are finned with a spiral [23]

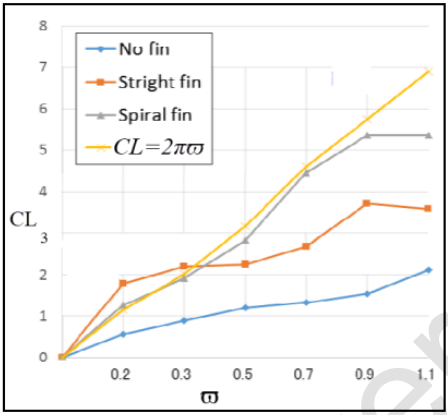

Fig.1.12.Dependence of the lift coefficient for three blade variants [23]

As follows from the above data, the streamlined state the blade itself, i.e. the cylinder, plays a huge role in the entire performance of a wind turbine. The authors of [24] performed direct numerical simulation (DNS) of the turbulent flow around the Flettner rotor (Figure 1.13), that is, an electrically driven rotating cylinder in the boundary layer of the atmosphere. The Reynolds number and various aerodynamic coefficients have been studied, which give a complete aerodynamic picture of the stream around the Flettner rotor.

As follows from Figure 1.13 on condition cylinder begins to rotate, a vortex motion occurs around the bases of the cylinder.

In [25], the authors investigated the effect of various surfaces with roughness created by sandpaper on the output torque of a Magnus wind turbine. It is established that the use of P40 sandpaper to create a rough surface increases the output torque coefficient by almost five times.

Numerical studies of CFD aerodynamics around a Darrius VAWT with cylindrical blades are presented in [26]. The aerodynamic flow was studied for several values of the tip gear ratio (TSR), i.e. δ = wC/wT. The direction of the lift coefficient and drag force are shown in Figure 1.14.

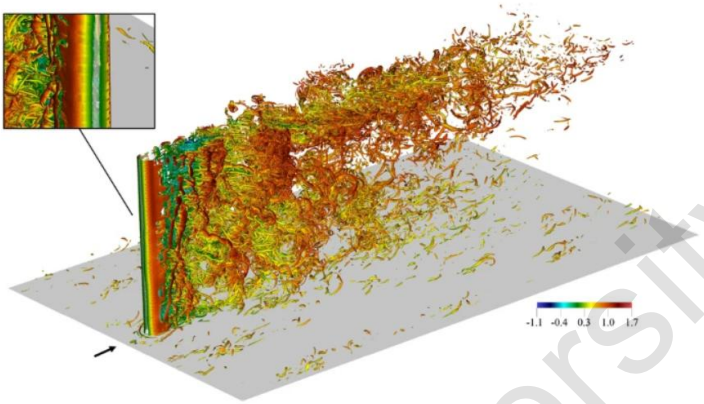

Fig.1.13. Three-dimensional visualization of flow velocity vectors around the cylinder

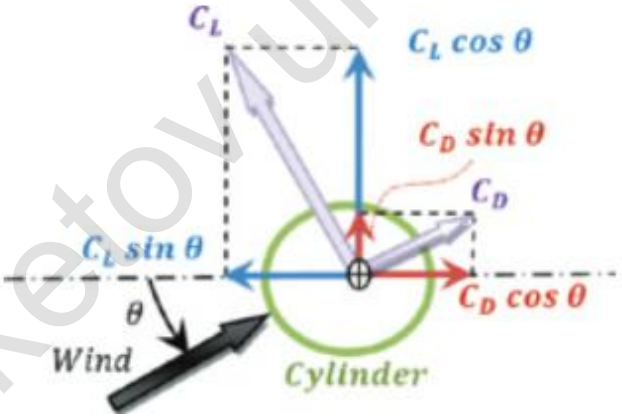

Fig.1.14. The direction of the aerodynamic force coefficients

Using rotating cylinders in Magnus-type wind turbines, it is possible to achieve an increase in lift 10 times higher than the aerodynamic profile. But nevertheless, in parallel with this, the aerodynamic drag is also growing. Recent studies [27] have improved aerodynamic performance by changing and modifying

power elements by changing surfaces, adding dimples and protrusions, as well as changing the shape of round cylinders into a truncated cone.

1.5 The current state of the problem

Currently, the problem of energy saving occupies a leading position worldwide, since industry and technology are constantly developing, and this leads to a significant increase in energy costs, an increase in corporate costs and an increase in the cost of products produced by enterprises. In the face of increasing competition, enterprises are forced to strive to reduce electricity consumption and improve the energy efficiency of certain industries.

The importance of energy saving issues in the state is to a certain extent confirmed by the base of laws. Kazakhstan 2050 promotion strategy our country considers it necessary to move to a "green economy" and a new industrial revolution.

Most energy consumers require a small amount of energy (from a few hundred watts to ten kilowatts), the most important indicators of which are reliability, long-term resources and low operating costs. Automatic installations powered by renewable energy sources, such as wind turbines powered by the Magnus effect, meet these requirements.

There are known works where an increase in lift and an improvement in aerodynamic quality have been proven by optimizing the shape and surface of the cylindrical blades of Magnus wind turbines. Based on this, it is necessary to create new methods and methods for optimizing HAWT and VAWT for low wind speeds zones.

2 NUMERICAL STUDY OF THE DESIGN OF COMBINED BLADES OF WIND POWER PLANTS

2.1 The optimal choice of the blade shape of a wind power plant based on the design method

The main goal that arises during the design and development of WPP is to achieve maximum output power under specified atmospheric weather conditions. From a physical point of view, this is achieved by creating blades with optimal parameters and shapes. Changing the shape and linear dimensions of the blades affects the aerodynamic coefficients of the WPP's blade. When making a blade, about 15-20% of the total cost of production of a wind power plant is spent. Nevertheless, the profit gained from improving the structural model of the blade is tangible [28].

The problem of determining the optimal shape of the blade and determining the optimal composite material is difficult, since the mathematical formulation of the aerodynamic load is complex and it is necessary to fulfill a number of limitations and tasks.

Currently, there are 3 types of wind turbine design (Figure 2.1).

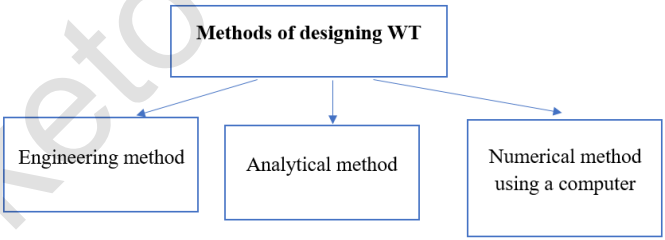

Fig.2.1. Wind turbine design methods

As shown in the Figure 2.1, the first and third methods are often used in engineering practice in creating elements and wind turbines themselves.

One of the most popular WT in the world are winged vane wind turbines. However, in addition to the indisputable advantages, such wind turbines have one, but very significant drawback – orientation to the wind. Developers and manufacturing companies deliberately conceal this fact from the consumer, informing him only about the advantages of the installation. In fact, it turns out the following. The wind generator power is estimated on the basis that the wind orientation always corresponds to the rotation axis of the wind generator, i.e. the breeze blows straight onto the calculated surface of the blades. The resulting design power of the WPP is produced. but it is known from life that the wind direction is not a fixed value [28-30].

Other representative of Magnus wind turbines are installations with cylindrical blades. Compared with vane wind turbines, these installations have the advantage of generating energy at low wind speeds ranging from 2-3 m/s, and there is no need for wind orientation. Due to the cylindrical blades, the wind potential of the air is captured, both from the windy side and from the windward side, so there is no need to orient in the wind direction [31].

The work's authors [32] carried out a modification of the blade, which is a combination of blades in which the usual circle-shaped model is combined with a concave elliptical model. It was established that the combined blade improves the characteristics of the maximum wind turbine power factor (Cp_{max}) by up to 11%.

Based on this, using design methods, it is possible to create a combined blade containing a cylinder and a traditional fixed blade, thus, two lifting forces, fixed and cylindrical blades, are combined, and the dependence of the cylinder rotation speed on wind speed decreases [33,34].

In our case, a numerical design method using computer programs was used.

There are known data on the effect of the comparative cylinder length on the values of lift and drag. It was found that with the cross cylinder flow, the effect of cylinder elongation on the coefficient of drag and lift is sufficiently exerted [35]. It was determined that with a relative length of L/d = 40, the value of this coefficient differs by 18% from the data for an infinite cylinder [36]. From this, it can be deduced that in order to design the optimal blade sizes, it is

necessary to select, based on previous work, the optimal values of the length and cylinder diameter, and fixed blade angle.

Based on the existing works of well-known authors and engineers, 4 numerical models of blades with different angles of the fixed blade were created using numerical modeling (Figure 2.2). Focusing on the highly effective results of well-known works by such a number of authors as S.I. Isataev, O. Zhangunov, K.Kusainov and N.K.Tanasheva [32-36], an optimal cylindrical blade with a length of 300 mm and a diameter of 50 mm was created. The width of the fixed blade was 33 mm, and the length was 300 mm.

Numerical modeling in to define the optimal angle of inclination of the fixed blade relative to the cylinder it was conducted with the using of the ANSYS WORKBENCH software. Using the three-dimensional modeling system, 4 versions of blades with angles of 0, 30, 45 and 60 degrees were designed. The air flow velocity varied from 3 to 12 m/s.

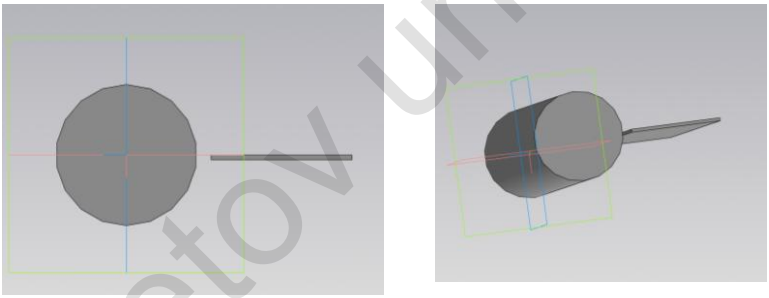

a) at 0 degrees

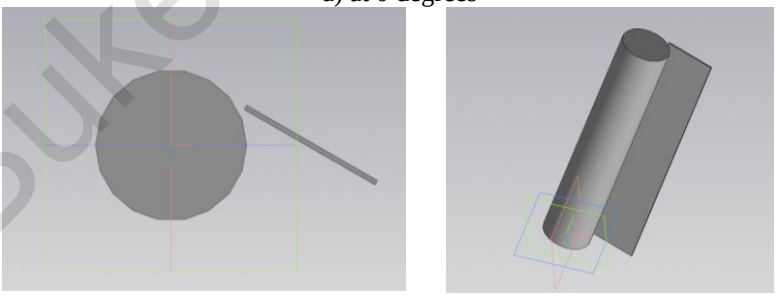

b) at 30 degrees

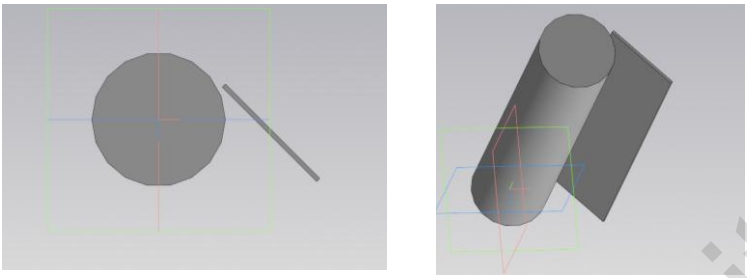

c) at 45 degrees

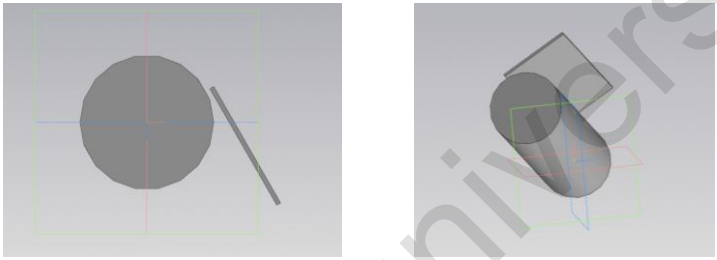

d) at 60 degrees

Fig.2.2. Options for the location of the fixed blade relative to the cylinder

Computing area

Using the Enclosure program [37-40], a cylindrical computational subdomain was created around the combined blade, with a radius of 0.05 m to set rotation conditions around the y axis. To set the boundary conditions around the swept space, a subdomain was created that simulates a wind tunnel in the form of a parallelepiped with dimensions of 1m; 1m; 1.5 m; 1;1;2m minus the cylindrical subdomain (Figure 2.3).

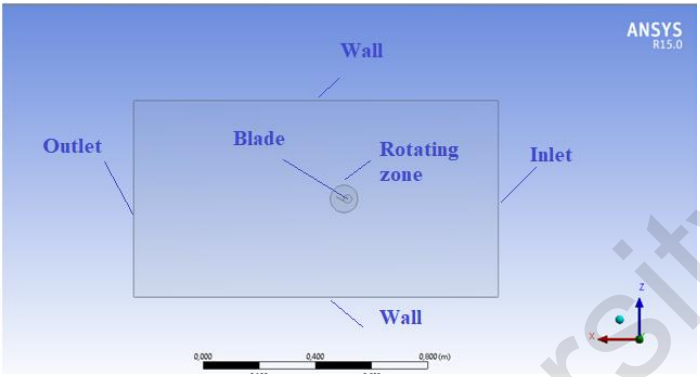

Fig.2.3. A blade model with a calculated area

Boundary conditions

To perform further calculations, boundary conditions were set:

The wall (no-slip). The boundary conditions of the wall are used to bind the liquid and the solid area. In our case, it will be the blade surface and atmospheric air.

The speed at the entrance. It is used to determine the set air flow velocity, and it will be (3, 5, 7, 10, 15 m/s) together with all the corresponding scalar properties of the flow, as a turbulent model at the flow entrance. The total pressure is not fixed, but will rise to any value necessary to ensure the necessary velocity distribution.

Rotation of the blade. It is a periodic boundary condition, and is equal to 300, 500, 700 rpm.

Turbulence model

The problem was solved in a stationary setting.

The process of integrating the system of Navier-Stokes equations into the stage of numerical modeling is performed. The Realizable k-ε model was chosen as the turbulence model, which is suitable for modeling the processes of flow around rotating elements.

Aerodynamic coefficients

An indicator of the efficiency of an aerodynamic element is the aerodynamic coefficients. Using formulas (2.1) and (2.2), the aerodynamic coefficients were calculated numerically [28].

The drag coefficient is calculated in accordance with to the formula (2.1):

$$C_x = \frac{2F_x}{\rho u^2 S} \qquad (2.1)$$

The lift coefficient is calculated using the formula (2.2):

$$C_y = \frac{2F_y}{\rho u^2 S} \qquad (2.2)$$

where F_x is the drag force; F_y - the lifting force; ρ – the density of the air; u - the flow rate; S – the area of the midsection.

The results of the numerical study and their discussion

As a result of numerical modeling, the results of the distribution pattern of velocity vectors around the combined blade at V=7 m/s, n=500 rpm are obtained (Figure 2.4).

In the upper left corner there is a color gradation from blue (minimum) to red (maximum), which is a panel of symbols.

It is determined from the drawings that the angle of inclination of the fixed blade has a great influence on overall picture of the distribution of velocity vectors. As the angle of the fixed blade increases, the turbulence between the cylinder and the blade increases. A so-called enclosed space is created, which, with increasing angle, becomes more enclosed and gives more resistance when flowing around the airflow. It was determined that when the fixed blade is positioned at an angle of 0 degrees to the cylinder, a maximum flow velocity of about 11.71 m/s is observed, which is an assumption about the most effective location of the fixed blade.

Figure 2.5 displays the outcomes of the static pressure distribution field ($p_{st} = p - p_{atm}$) around the combined blade at V=7 m/s, n=500 rpm.

It is determined from the drawings, at an angle of 0 degrees of the fixed blade, the so-called additional repulsion of the entire combined blade occurs due to the formation of high pressure behind the fixed blade. This results in the formation of an additional lifting force of the most stationary blade.

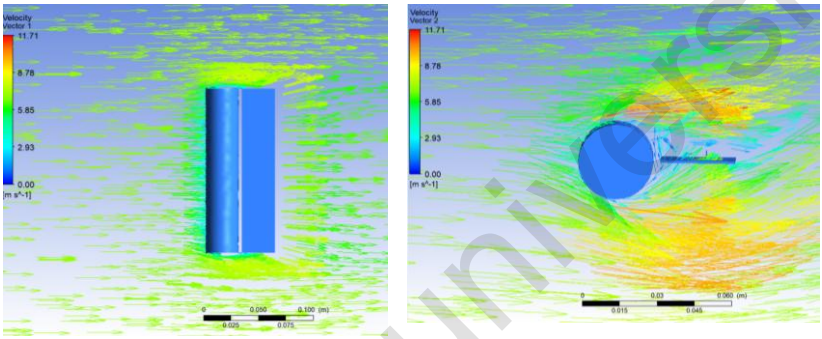

a) 0 degrees

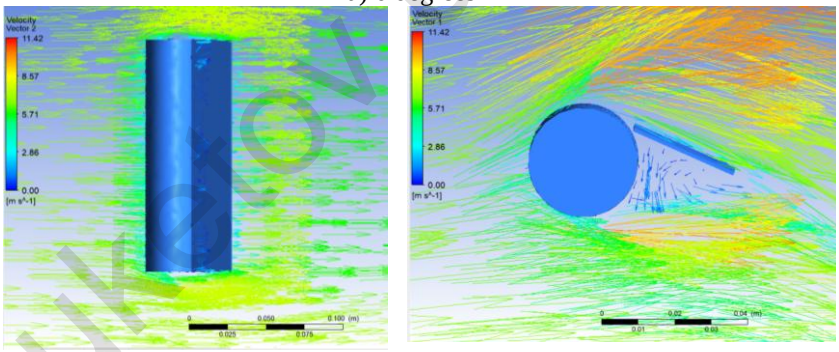

b) 30 degrees

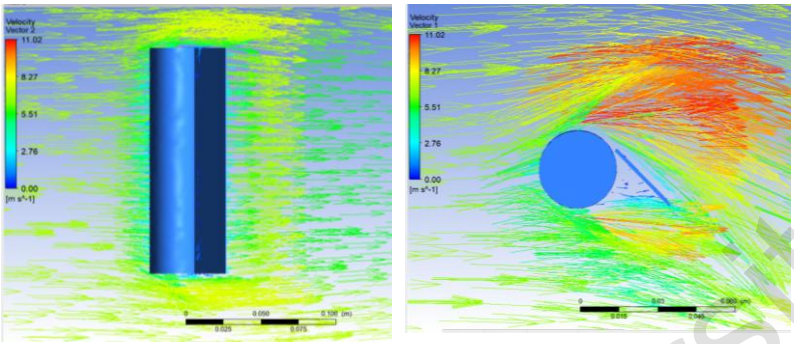

c) 45 degrees

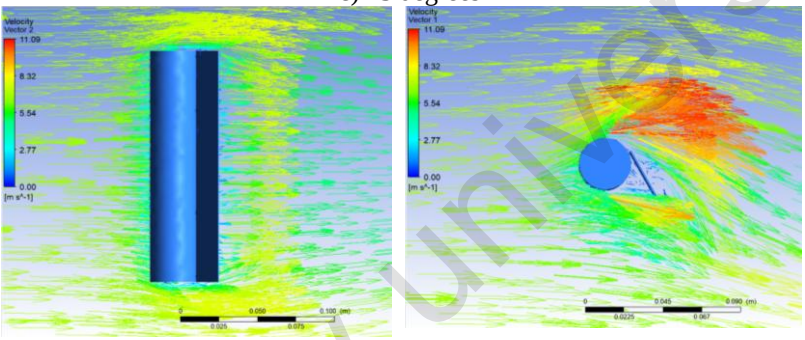

d) 60 degrees

Fig.2.4. Velocity vector distributions around the combined blade at V=7 m/s, n=500 rpm

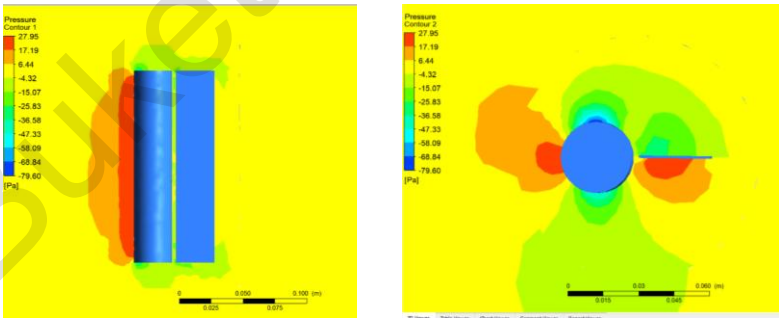

a) 0 degrees

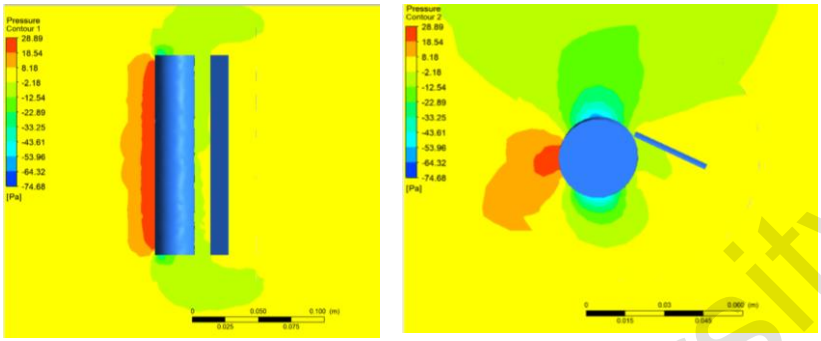

b) 30 degrees

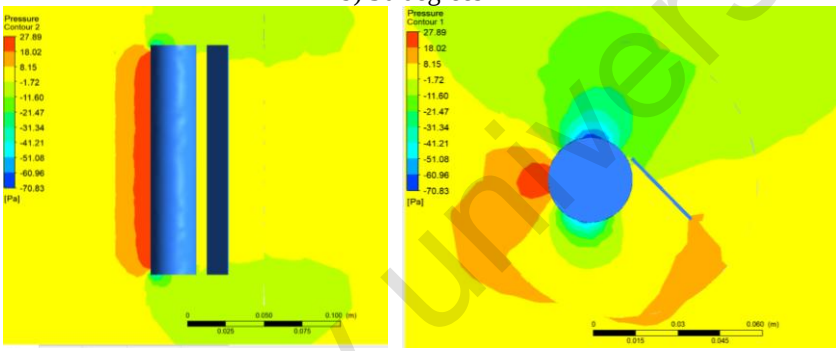

c) 45 degrees

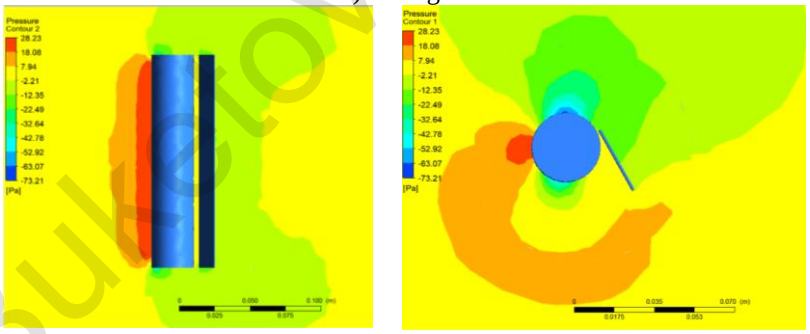

d) 60 degrees

Fig.2.5. Pressure fields around the combined blade at V=7 m/s, n=500 rpm

Figures 2.6 and 2.7 present the results of numerical calculation of the lift coefficient and drag coefficient from the Reynolds number for various variants of the fixed blade relative to the cylinder

.

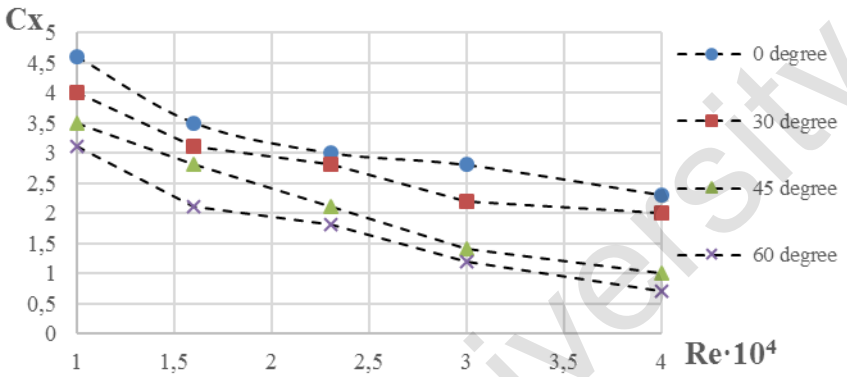

Fig.2.6. Dependence of the drag coefficient on the Reynolds number

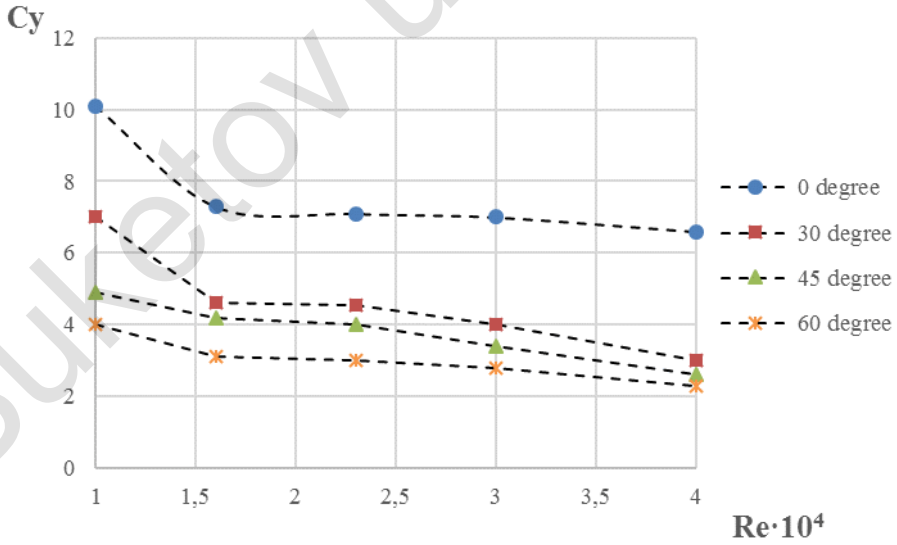

Fig.2.7. Dependence of the lift coefficient on the Reynolds number

It is determined from the Figures 2.6 and 2.7, when the fixed blade is positioned relative to the cylinder at 0 degrees, the optimal values of the lift and drag coefficients are obtained: 0.05 and 0.03 with a Reynolds number of $1 \cdot 10^4$. Compared to the other three samples, at 30°, 45° and 60°, at 0° the combined blade produces maximum lift and minimum drag force. In further numerical calculations, a mathematical model of a combined blade with a fixed blade relative to the cylinder at 0° was used.

2.2 Creation of a 3D model of the blade profile for modeling. Work in Design Modeler

The main goal of the simulation is to study the aerodynamic coefficients of the new design of the combined blade of the wind power blade. The steps of computational simulation are illustrated in Fig. 2.8 [40-45].

The preprocessor of computational simulation consists of the creation of the geometries of the model under study, the separation of the model into finite element grids to improve the quality and speed of the study, and setting input and output boundary conditions. The preprocessor includes such ANSYS Workbench products as the universal CAD editor DesignModeler and the Ansys Meshing grid generator.

The *solver* sets parameters such as: turbulence model (laminar or turbulent), boundary condition parameters (flow velocity, inlet and outlet pressure, rotation speed, etc.), solver methods (SIMPLE, SIMPLEC, PISO, COUPLED), initialization methods (hybrid or standard), number of iterations.

A *postprocessor* is used to verify the results and 3D visualization.

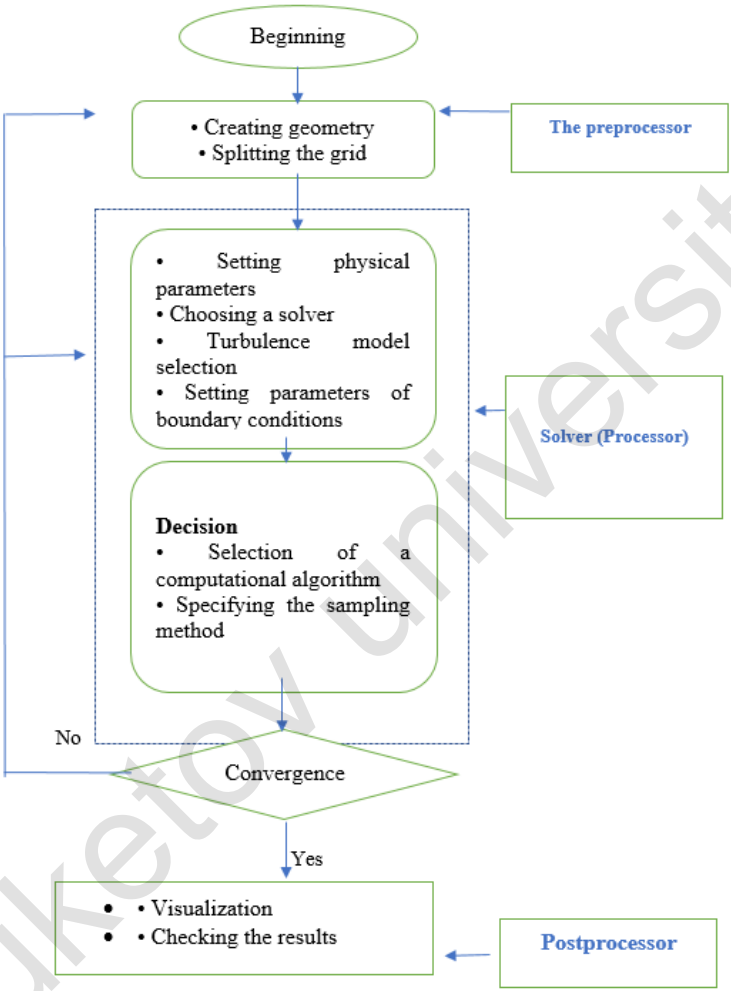

Fig.2.8. Stages of mathematical modeling

First, the blade geometry and calculated fluid areas are modeled in ANSYS DesignModeler to accurately measure the test blade in a simulated wind tunnel.

Using the COMPASS 3D three-dimensional modeling system and Design Modeler, a CAD (Computer-Aided Technologies)

(Fig.2.9) model of the blade in the XYZ three-dimensional plane was created (Fig.2.10). Optimal geometric data of the blade are presented in Table 2.1.

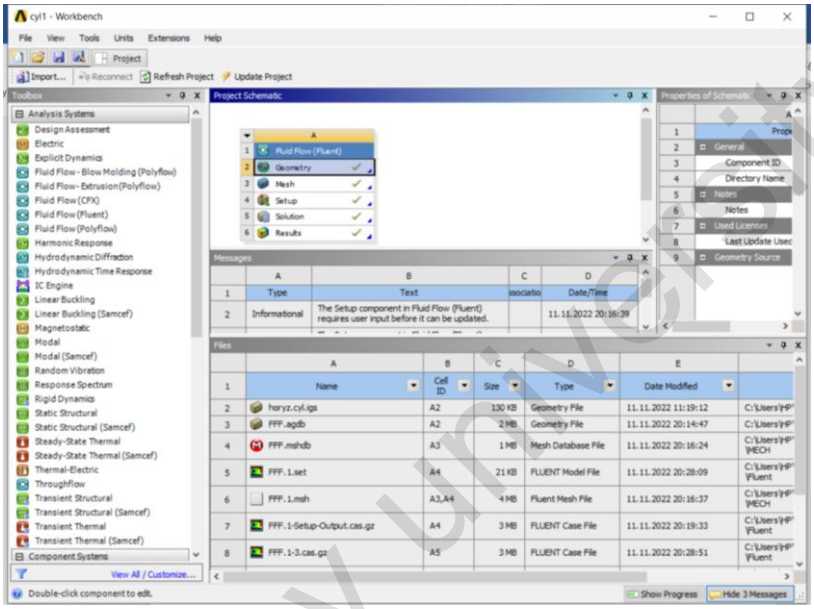

Fig. 2.9. The ANSYS Workbench work window

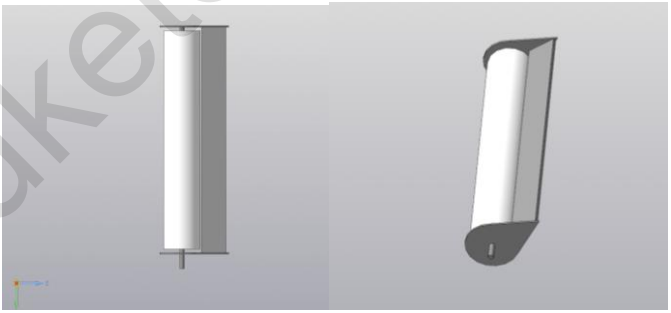

Fig.2.10. A combined blade in a three-dimensional plane

Figure 2.10 shows, that the combined blade consists of a cylinder and a fixed blade mounted on both sides on a base in the form of a teardrop-shaped disk.

Using Enclosure program, a cylindrical design subdomain was created around the combined blade, with a radius of 0.05 m to set rotation conditions around the y axis. To set the boundary conditions around the swept space, a subdomain was created that simulates a wind tunnel in the form of a parallelepiped with dimensions of 1m; 1m; 1.5 m; 1;1;2m minus the cylindrical subdomain (Figure 2.11).

Table 2.1.

Geometric parameters of the blade

Parameters	**Values**
Cylinder length, L	300 mm
Cylinder diameter, d	50 mm
Fixed blade height, a	310 mm
Fixed blade width, b	33 mm
The fixed blade thickness, c	4 mm
The length of the teardrop-shaped base,l	94 mm
The radius of the teardrop-shaped base, R	30 mm

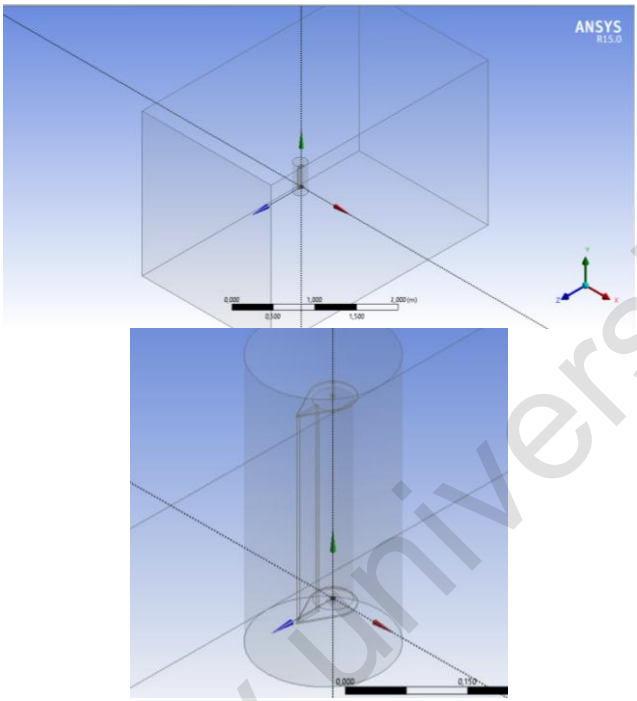

Fig.2.11. The calculated area around the blade

Eventually, after performing Boolean operations in the universal CAD editor, 2 bodies were created- a cylinder minus the blade, as well as a parallelepiped minus the cylinder. Later, the created model is imported into the grid preprocessor.

2.3 Selection of the computational grid of the area for numerical analysis of the flow field. Setting the boundary conditions for the calculated grid

The creation of a computational grid is one of the decisive moments in the modeling process, which affects the accuracy of the results and convergence.

Comparing the predicted values of the aerodynamic coefficient of the three grids (Table 2.2), there is no noticeable difference

between the last two smaller grids, but there is a greater deviation from the first, coarser grid. Considering the computational cost and reasonable accuracy, a grid 3 with a number of cells of 248723 is sufficient.

Table 2.2.

Comparison of the predicted values of the aerodynamic coefficient from three grids

	Grid 1	**Grid 2**	**Grid 3**
Number of cells	187450	248723	478400
Lifting force coefficient	0,031	0,037	0,036
Air flow rate	9 м/с	9 м/с	9 м/с

The ANSYS Meshing grid preprocessor creates high-quality computational grids for almost all physical tasks. Of course, the volumetric grid consists of tetragonal cells. The grid image in the XY plane, the cross section of the area Z=0, is shown in Figure 2.12. Boundary conditions at the input and output of the calculated area are established (Figure 2.13).

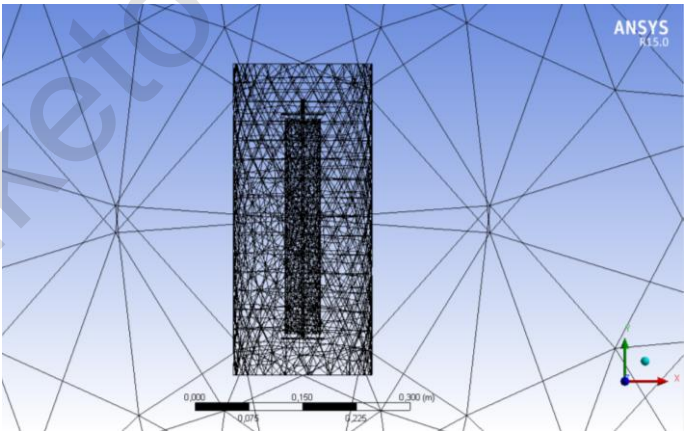

Fig.2.12. Finite-volume grids in the XY plane

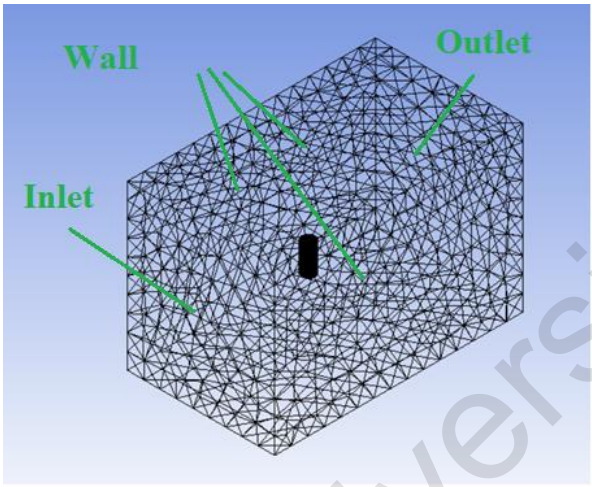

Fig.2.13. Boundary conditions

Later, the resulting model was imported into the Setup solver, where the turbulence model was selected, the parameters of the boundary conditions and the methods of the solver were set. The specified boundary conditions for performing the simulation are given in Table2.3.

Table 2.3.

The value of the specified boundary conditions

Boundary conditions	
At the entrance	
Type	The speed at the entrance
Initial pressure (Pa)	0
Flow rate m/s	3, 5, 7, 10, 15
Turbulent intensity (%)	5
Coefficient of turbulent viscosity	10
At the exit	
Type	Outlet pressure
Outlet pressure (Pa)	0

Return flow of turbulent intensity (%)	5
Coefficient of return flow of turbulent intensity (%)	10
Blade surface	
Type	Wall
The condition is sticking together	No sliding
Periodic conditions	
Type	Rotation
Blade rotation (rpm)	300, 500, 700

Turbulence model

To solve the simulation task of the flow of air around the rotating blade, a Realizable k-ε turbulence model with two equations averaged by Reynolds Navier-Stokes equations (RANS) was used. The term "Realizable-realizable" means that the model satisfies certain mathematical constraints on Reynolds stresses consistent with the physics of turbulent flows. The immediate advantage of the implemented k-model is that it more accurately predicts the propagation velocity of both flat and round jets. It is also likely to provide excellent performance for flows associated with rotation, boundary layers under strong adverse pressure gradients, separation and recirculation.

The turbulent energy equation (2.3):

$$\frac{\partial \rho k}{\partial t} + \frac{\partial \rho k u_j}{\partial x_j} = \frac{\partial}{\partial x_j}\left[\left(\mu + \frac{\mu_t}{\sigma_k}\right)\frac{\partial k}{\partial x_j}\right] + G_k - \rho\varepsilon \qquad (2.3)$$

Dissipation's specific rate equation of turbulent energy (2.4):

$$\frac{\partial \rho \varepsilon}{\partial t} + \frac{\partial \rho \varepsilon u_j}{\partial x_j} = \frac{\partial}{\partial x_j}\left[\left(\mu + \frac{\mu_t}{\sigma_\varepsilon}\right)\frac{\partial \varepsilon}{\partial x_j}\right] + \rho\varepsilon\left(C_1 S - C_2 \frac{\varepsilon}{k + \sqrt{\nu\varepsilon}}\right) \qquad (2.4)$$

Turbulent kinetic energy production $G_k = \mu_t S^2$, where $S = \sqrt{2S_{ij}S_{ij}}$ – strain rate tensor modulus (2.5):

$$C_1 = \max\left(0.43, \frac{\eta}{\eta+5}\right),\ \eta = S\frac{k}{\varepsilon},\ C_2 = 1.9. \qquad (2.5)$$

Turbulent viscosity coefficient $\mu_t = \rho C_\mu \frac{k^2}{\varepsilon}$,

where $C_\mu = \frac{1}{A_0 + A_s \frac{kU^*}{\varepsilon}}$, $U^* = \sqrt{S_{ij}S_{ij} + \Omega_{ij}\Omega_{ij}}$,

$\Omega_{ij} = \overline{\Omega_{ij}} - \varepsilon_{ijk}\omega_k$.

$\overline{\Omega_{ij}}$ – the vorticity tensor moving with angular velocity ω_k in the coordinate system.

$$A_0 = 4.04,\ A_s = 6\cos(\phi),\ \phi = \frac{1}{3}\cos^{-1}\left(\sqrt{6}W\right),\ W = \frac{S_{ij}S_{jk}S_{ki}}{\tilde{S}^3},$$

$$\tilde{S} = \sqrt{S_{ij}S_{ij}},\ S_{ij} = \frac{1}{2}\left(\frac{\partial u_i}{\partial x_j} + \frac{\partial u_j}{\partial x_i}\right),\ \Omega_{ij} = \frac{1}{2}\left(\frac{\partial u_i}{\partial x_j} - \frac{\partial u_j}{\partial x_i}\right)$$

ε_{ijk} – Levi-Civita tensor's components .

Turbulent Prandtl numbers $\sigma_k = 1$, $\sigma_\varepsilon = 1.2$.

Boundary conditions

The turbulent kinetic energy boundary conditions on the side are given as follows (2.6):

$$\frac{\partial k}{\partial n} = 0 \qquad (2.6)$$

and the velocity of scattering of turbulent kinetic energy in the side of the wall is estimated from the criterion of equivalence of kinetic energy production by turbulent fluctuations and its dispersal and the presupposition of the logarithmic distribution of the middle speed of the gas (2.7).:

$$\varepsilon_p = \frac{C_\mu^{0.75} k_p^{1.5}}{\kappa y_p} \qquad (2.7)$$

where κ=0.42. Value y_p this is the the distance of the cell center to the wall if $y_p > \frac{\mu}{\rho C_\mu^{0.25} k_p^{0.5}} y^*$, differently $y_p = \frac{\mu}{\rho C_\mu^{0.25} k_p^{0.5}} y^*$. Here $y^* = 11.225$

Entrance boundary conditions of the area (2.8), (2.9):

$$u_x = 0, u_y = 0, u_z = V \qquad (2.8)$$

$$\varepsilon = C_\mu^{0.75} \frac{k^{1.5}}{0.07 D_h}, \; k = \frac{3}{2}(V \cdot I)^2 \qquad (2.9)$$

where D_h – the entrance area hydraulic size was assumed to be 1 m.

I – The turbulent pulsations intensity was assumed to be equal 0.1.

Exit boundary conditions from the region: $p = p_{ex}$.

Boundary conditions on the blade walls: $u_i = U(t,x,y,z)$,

where $U(t,x,y,z)$ – the walls's movement speed, depending on the blade rotation speed.

The parameters of a given turbulence model are displayed in Figure 2.14.

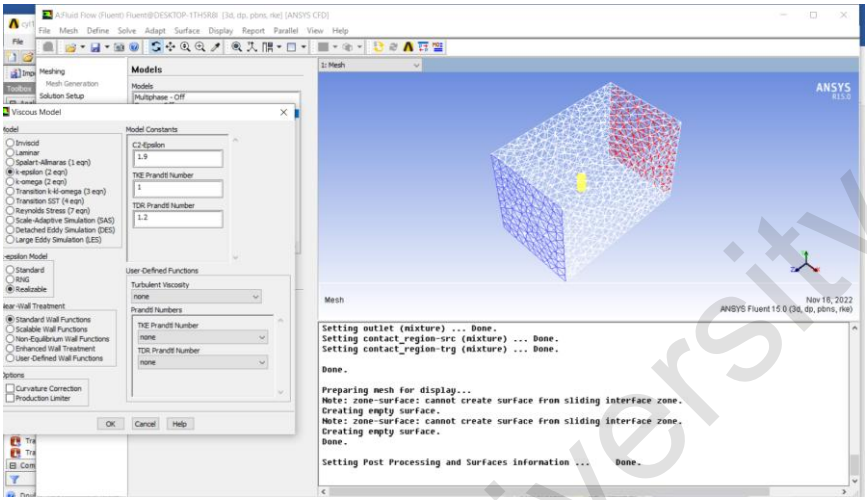

Fig.2.14. Turbulence model parameters

For the most accurate adjustment of the velocity and pressure fields, as well as to improve convergence, the SIMPLE algorithm was used, which is based on a semi-implicit scheme with splitting by physical processes.

To calculate the gradient of a given variable, FLUENT/ANSYS includes three different methods: based on Green-Gauss cells, based on Green-Gauss nodes, and based on least squares cells. In the presented study, the default program method based on least squares cells was chosen. The standard method is selected as the initialization method.

2.4. Results of mathematical modeling of the blade

During numerical simulation at air speeds of 5, 10, 15 m/s and at a rotational velocity of 300, 500, 700 rpm, three-dimensional patterns of airflow around the blade were obtained. (Figures 2.13-2.15).

The rotation of the blade was set along the y axis, clockwise. It's determined from the results obtained, the wind velocity field is deformed. Near the center of rotation of the blade, the air flow

velocity vectors have a swirling motion, outside the rotational region, the flow behind the blade coincides with the main air flow. The maximum air flow velocity created by the blade rotation rises everytime by 5-7 m/s.

On the left side of the painting there is a panel with a gradation of colors from the minimum speed, which is indicated in blue to the maximum speed, indicated in red. The air flow velocity was set manually, and was equal to 5.10 and 15 m/s. As can be seen from the drawings, there is a slowdown in the air flow behind the blade, which is shown by the blue velocity vectors.In the case when the flow accelerates, this phenomenon is shown in the figure with red vectors. This trend corresponds to the law of conservation of momentum and mass.

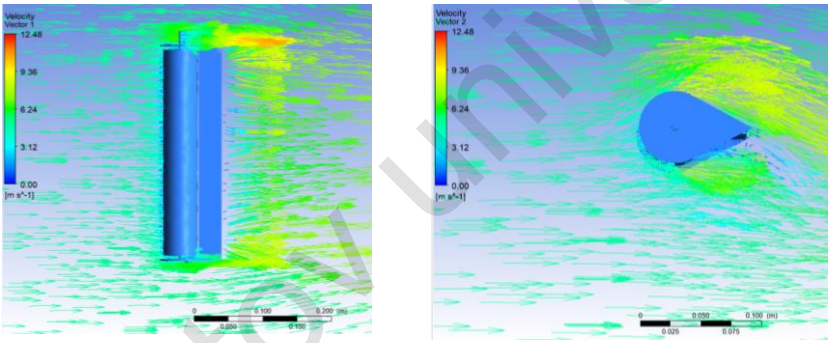

a) V=5 m/s, n=300 rpm

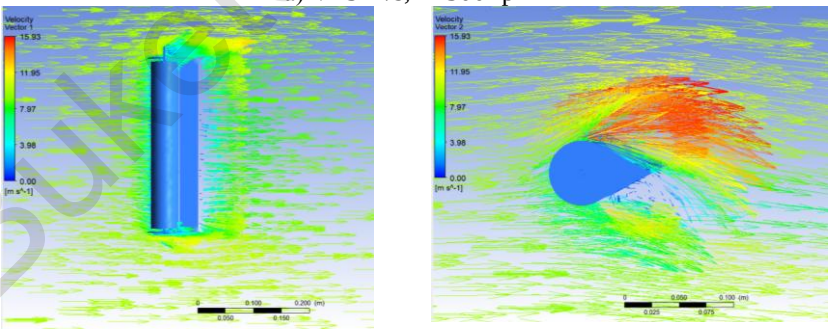

b) V=10 m/s, n=300 rpm

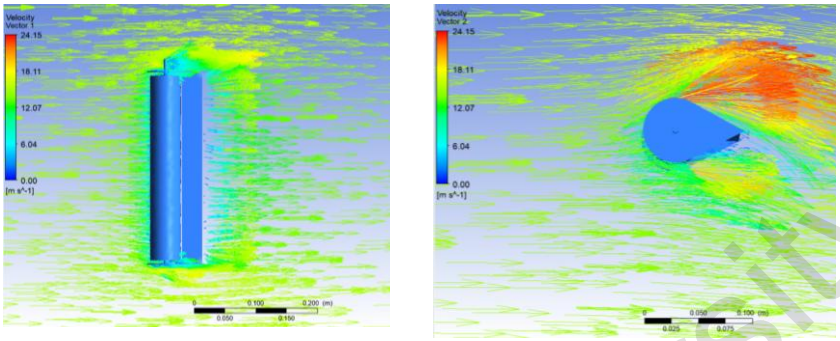

c) V=15 m/s, n=300 rpm

Fig.2.15. The velocity field around the blade at n = 300 rpm, and at 5,10,15 m/s

It is determined that from Figures 2.15 a, 2.16 a and 2.17 a, at flow velocities of 5 m/s, vortex formation is observed on the opposite side to the direction of rotation of the blade, in which the instantaneous angular velocity of rotation of the particle medium is not zero. With increasing rotation speed of the blade, vortex formation increases at a given speed. In the future, there is an increase in lifting force and drag force due to unwinding and attenuation of the intensity of vortex formation in the wake of the blade.

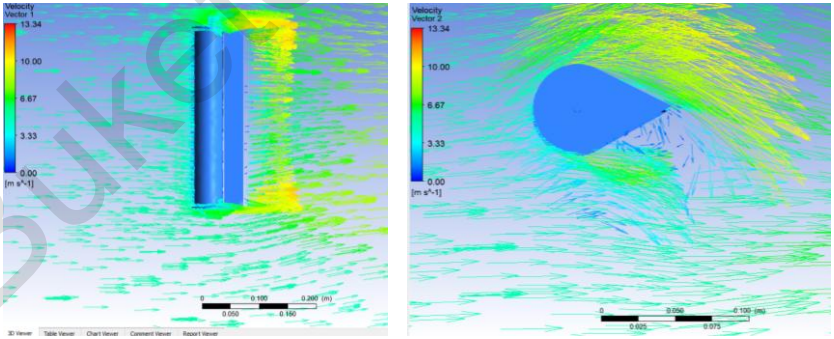

a) V=5 m/s, n=500 rpm

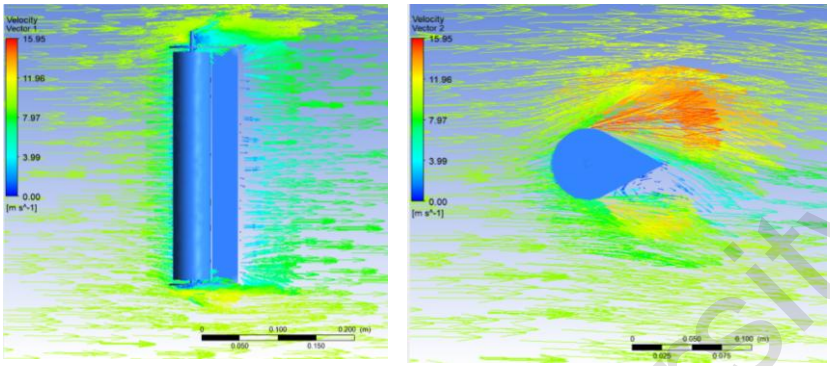

b) V=10 m/s, n=500 rpm

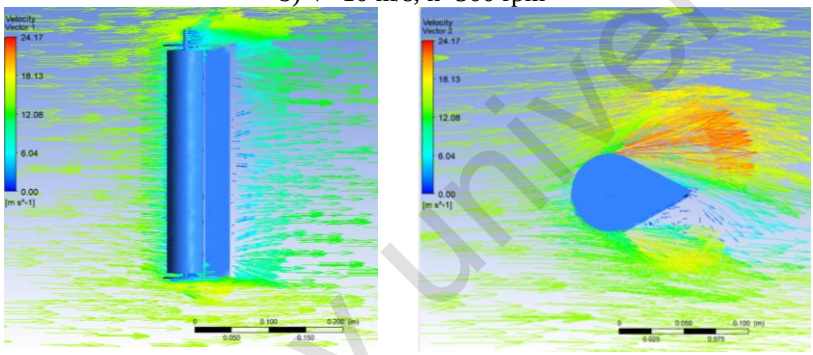

c) V=15 m/s, n=500 rpm

Fig.2.16. The velocity field around the blade at n = 500 rpm, and at 5,10,15 m/s

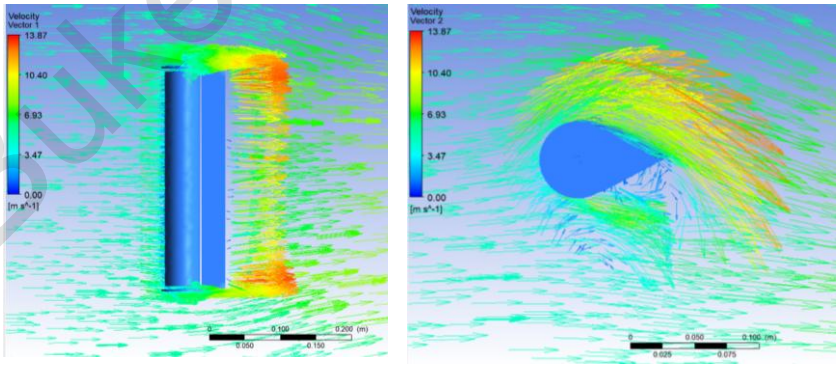

a) V=5 m/s, n=700 rpm

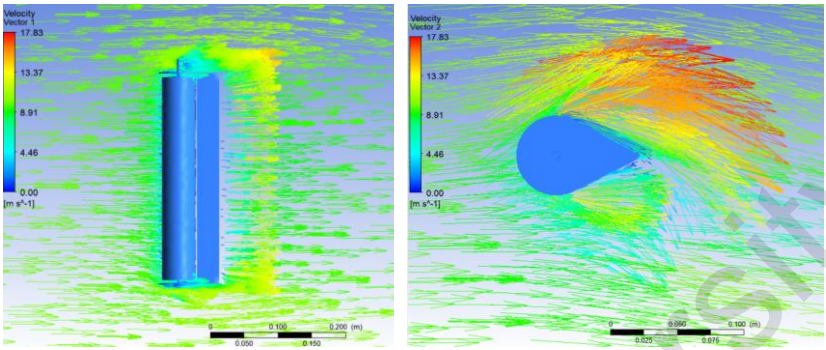

b) V=10 m/s, n=700 rpm

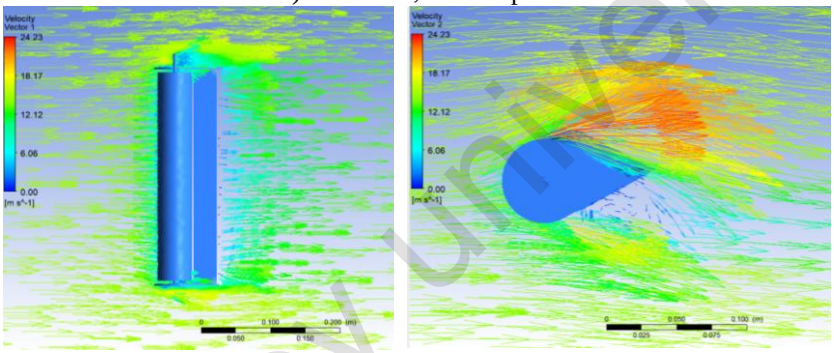

c) V=15 m/s, n=700 rpm

Fig.2.17. The velocity field around the blade at n = 700 rpm, and at 5,10,15 m/s.

The next pictures 2.18-2.20 demonstrate the results of the distribution of static pressure (pst = p – patm) around the rotating blade of a wind turbine. The results were achieved at the air velocities of 5.10 and 15 m/s and at the blades rotation speed of 300, 500 and 700 rpm.

The legend panel in the figure on the left side represents a color gradation from blue, which is the lowest pressure, to red.

The flow direction was from left to right. When the blade rotates, there is a pressure difference between the front surface and the back. Due to the cylindrical surface of the blades, the pressure difference (force) generates torque. It is showed that the blade face

has a higher pressure, while the corresponding back side has a lower pressure.

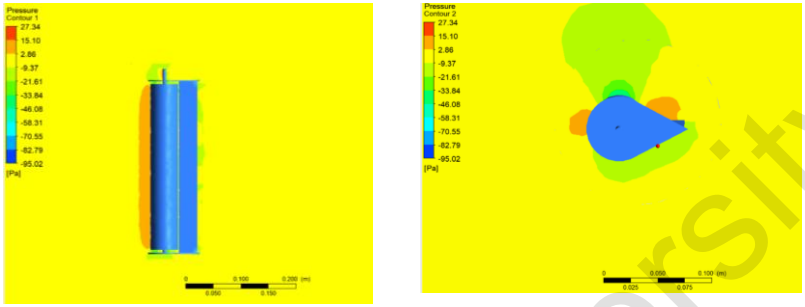

a) V=5 m/s, n=300 rpm

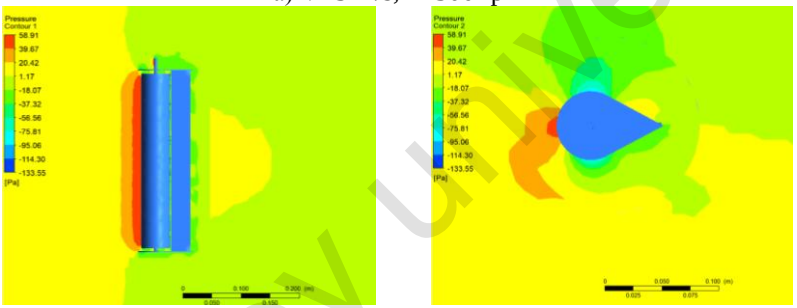

b) V=10 m/s, n=300 rpm

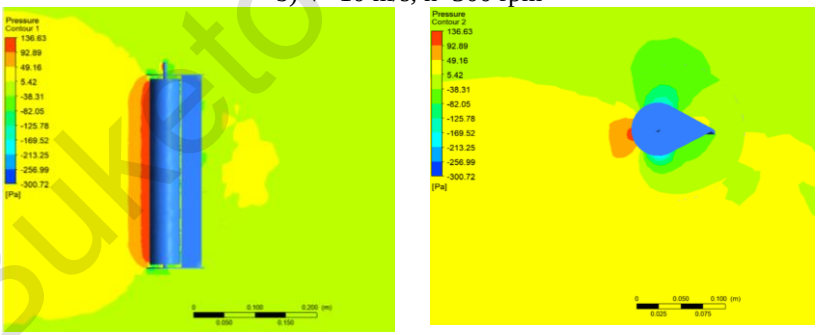

c) V=15 m/s, n=300 rpm

Fig.2.18. The pressure distribution field around the blade at n = 300 rpm, and at 5,10,15 m/s

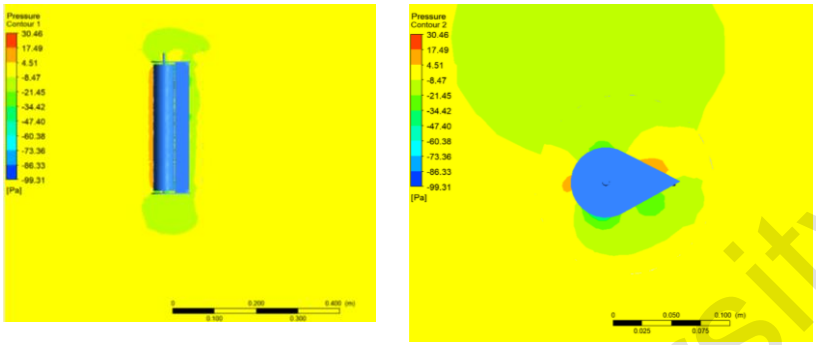

a) V=5 m/s, n=500 rpm

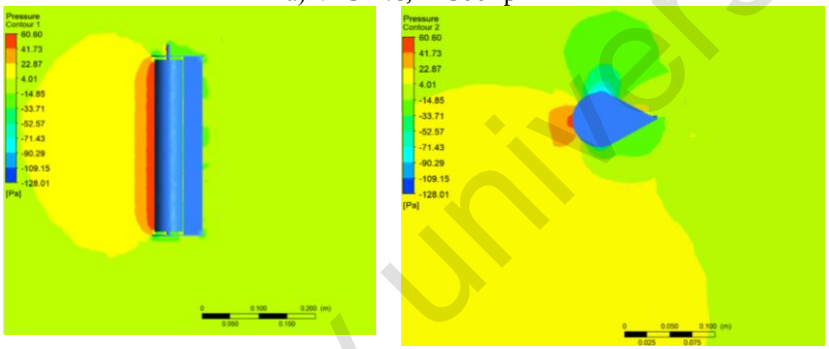

b) V=10 m/s, n=500 rpm

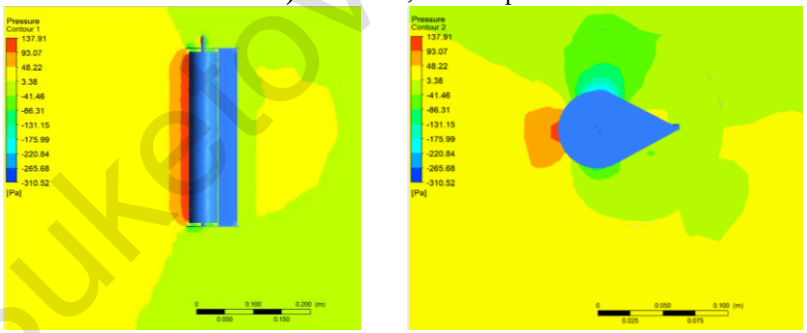

c) V=15 m/s, n=500 rpm

Fig.2.19. The pressure distribution field around the blade at n= 500 rpm, and at 5,10,15 m/s

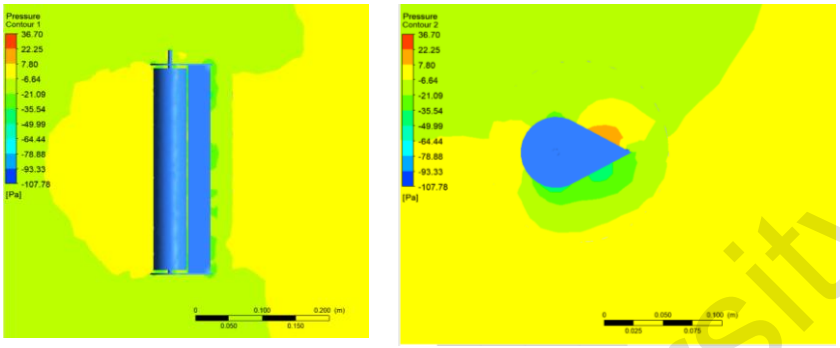

a) V=5 m/s, n=700 rpm

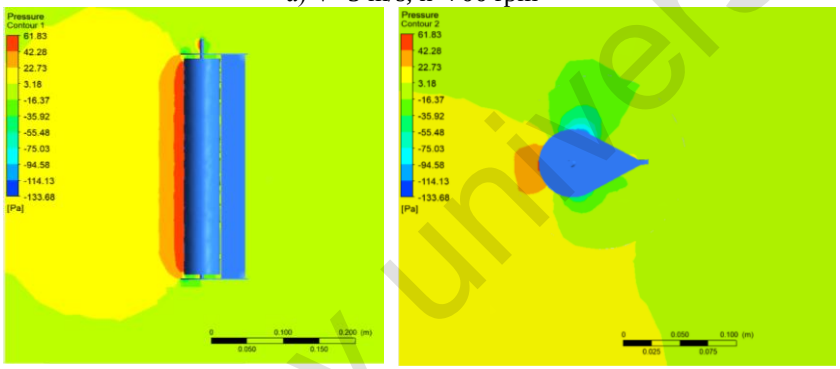

b) V=10 m/s, n=700 rpm

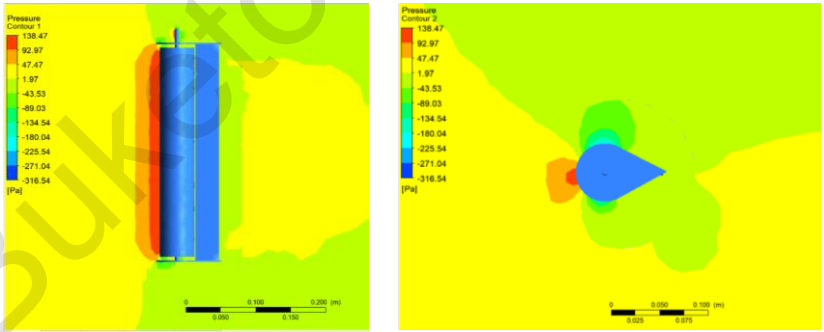

c) V=15 m/s, n=700 об/мин

Fig.2.20. The pressure distribution field around the blade at n= 700 rpm, and at 5,10,15 m/s

According to Bernoulli's law, kotoraya established a relationship between the speed of the flow and the flow, in the zone above the paragliding static flow rate. I go out of Urga, in the region where the green Urga is shown in color with low meanings, and the static formation of a rising (force Magnus) power. Glasslike canberransfact the Magnus, the lifting force, forming a series of cylindrical bodies in the fairing of the airspeed, the flow of the air is perpendicular to the direction of the flow.

At speeds of 5 m / s, the significance of the relative remains almost unchanged, and the increase of the part of the enclosures is negligible. Definitely, at part 300 rpm, the range of changes lies in the range from -95.02 Pa to 37.34 Pa, at 500 rpm from -99.31 Pa to 30.46 Pa and at 700 rpm from -107.78 Pa to 36.70 Pa.

As the air flow velocity increases, the range of pressure changes expands. So, at an air flow rate of 10 m / s and at a speed rotation 300 rpm, it ranges from -133.55 Pa to 58.91 Pa, and at 500 rpm from -128.01 Pa to 60.60 Pa, and at 700 rpm from -133.68 Pa to 61.83 Pa. Due to the rotary movement, the is changing the pressure field at the ends of the blades. It is identified from the figures, the max pressure is seen from the downwind side of the blade, while the minimum pressure is concentrated on the leeward side.

At a maximum set flow velocity of 15 m/s, the following results were obtained: static pressure change: at 300 rpm from -300.72 Pa to 136.63 Pa, at 500 rpm -310.52 Pa to 137.91 Pa and at 700 rpm -316.54 Pa to 138.47 Pa.

3 MATHEMATICAL MODELING OF A HORIZONTAL-AXIAL WIND POWER PLANT WITH TWO AND THREE BLADES

3.1. Creation of a three-dimensional model of a wind power plant with two blades

Currently, mathematical modeling is widely used to solve engineering problems related to the wind turbine blades aerodynamics [45-49]. In the computational study, the flow structure around a wind turbine is studied using numerical methods of gas dynamics based on solving a system of Navier Stokes equations. The use of mathematical equations to solve the flow makes it possible to significantly reduce time and material costs, compared with the experiment [49-55].

The first stage for conducting mathematical modeling of wind turbine flow is the construction of a geometric model. In the course of numerical studies, a three-dimensional model of a two-bladed WPP was created [55-61].

The WPP model with combined blades made in the construction of fixed blades and cylinders, a central shaft on which the working power elements are fixed, as well as a mast on which the main shaft is fixed.

The geometric dimensions the of the numerical simulation are presented in Table 3.1.

Table 3.1.

WPP model geometric dimensions

Parameters	**Value**
Cylinder length	205 mm
Cylinder diameter	50 mm
The length of the fixed blade	225 mm
Width of the fixed blade	25 mm
Wind wheel diameter	500 mm
Mast length	420 mm

To study the effect of the fixed blade inclination angle on the aerodynamic features of the entire wind power plant, mathematical models with different positions of the fixed blade have been created.

Figure 3.1 shows how a fixed blade forms an angle (0°, 15°, 30°, 45°, 60°) relative to the distance of the cylinder rotation axis.

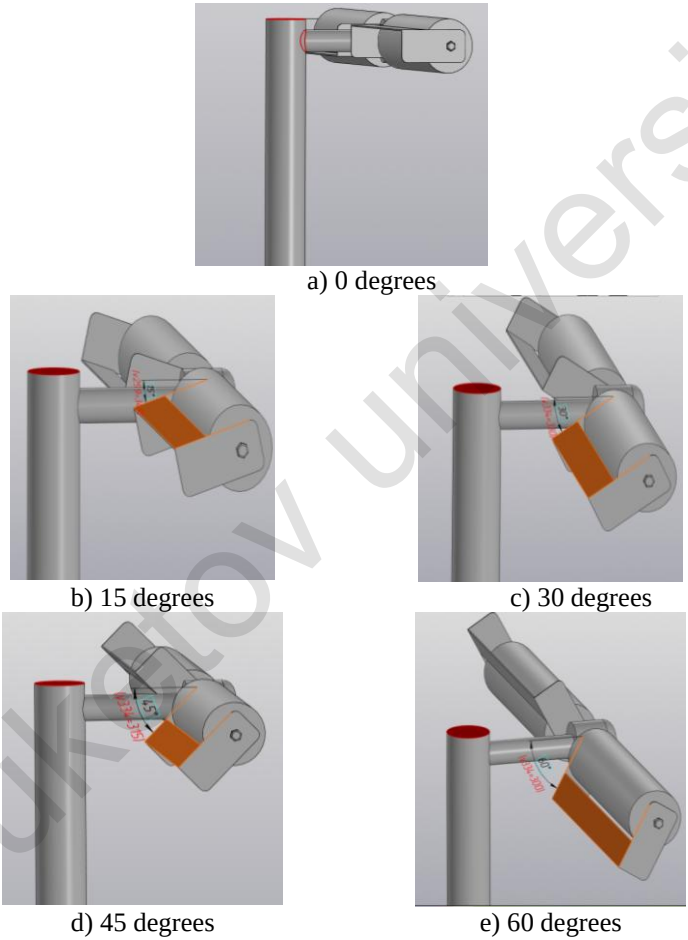

a) 0 degrees

b) 15 degrees

c) 30 degrees

d) 45 degrees

e) 60 degrees

Fig.3.1. The arrangement of the blades at different angles

The initial stage of mathematical modeling is the creation of computational areas around the mathematical model to set boundary conditions and rotation conditions. A cylindrical subdomain (1) with a thickness of 5 mm has been created around each power element to set the conditions for the rotation of the blades, a cylindrical subdomain (2) with radii of 0.1 m around the z axis has been created around the cylindrical subdomains, as well as an area in the form of a parallelepiped (3) with dimensions of 0.7 m; 0.7 m; 1.5 m; 0.7 m;0.7m; 3m around the cylindrical subdomain (2) (Figure 3.2) to rotate the entire conditions of the wind wheel. Figure 3.3 shows a finite-volume grid of wind turbines obtained in the Ansys Meshing routine.

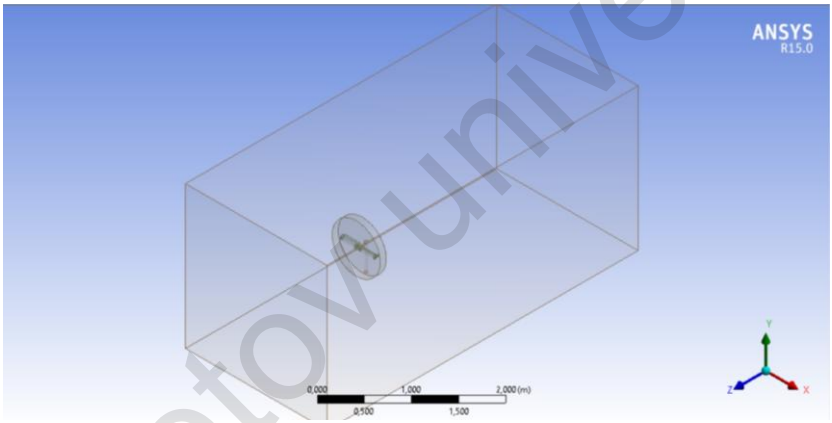

Fig. 3.2. A model of a WPP with calculated areas

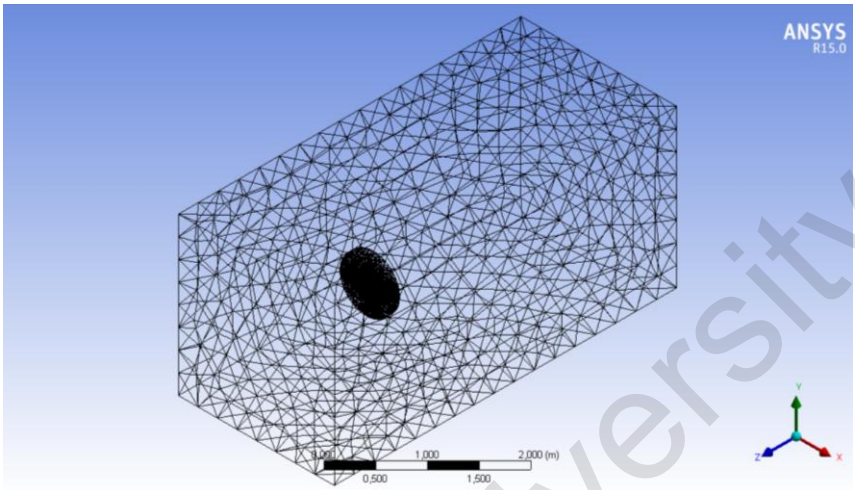

Fig.3.3. Of course-a three-dimensional grid

The grid consists of tetrahedra, the number of which is 269842.

3.2. Creation of a three-dimensional model of a wind power plant with three blades

Modeling the flow around a wind wheel with combined blades is a complex numerical task. In order to numerically study the stream around a three bladed WPP, a geometric model was created using the Design Modeler program and a 3D COMPASS (Figure 3.4). To study the effect of the inclination angle of the fixed blade on the aerodynamic features of the entire wind power plant, mathematical models with different positions of the fixed blade have been created (0°, 15°, 30°, 45°, 60°).

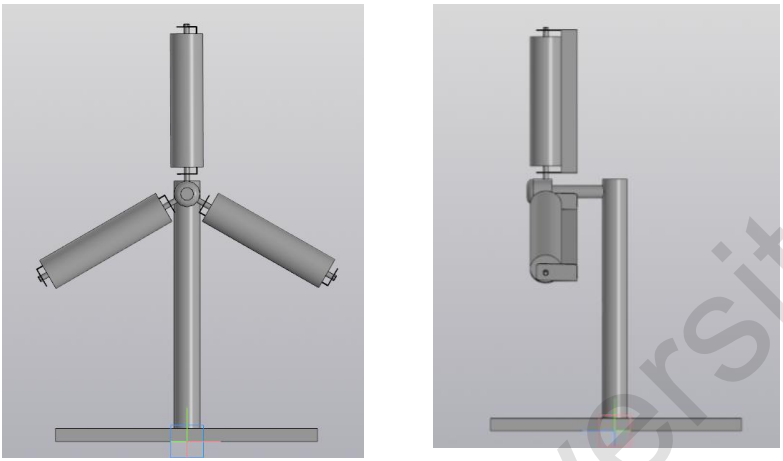

a) 0 degrees

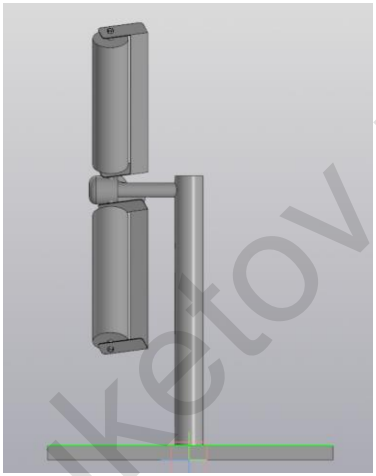

b) 15 degrees

c) 30 degrees

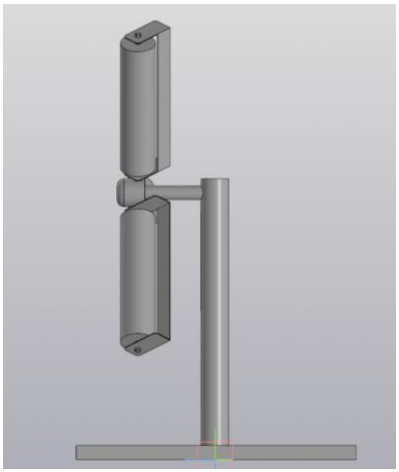

d) 45 degrees

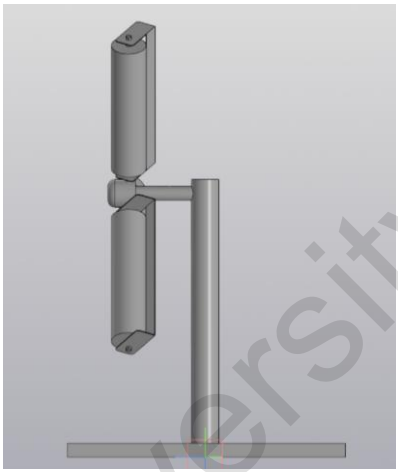

e) 60 degrees

Fig.3.4. Geometrical models of a three-bladed WPP with various inclination angle of a fixed blade

Figure 3.5 below demonstrates a three-bladed mathematic model WPP with estimated areas and boundary conditions

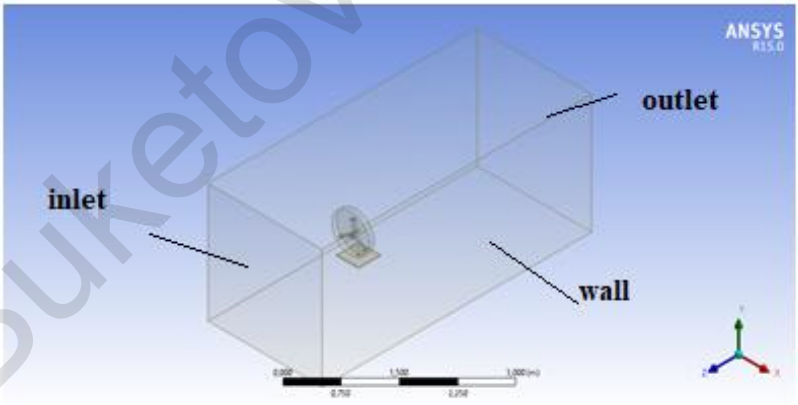

Fig.3.5. Mathematical model of a 3-blade WPP

It is determined that from Figure 3.5, the creation of computational areas around the mathematical model for setting boundary conditions and rotation conditions is performed similarly to the above-described operation algorithm for a 2-blade wind turbine. A distinctive feature is the setting of rotation conditions, since the blades are located at an angle of 120 degrees. The . axes of rotations of the blades are set (0, 1, 0), (cos(π/6), –sin(π /6), 0), (–cos(π /6), –sin(π /6), 0). The wind wheel rotation is established around the z axis.

3.3. Basic assumptions

1. Because of the Mach numbers small value (the proportion of the gas speed to the regional velocity of sound, M<<0.1), the air is described by formulas that are valid for an incompressible medium.

2. Owing to the high Reynolds numbers (the proportion of inertial forces to viscosity forces, Re $>10^4$), the stream is turbulent.

3. Owing to the small value of the coincidences numbers and minor temperature changes in the wind wheel vicinity, the current is isothermal.

3.4 A formulas system of describing the air stream running around a wind wheel

$$\frac{\partial u_j}{\partial x_j} = 0 \qquad (3.1)$$

$$\frac{\partial \rho u_i}{\partial t} + \frac{\partial \rho u_i u_j}{\partial x_j} + \frac{\partial p}{\partial x_i} = \frac{\partial \tau_{ij}}{\partial x_j} \qquad (3.2)$$

where $\tau_{ij} = (\mu + \mu_t)\left[\frac{\partial u_j}{\partial x_i} + \frac{\partial u_i}{\partial x_j}\right]$ – stress tensor;

3.5. Choosing a model of turbulence for mathematical calculation of the airflow field

The choice of a turbulence model depends on the nature of the turbulent flow, the required accuracy, available computing resources [61-72], and the time required for the modeling process. To adequately select a turbulence model, it is necessary to clearly understand the properties and limitations of each turbulence model. In our case, the Realizable k-ε turbulence model (system of equations 2.1-2.5) is chosen as the model.

3.6 Boundary conditions

The turbulent kinetic energy boundary conditions on the side are defined as follows (3.3):

$$\frac{\partial k}{\partial n} = 0 \qquad (3.3)$$

and the velocity of dispersion of turbulent kinetic energy in the side of the wall is computed from the criterion of equivalence of kinetic energy production by turbulent fluctuations and its dispersal and the presupposition of the log-distribution of the middle speed of the gas (3.4).:

$$\varepsilon_p = \frac{C_\mu^{0.75} k_p^{1.5}}{\kappa y_p} \qquad (3.4)$$

where κ=0.42. Meaning y_p this is the length from the centre of the cell wall to the wall, if $y_p > \frac{\mu}{\rho C_\mu^{0.25} k_p^{0.5}} y^*$, else $y_p = \frac{\mu}{\rho C_\mu^{0.25} k_p^{0.5}} y^*$. Here $y^* = 11.225$

Boundary conditions at the access to the zone (3.5), (3.6):

$$u_x = 0, u_y = 0, u_z = V \qquad (3.5)$$

$$\varepsilon = C_{\mu}^{0.75} \frac{k^{1.5}}{0.07 D_h}, \; k = \frac{3}{2}(V \cdot I)^2 \qquad (3.6)$$

where D_h – – the hydraulically sized entrance area of the site is 1 m was assumed; I – it was supposed that the rate of turbulent fluctuations is equal to 0.1;

Boundary conditions at the outlet of the area: $p = p_н$.

Boundary conditions on the side walls of the wind turbine: $u_i = U(t,x,y,z)$,

where $U(t,x,y,z)$ – the speed of wall movement depends on the rotation speed of the working cylinders around their own axial length and the rotation speed of the cylinders around the axis of the wind turbine.

Methods of solution of a set of formulas (3.1-3.5)

The set of formulas (3.1-3.5) is resolved in the Ansys-Fluent software package using the finite volume method and the method of multiple (nested) coordinates systems.

Of course, the three-dimensional grid built in type 1 subdomains consist of hexagonal cells, and in type 2 and type 3 subdomains it consisted of tetragonic cells.

To estimate the convective terms of the system of equations (3.1-3.2), a countercurrent difference scheme of the second order of accuracy in space was used. The middle difference system was used to estimate the second-order derivations. A simple scheme was employed to match the pressure field and the velocity field. Time derivative is estimated with the second order of accuracy.

3.7 Simulation results of a wind power plant with horizontal axis of rotation

3.7.1. Simulation of aerodynamic characteristics of wind power plants

This chapter shows the time-averaged values of the drag force of all combined blades, the lifting force acting on one blade, the moment of force acting on the wind wheel, and the coefficient of drag and lift of one blade obtained for a moveable wind wheel.

The time average was carried out using the formula:

$$\langle f \rangle = \frac{1}{T} \int_0^T f(t)\,dt\,.$$

The value of the averaging timeslot T was selected to be from 3 s to 5 s, that considerably outweighs the time period of rotation of the cylinders around its own axis, equaling 0.02 s at a minimum rotation speed of 300 rpm.

The results of the drag force obtained during mathematical modeling as a function of wind speed and the inclination angle of the fixed blade for a WPP with two blade is illustrated under (Figures 3.6-3.10).

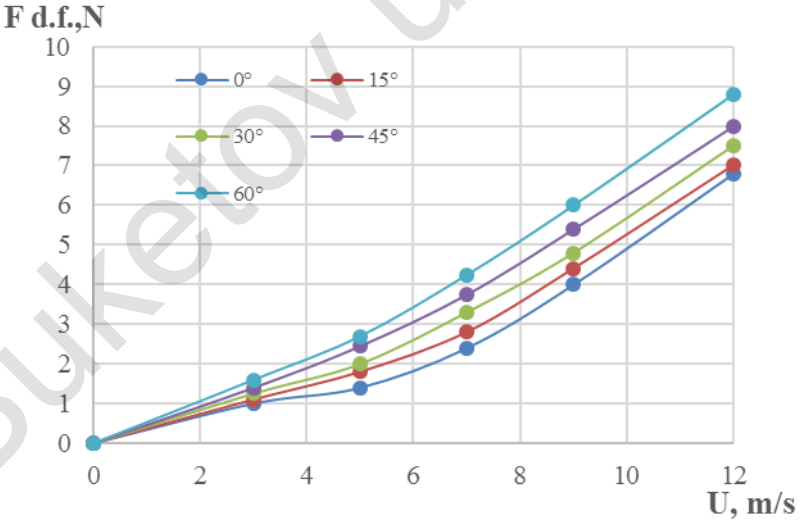

Fig.3.6. The relation of the drag force to the stream velocity at various inclination angles the fixed blade for two bladed WPP

It is determined from Figure 3.6 that the resistance force grows steadily with an increasing rate of stream speed, as also with an increase in the inclination angle of the fixed blade. The drag force grows with each rise in the angle of inclination of inclination is about 0.3- 0.4 N. It was found that at an angle of 0°, the layout has a minimum drag and maximum lift.

Figure 3.7 below displays the result of the thrust force measurement of the layout depending on the flow rate.

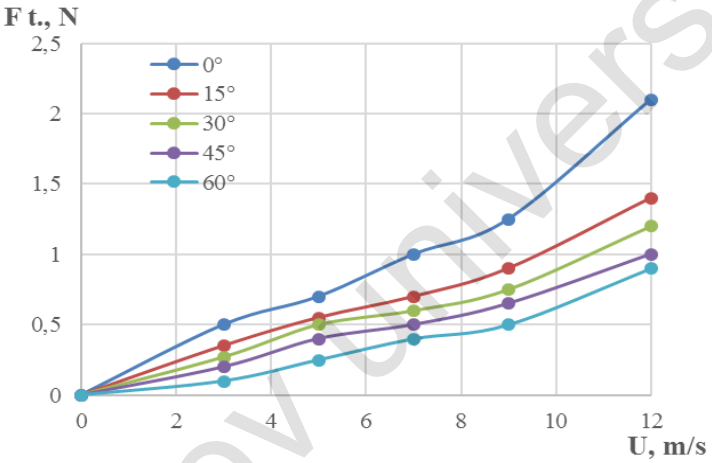

Fig.3.7. The relation of the thrust force to the stream speed at various inclination angles of the fixed blade

From Graph 3.7 it is found that, the max value of 2.1 N thrust force at 12 m/s was obtained when the fixed blade relative to the cylinder was positioned at an angle of 0 °. In the future, there is a sharp decrease in the thrust force of 1.4 N at a wind speed of 12 m/s and at an angle of 15 °. With an increasing of inclination angle in increments of 15 °, the thrust force meaning decreases by 0.1-0.05 N.

Figures 3.8-3.10 display the outcomes of the calculated aerodynamic coefficients depending on the Reynolds number.

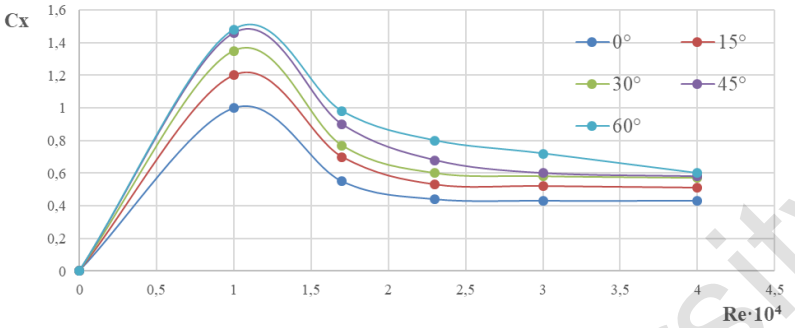

Fig.3.8. Dependence of the drag coefficient on the Reynolds number at various inclination angles

From Graph 3.8 it is determined that, when the fixed blade is positioned relative to the cylinder at an angle of 0 degrees, optimal values of the lift coefficient of 0.04 are obtained with a Reynolds number of $1 \cdot 10^4$.

Next, a graph of the dependence of the moment of forces acting on a movable wind turbine with two and three blades on the velocity of the incoming flow is constructed numerically (Figures 3.9, 3.10).

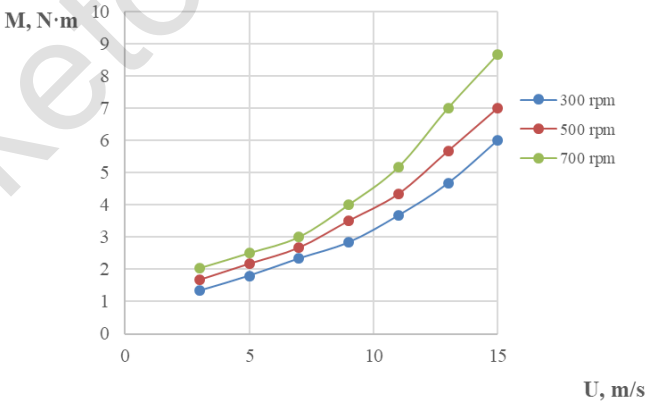

Fig.3.9. Dependency graph of the moment of forces acting on a movable wind wheel with two blades on *U, m/s*

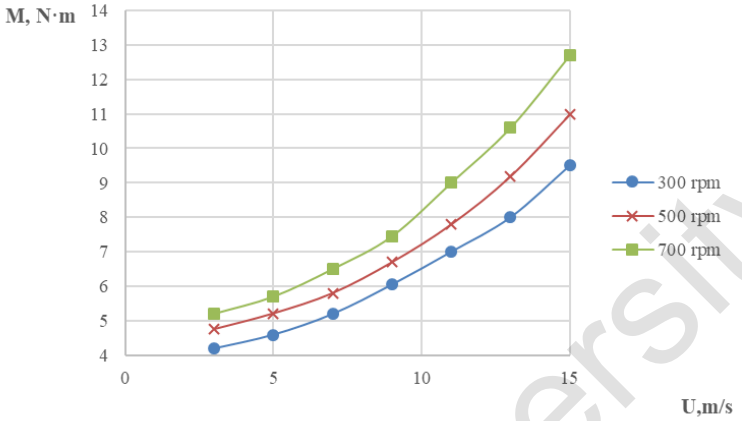

Fig.3.10. Dependency graph of the moment of forces acting on a movable wind wheel with three blades on the velocity of the incoming flow

From Graph 3.9 it is determined that, the value of the moment of forces increases in a straight line with increasing wind flow velocity. The maximum torque value of a two-bladed wind power plant is 8.6 Nm at a wind speed of 15 m/s and at a blade rotation speed of 700 rpm.

From Figure 3.10, it is determined that a three-bladed wind wheel with a blade rotation speed of 700 rpm produces 46% more torque than a two-bladed wind wheel. The difference between the values of the moment of forces between them is about 4 Nm.

Next, the calculation of the wind energy utilization coefficient ξ (WEUC) was carried out. The WEUC depends on the velocity of the ground and the wind direction.

The following formula was used to determine the WEUC (3.7):

$$\xi = \frac{N_r - N_c}{N_{wf}}, \qquad (3.7)$$

where $N_c = mM_c\omega_c$ – cylinder rotation power, m – number of cylinders; M_c – the moment of forces acting on the rotating cylinder; ω_c – angular velocity of cylinder rotation; $N_{wf} = \frac{\rho u^3 S}{2}$ – wind flow power, ρ – the density of the air in the incoming flow; $S = \pi R^2$ – the area of the midsection of the rotor;R- the radius of the rotor; u – incoming flow rate, $N_r = M_r\omega_r$ – rotor rotation power, M_r – the moment of forces acting on the movable rotor; n – the number of cylinders revolutions; N – the wind wheel speed rotation; ω_r – the free rotation angular velocity of rotor or the rotor rotational power is equal to $N_r = M_r \frac{2\pi n_1}{60}$.

Figures 3.11 and 3.12 below demonstrate the results of the WEUC from the speed (speed coefficient).

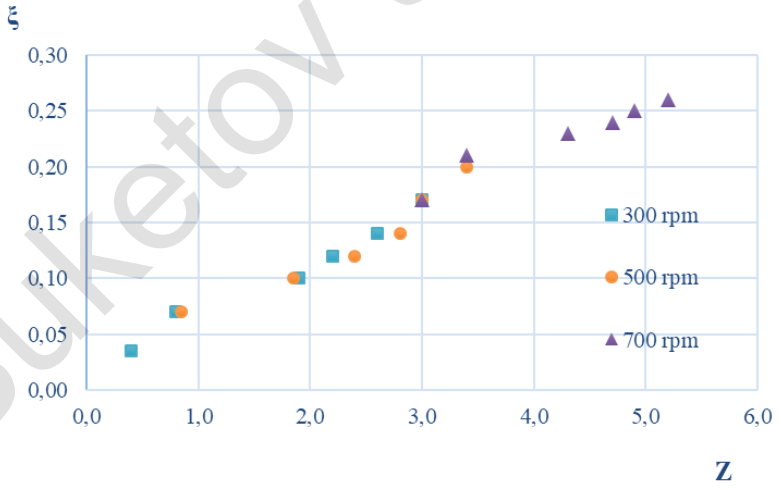

Fig.3.11. The dependence of the WEUC on the speed (speed coefficient) for a two-bladed WPP

From Graph 3.11 it is found that, the WEUC of a wind power plant can be represented by a power-law function of speed :

$$\xi = 0{,}0713 \cdot Z^{0{,}713}$$

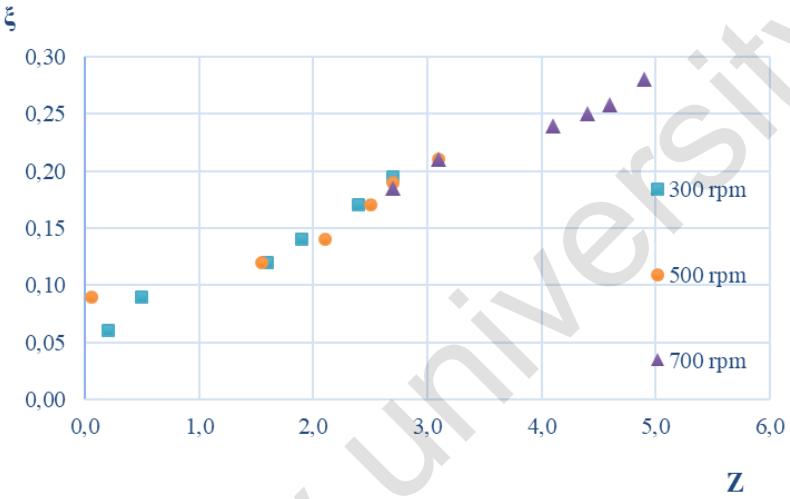

Fig.3.12. The dependence of the WEUC on the speed (speed coefficient) for a three-bladed wind turbine

The design of a three bladed WPP can be represented by a power-law function of speed:

$$\xi = 0{,}1147\ Z^{0{,}409}$$

It is established that the number of blades affects the energy efficiency of wind turbines. From Graphs 3.11 and 3.12 it is found that, the WEUC three-bladed wind turbine is almost 7-8% larger than the two-bladed wind turbine. The speed of a WPP with three blade is 6-7% lower than a two-bladed one. It is established that each speed value corresponds to a certain value of the wind energy utilization coefficient.

3.7.2 Obtaining a flow pattern and pressure distribution of wind turbine with two blade

Figures 3.13 show flow patterns of a rotating wind wheel with two blades at n =300 rpm and different wind speeds.

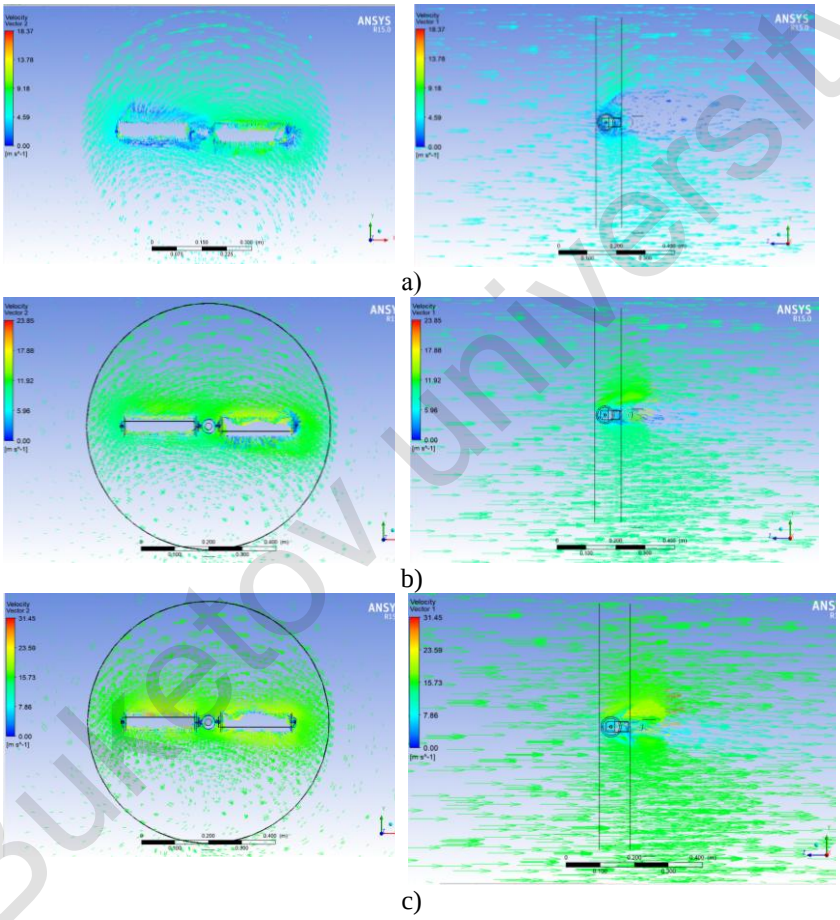

Fig.3.13. The WPP flow diagram at n = 300 rpm:
a) at u = 5 m/s; b) u= 10 m/ s; c) u=15 m/s

From figure 3.13 it is determined that, in the upper left corner there is a color gradation from blue (minimum) to red (maximum), which is a panel of symbols. The rotation axis of the combined blades corresponds to the x axis. The wind wheel rotates round the z axis. The wind wheel rotation direction is determined in a clockwise direction.

When the wind wheel is subjected to the influence of airflow on the blades, aerodynamic forces arise that cause the wind wheel to rotate. It is determined that vortex formation is formed behind the central shaft of the wind wheel. The air pressure in the jet increases as it approaches the wind wheel, but drops sharply when passing through the wind wheel. A certain vacuum is formed behind the wind wheel, which gradually disappears in the future.

Figures 3.14 below show the flow patterns of a wind turbine at n=700 rpm.

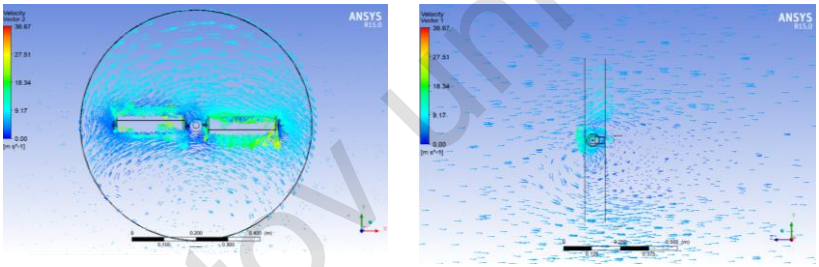

a)

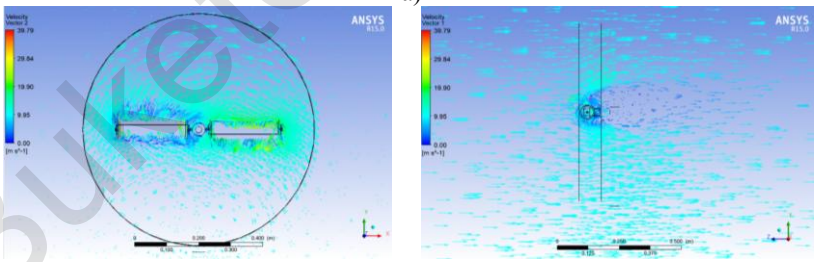

b)

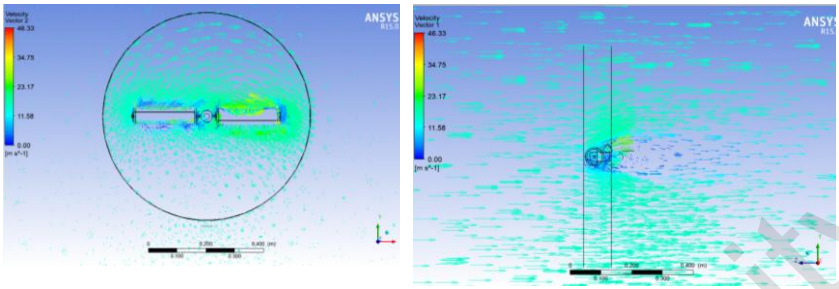

c)

Fig.3.14. Flow pattern of a wind turbine at n=700 rpm:
a) at u=5 m/s; b) u=10 m/s; c) u=15 m/s

From figure 3.14 it is determined that, at high rotation speeds of the blades and the wind wheel, a vortex is formed behind the central part of the wind wheel increases at a given speed. The direction of the the incoming flow of air is directed from left to right along the z axis. In the future, there is an increase in lifting force and drag force due to unwinding and damping the intensity of vortex formation in the wake of the wind wheel. Due to the decrease in intensity behind the wind wheel, the torque increases, including the lifting force of the wind turbine.

Figures 3.15 and 3.16 below show the results of modeling wind turbines with a fixed blade at an angle of 30 degrees at n =300 rpm and 700 rpm.

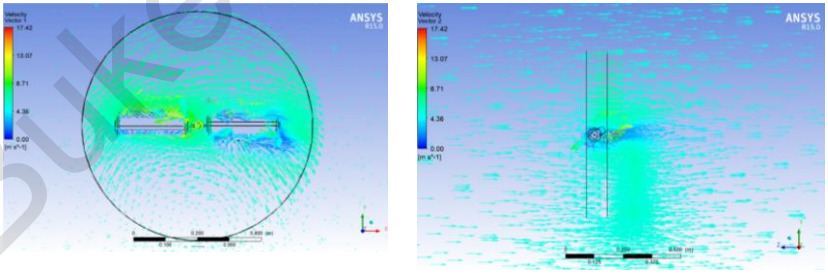

a)

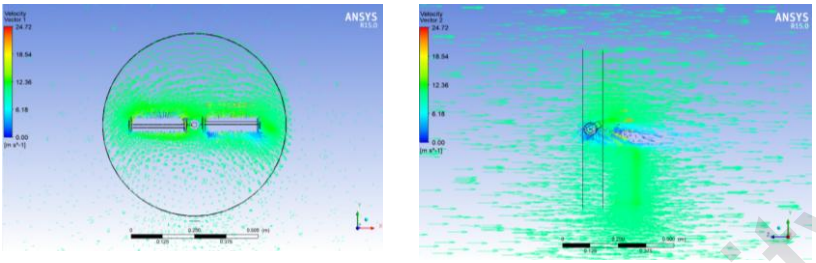

b)

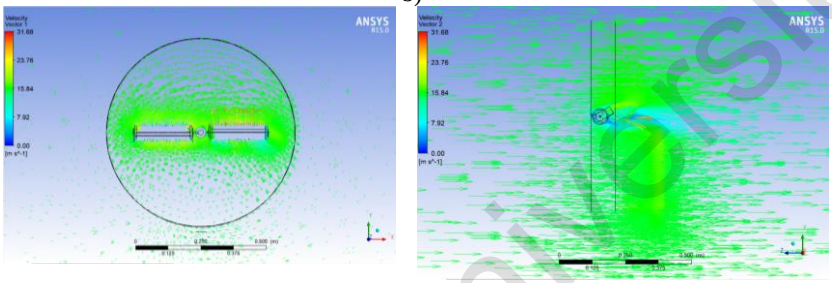

c)

Fig. 3.15. Flow pattern of a wind turbine at n=300 rpm:
a) at u=5 m/s; b) u=10 m/s; c) u=15 m/s

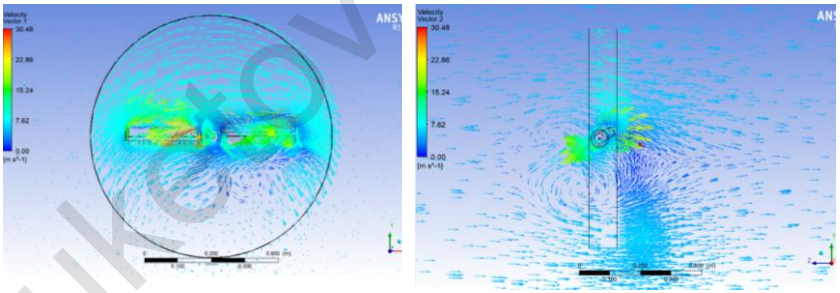

a)

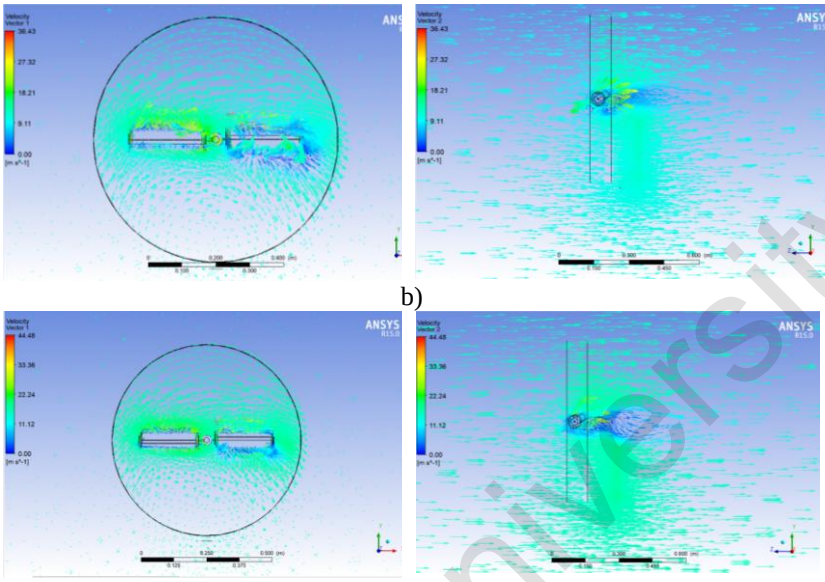

Fig.3.16. Flow pattern of a wind turbine at n=700 rpm:
a) at u=5 m/s; b) u=10 m/s; c) u=15 m/s

From figures 3.15 and 3.16 it is determined that, when the fixed blade is positioned at an angle of 30 degrees, the flow is disrupted, that is well apparent at the max rotation velocity of the blades and the wind wheel.The reason for this disruption is the separation of the boundary layer caused by its braking at an unfavorable pressure gradient. Since the turbulent flows arising from the rotating combined blade have counterflows, the lifting force of the wind turbine itself drops sharply. A drop in lift entails a decrease in the WPP efficiency. On this principle, a suitable inclination angle of the fixed blade is established. is an angle of 0 degrees for a two-bladed wind turbine.

Figures 3.17-3.18 below show pressure distribution patterns around a rotating wind wheel at a fixed blade angle of 0 and 30 degrees.

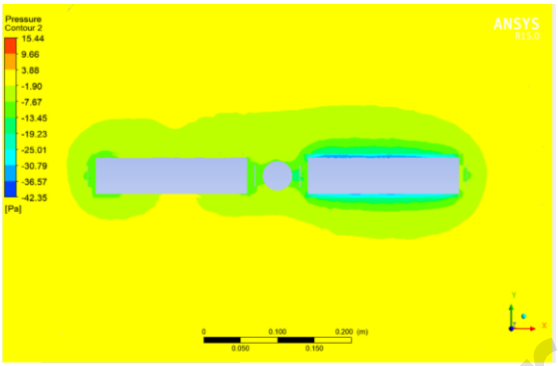

a)

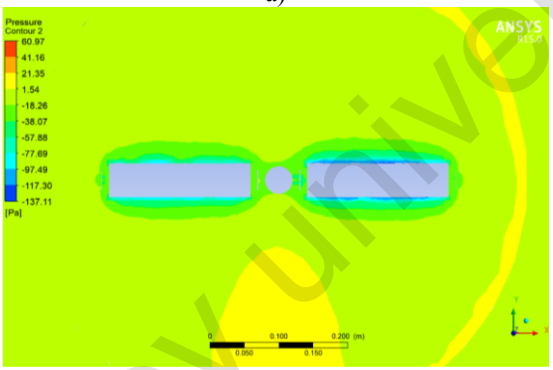

b)

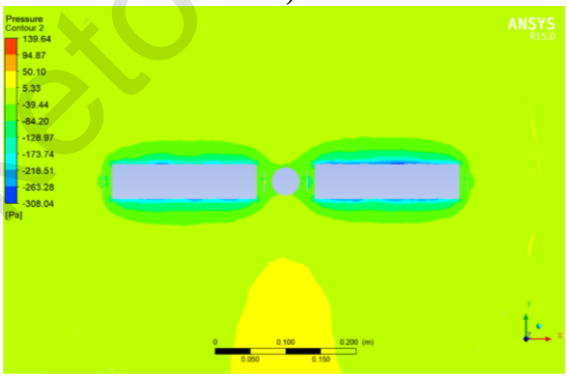

c)

Fig.3.17. Pressure distribution around a rotating wind wheel with a fixed blade at 0 degrees at n=500 rpm:
a) u=5 m/s; b) u=10 m/s; c) u=15 m/s

From figures 3.17 it is found that, the pressure range arising around the rotating wind wheel varied from -308.04 Pa to 139.64 Pa at maximum flow modes at n= 500 rpm.

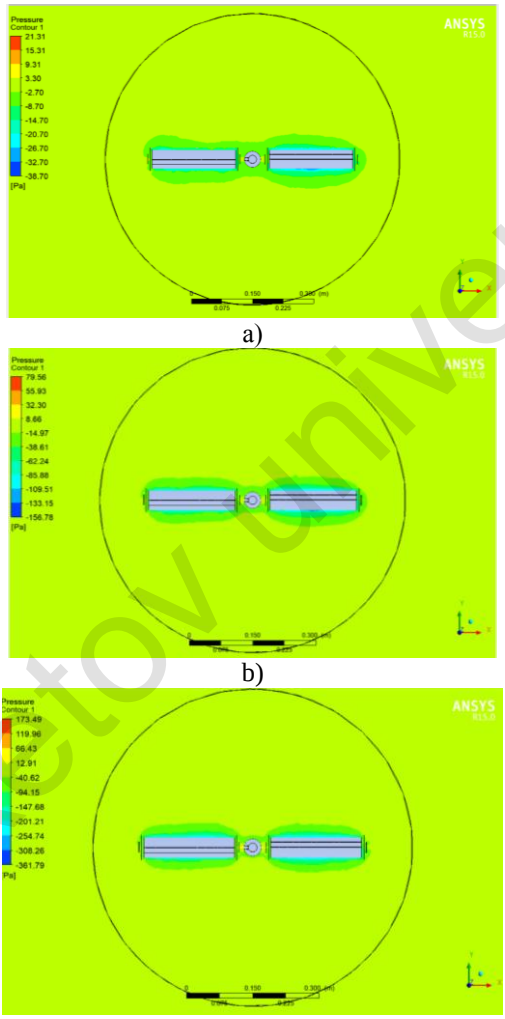

Fig.3.18. Pressure distribution around a rotating wind wheel with a fixed blade at 30 degrees at n=500 rpm:
a) u=5 m/s; b) u=10 m/s; c) u=15 m/s

From figures 3.18 it is determined that, the pressure value around a rotating wind wheel with a fixed blade at 30 degrees at a minimum flow velocity and blade rotation frequency (n=500 rpm and u=5 m/s) ranged from -38.48 Pa to 21.30 Pa. because of the adverse pressure gradient, the boundary layer is torn off due to the braking of the wind wheel.

3.7.3 Obtaining a flow pattern and pressure distribution of wind turbine with three blade

Figures 3.19-3.20 below demonstrate the results of the stream flow diagram of a three-bladed wind wheel with a fixed blade at an angle of 0 degrees at n =300 and 700 rpm and u = 5, 10 and 15 m/s.

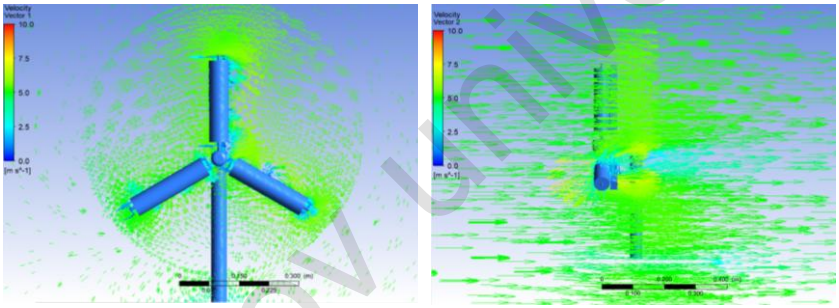

a)

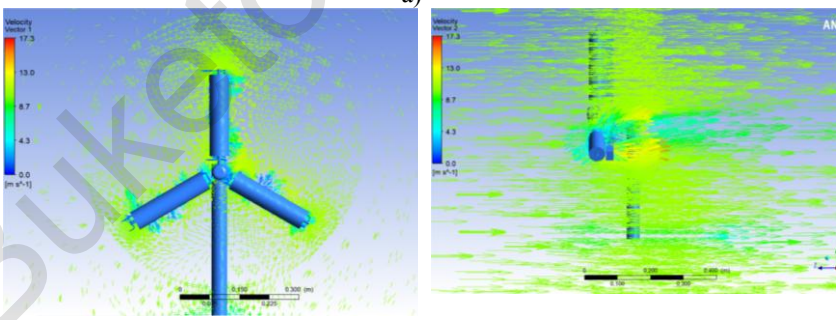

b)

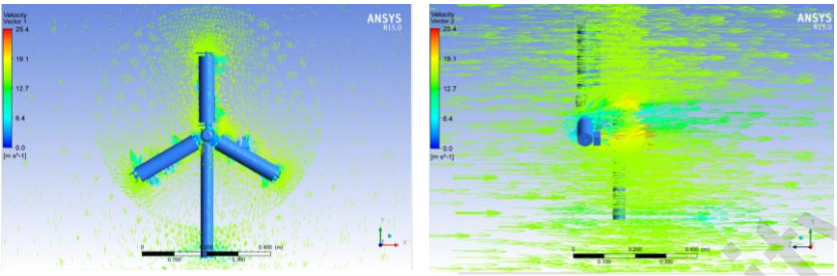

c)

Fig.3.19. Flow pattern of a wind power plant at n=300 rpm:
a) at u=5 m/s; b) u=10 m/s; c) u=15 m/s

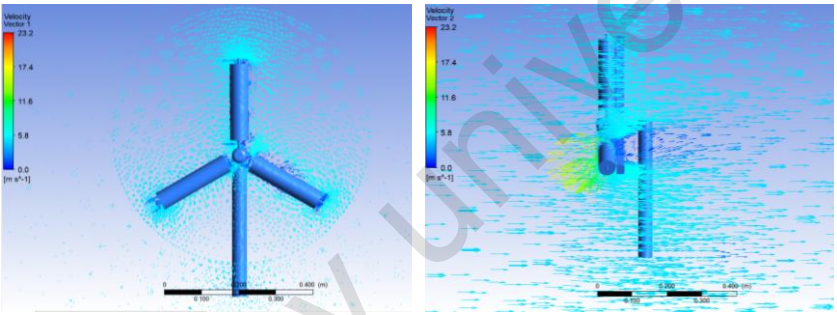

a)

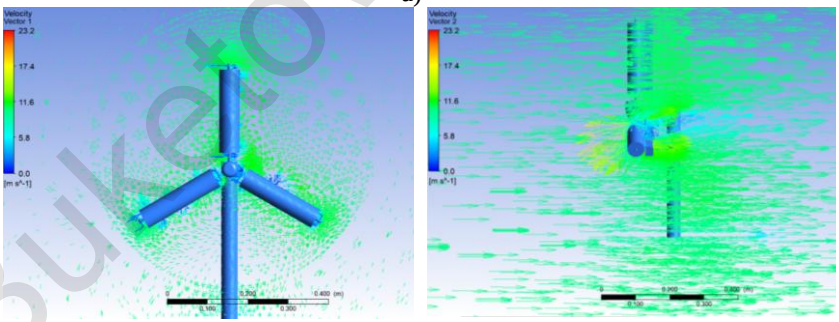

b)

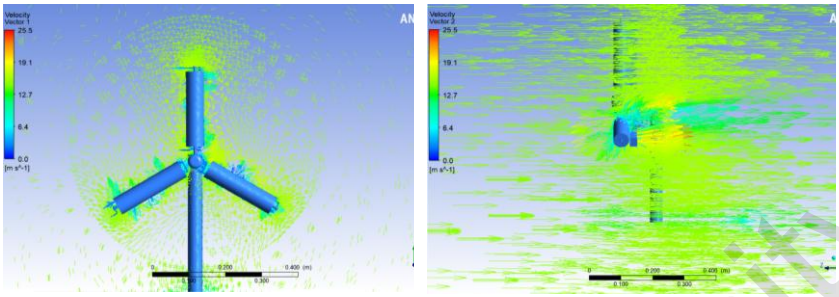

c)

Fig.3.20. Flow pattern of a wind turbine at n=700 rpm:
a) at u=5 m/s; b) u=10 m/s; c) u=15 m/s

From figures 3.19 and 3.20 it is determined that at low speeds, the velocity field remains symmetrical relative to the three planes, but with increasing air flow velocity, the formation of vortices behind the rotating blades is observed, due to the formation of a turbulent wake behind the wind wheel. The physical explanation for this is that turbulent vortices increase due to the creation of kinetic energy of turbulence due to large gradients of average velocity.

When air passes through a rotating wind wheel, the moment of inertia tends to decrease, thereby forming a local viscous region in which the wind speed decreases downstream from the rotor of the wind wheel. This region in a wind turbine is known as a footprint, which is a continuous large-scale turbulent coherent structure comprising coupled vortices and ordered vortex components in a spatial range

In the case when the power elements rotate counterclockwise, a pattern is observed when the air flow velocity is greater than the flow velocity on the other, based on this, there is a distortion of the flow field around the entire wind wheel.

Figures 3.21 demonstrate the pressure allocation results about the wind wheel at n=500 rotations per minute and u=5,10 and 15 m/s.

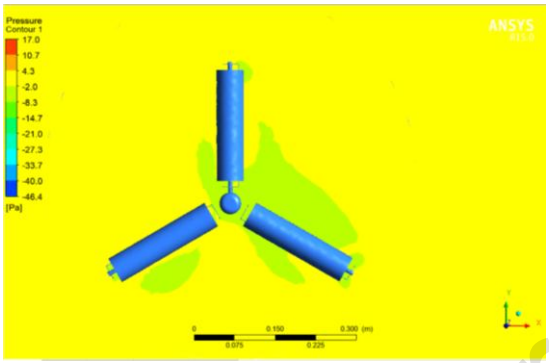

a)

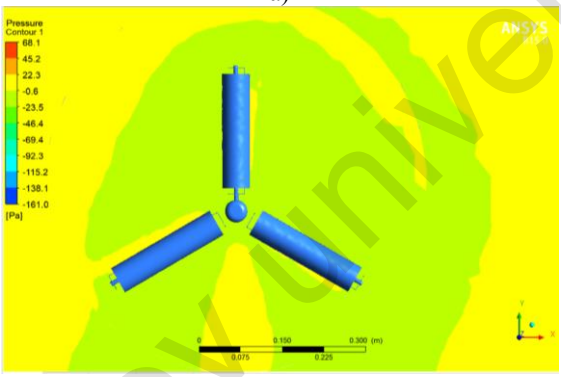

b)

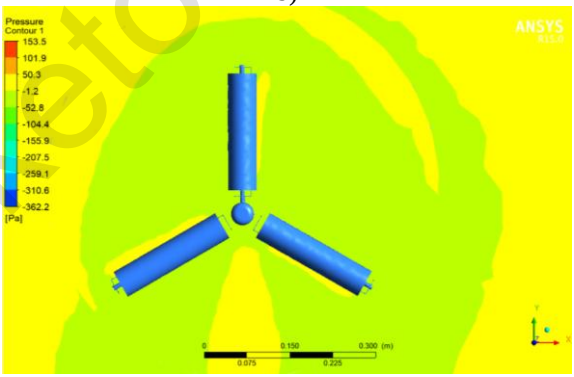

c)

Fig.3.21. Pressure allocation results about the wind wheel at n=500 rotations per minute and u=5,10 and 15 m/s

It is determined from Figure 3.21 that the low pressure region branches above the surface from the downwind side blade, and the high pressure region branches from the downwind of the blade as a result of flow acceleration.

As a result of the formation of turbulent vortices, a low pressure area is formed.

Figures 3.22-3.23 below show the results of mathematical modeling of a wind wheel with a fixed blade at an angle of 30 degrees under different flow regimes.

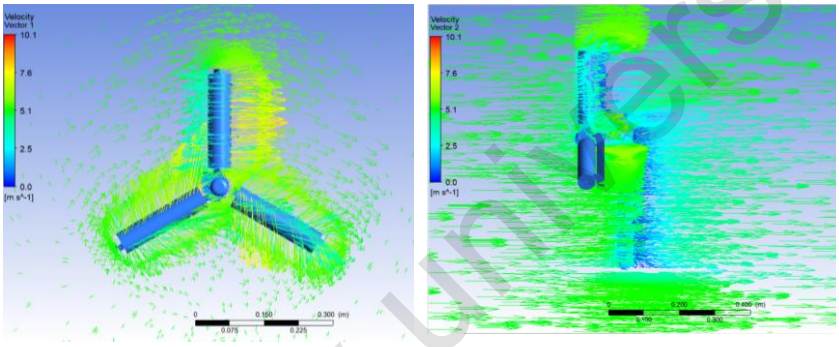

a)

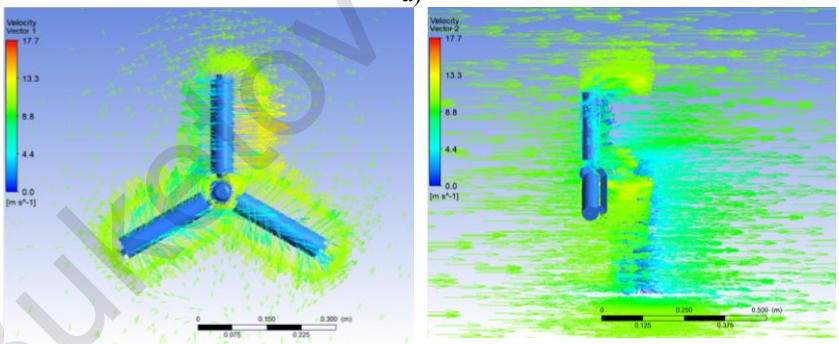

b)

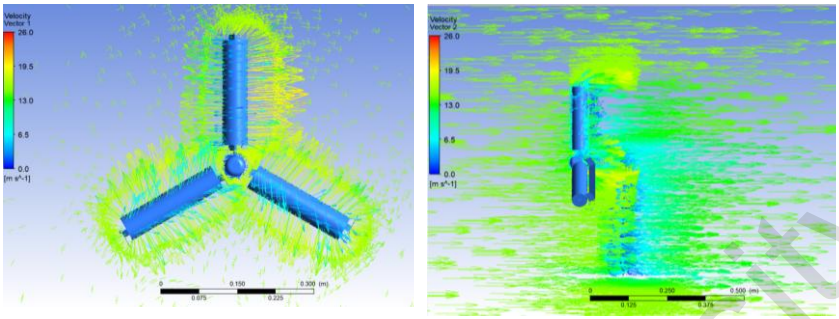

c)

Fig.3.22. The velocity field around the rotating wind wheel when the fixed blade is positioned at an angle of 30 degrees at n= 300 rpm:
a) at u = 5 m/s; b) u = 10 m/s; c) u= 15 m/s

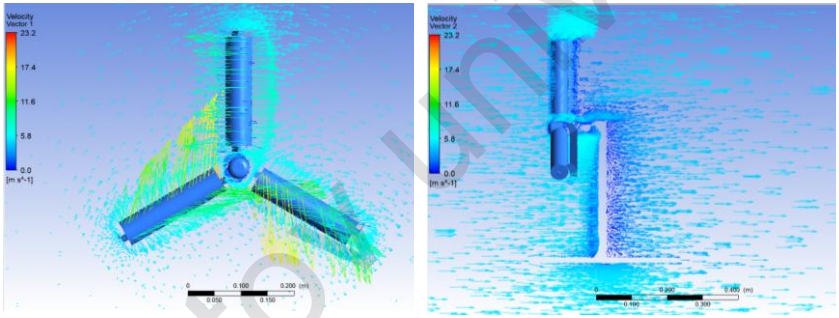

a)

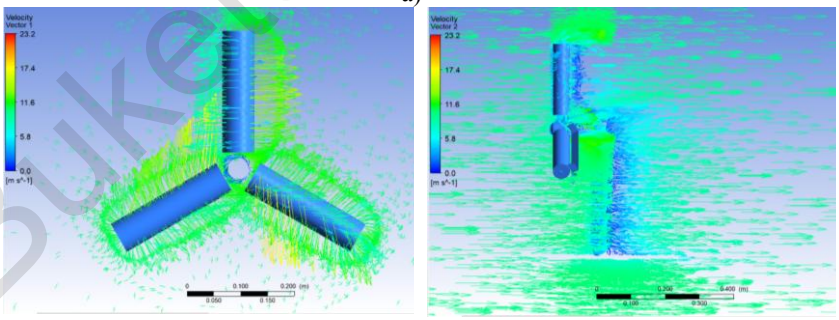

b)

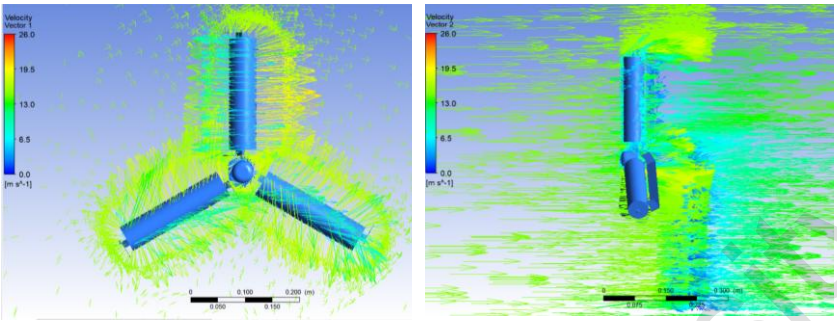

c)

Fig.3.23. The velocity field around the rotating wind wheel when the fixed blade is positioned at an angle of 30 degrees at n= 700 rpm: a) at u = 5 m/s; b) u = 10 m/s; c) u= 15 m/s

It is determined from Figures 3.22-3.23 that, when the fixed blade inclination angle rises, the full downwind side and ends of the blades turn out to be in the zone of stall flow, which is expressed in the form of braking of the WW and premature loss of thrust at full rotation.

It is determined that a strong vortex motion occurs around the wind wheel, due to an increase in the angle of inclination of the fixed blade relative to the rotating cylinder, which in turn increases the aerodynamic loads on the entire system of blades, i.e. the wind wheel.

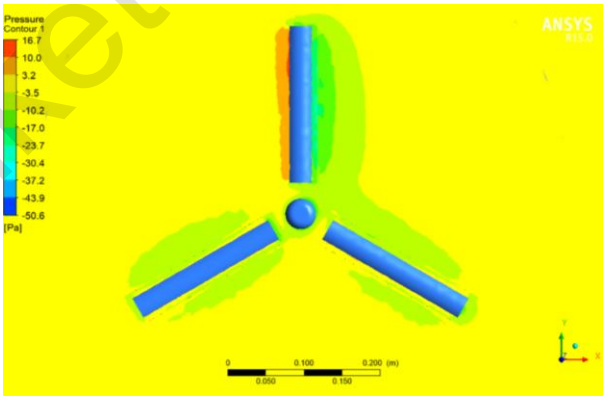

a)

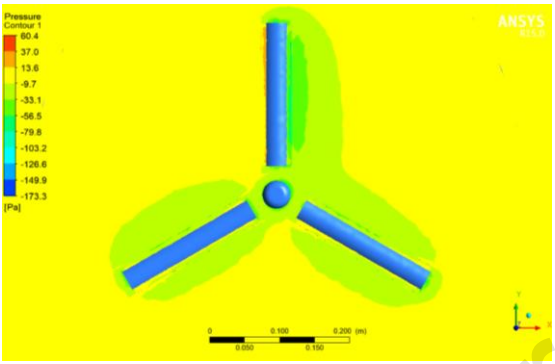

b)

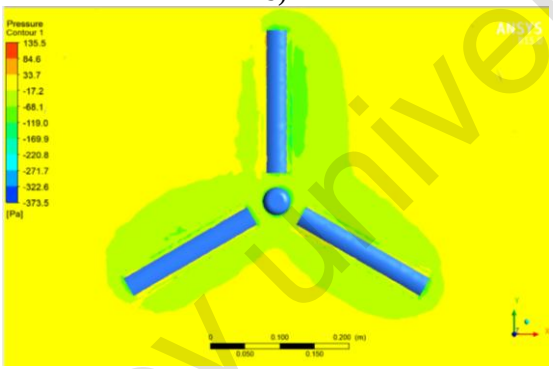

c)

3.24. The picture of pressure distribution when the fixed blade is positioned at an angle of 30 degrees and at n = 500 rpm:
a) at u = 5 m/s; b) u = 10 m/s; c) u = 15 m/s

Figure 3.24 shows the physical cause of the flow disruption at the ends of the blades, which is formed due to a positive pressure gradient along the chord of the profile with a boundary layer. The growth of the fixed blade location determines this interaction.

4 MATHEMATICAL MODELING OF A VERTICAL-AXIAL WIND POWER PLANT WITH THREE BLADES

4.1 Description of a vertical-axial wind power plant with three blades

Figure 4.1 shows a wind turbine with three vertical cylinders rotating relative to their own axes.

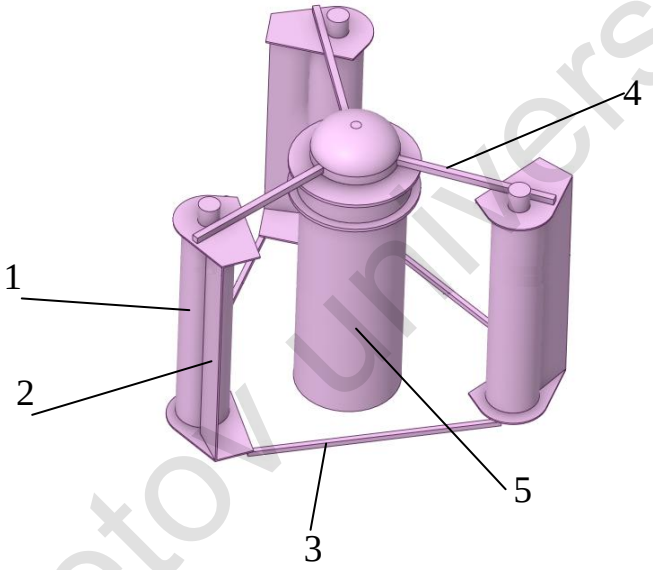

Fig.4.1. Wind turbine with vertical rotating cylinders

1 – rotating cylinder; 2 – vertical blade; 3, 4 – retaining rods; 5 – wind turbine support

WPP geometric features are accepted as follows.
Dimensions of rotating cylinders:
• Diameter 0.15 m
• Height 0.69 m
Blade sizes:
• Thickness 0.005 m

• Height 0.715 m
• Width 0.1182 m

Dimensions of the retaining rods:

• Cross section of the upper rods 0.03 m x 0.03 m
• The cross section of the lower rods is 0.015 m x 0.015

The spacing between theWPP support axis and the cylinder axis is 0.5 m.

The angle between the rotating cylinders, when projected onto a plane, forms 120°, i.e. together they form a regular triangle.

4.2 Methods for solving the system of equations 2.1-2.5

4.2.1 Sliding grid method

The presented equations (2.1)-(2.5) are solved by methods such as finite volume and sliding grid methods included in the Ansys-Fluent software package[72-84].

The separated 3 types of subdomains collectively form the entire calculation area. (Fig. 4.2).: fixed outer region 1, which is a ring with an outer radius of 2.5 m and an inner radius of 0.8 m; rotating region 2, which is a circle with a radius of 0.8 m; rotating regions around cylinders 3.

The calculations used a difference grid containing 24555 quadrangular cells, shown in Figure 4.3. In the fixed region 1, Fig.4.3, 2,771 cells were built, in the rotating region 2, Fig.1.2, 17,836 cells were built, in the rotating region of cylinder 3, Fig.4.3, 1316 cells were built.

The mesh was thickened near the walls of the cylinders, blades and supports. To estimate the convective members of the system of equations (2.1)-(2.2), a second-order countercurrent divergence scheme of precision in space was used.

The central difference scheme was employed to estimate second-order derivatives. The coupled scheme was employed to coordinate the pressure and the velocity fields. Time derivatives are estimated with first-order accuracy. The time step was set to $4 \cdot 10^{-4}$ s.

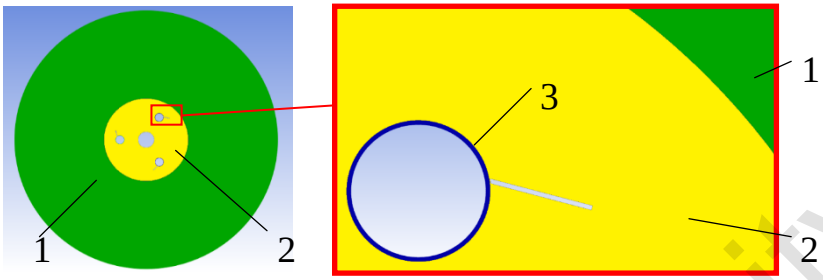

Fig.4.2.Calculation area
1 – external stationary area; 2 – rotating area of the wind turbine;
3 – rotating area of the cylinder

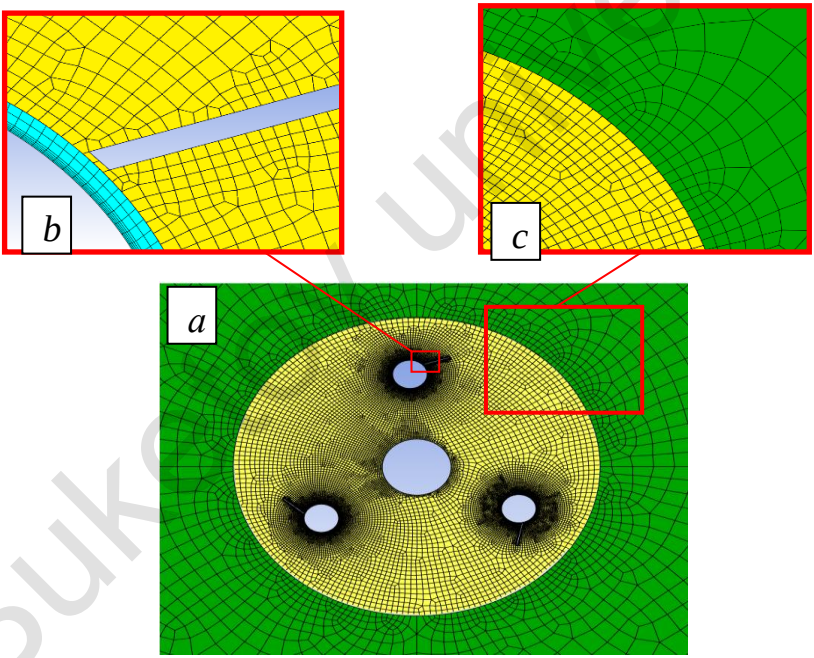

Fig.4.3. Grid area: a – general view of the grid area; b – the mesh view in the immediate proximity of the spinning cylinder and the blade; c – the mesh view near the interface of the spinning and fixed regions

The speed of the wind wheel rotation was determined by the following algorithm.

1. The moment of forces acting on the wind wheel is calculated as a function of time $M(t)$, for a given wind wheel rotation speed N.

2. The time mean value of the moment of forces for the time period T is calculated using the formula $\langle M \rangle = \frac{1}{T}\int_0^T M(t)dt$. The time-averaged moment of forces is a function of the wind wheel rotation speed: $\langle M \rangle = f(N)$.

3. The wind wheel rotation speed is assumed to be found if the average moment of forces $\langle M \rangle$ it is equal to zero. The search for the 3. The wind wheel rotation speed is reduced to solving a nonlinear equation $f(N)=0$.

4. Solving a nonlinear equation $f(N)=0$ it was implemented using the secant method (4.1):

$$N_{k+1} = N_k - \frac{f(N_k)}{f(N_k) - f(N_{k-1})}\left(N_k - N_{k-1}\right) \qquad (4.1)$$

4.2.2 The 6DOF method

To determine the wind wheel angular rotation speed, the rotation equation of a solid body is solved (4.2):

$$J\frac{d\omega}{dt} = \sum_{i=1}^{n} M_i, \qquad (4.2)$$

where J – wind wheel inertia moment, ω – wind wheel angular rotation speed, M_i – aerodynamic forces moments from the incoming flow, directed along the rotation axis, acting on the elements of the wind wheel (cylinders, blades), $\omega = 2\pi N$.

In the present calculations, the moment of inertia J of the WPP was assumed to be 2.5 kg·m^2. Moments of aerodynamic forces M_i

They are calculated by the Ansys-Fluent program based on the solution of the equations system (2.1)-(2.5).

4.3 The results of mathematical modeling of a vertical-axial wind power plant with three blades

Computations were performed for incoming flow velocities of 3 m/s, 9 m/s, 15 m/s and cylinder rotation speeds of 315 rpm, 550 rpm, 720 rpm.

The value of the averaging time period T was selected from 3 s to 5 s, which is significantly longer than the rotation period of the cylinders around its axis at the smallest rotation speed of 315 rpm. To determine the wind wheel rotation speed according to the formula (4.2), it was required to perform from 2 to 4 iterations.

Figure 4.4 indicates dependence of the moment of forces M(t) acting on the wind wheel on time for the incoming flow velocity of 9 m/s and the wind wheel rotation speed of 120 rpm. This dependence is periodic in nature. The period of change of the moment of forces T, shown in Fig. 4.4, is 0.5 m/s, which corresponds to 2 rpm of the WPP. As defined from Fig.4.4 *a) - c),* the cylinder rotation frequency in the range from 315 rpm to 720 rpm does not affect the period of change in the torque of forces, but the amplitude of the torque of forces increases with decreasing rotational speed. The presence of four peaks depending on M(t) in one period T is apparently due to the influence of rotating cylinders and a central support.

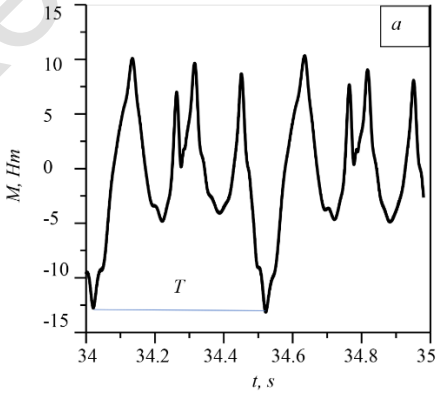

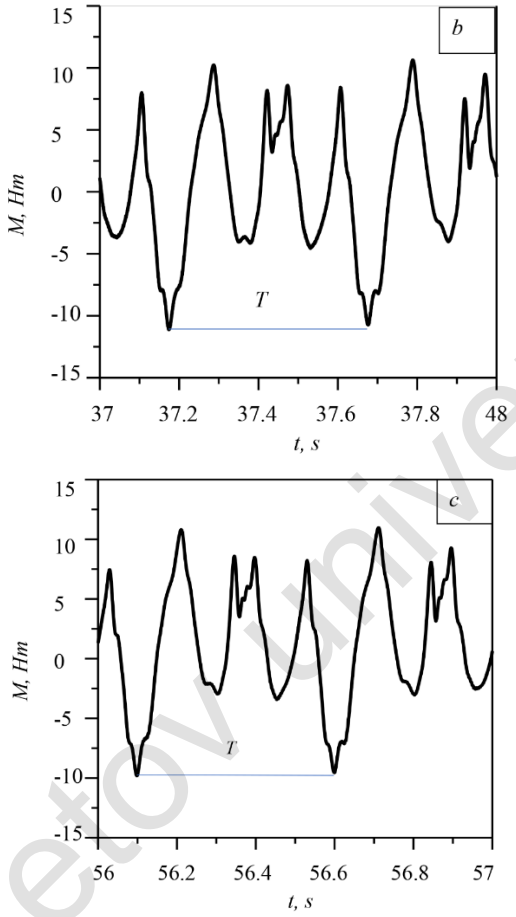

Fig.4.4. Dependence of the moment of forces on time
N = 120 rpm, V = 9 m/s;
a – n =315 rpm, b – 550 rpm, c – 720 rpm

In Fig.4.5 the the wind wheel rotation speed dependences on the velocity of the coming stream obtained for cylinder rotation speeds of 315 rpm, 550 rpm and 720 rpm are shown. The solid lines correspond to the results of a two–dimensional calculation model

using the sliding grid method, and the dotted lines correspond to the results of experiments.

As defined from the figure, the error in determining the wind wheel rotation speed for incoming flow velocities from 3 m/s to 7 m/s is 16% – 24% relative to the rotation speed obtained from the experiment. For incoming flow rate from 9 m/s to 15 m/s,the numerical model used gives an overestimated value of the wind wheel rotation speed by 1.5- 2 times.

As in the experiment, calculations demonstrate an improvement in the wind wheel rotation speed of the with an increase in the rotation speed of the cylinders.

In comparison with the experimental results, that indicate that an increase in the spin velocity of the wind wheel slows down with increasing wind speed, the calculation results give a dependence of the the wind wheel rotation speed depends on the velocity of the coming stream close to linear.

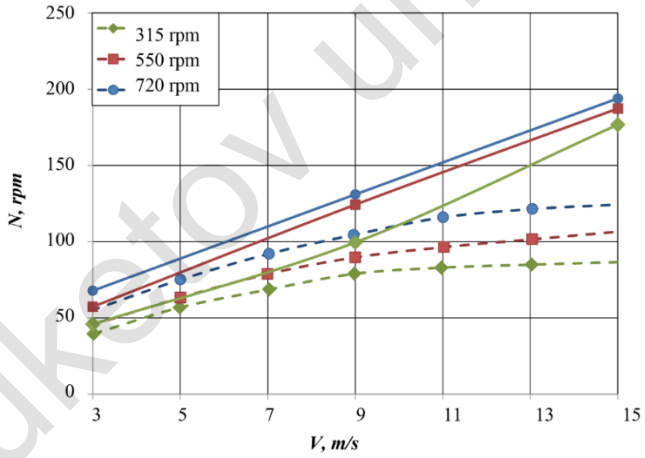

Fig.4.5. Dependence of the wind wheel rotation speed depends on the velocity of the coming stream. The sliding grid method

In Fig.4.6 the dependences of the wind wheel rotation speed on the incoming flow velocity are shown, obtained for cylinder rotation speeds of 315 rpm, 550 rpm and 720 rpm. The solid lines

correspond to the results of a two–dimensional calculation model using the 6DOF method, and the dotted lines correspond to the results of experiments.

As well as for the sliding grid method, the 6DOF method allows to obtain the wind wheel rotation speed with an error of 16% - 24% relative to the rotation speed obtained from the experiment for incoming flow velocities from 3 m/s to 7 m/s. For the incoming flow velocities of 11 m/s, 13 m/s and 15 m/s, the calculated speed of the wind wheel exceeds its experimental value by 1.5 – 2 times.

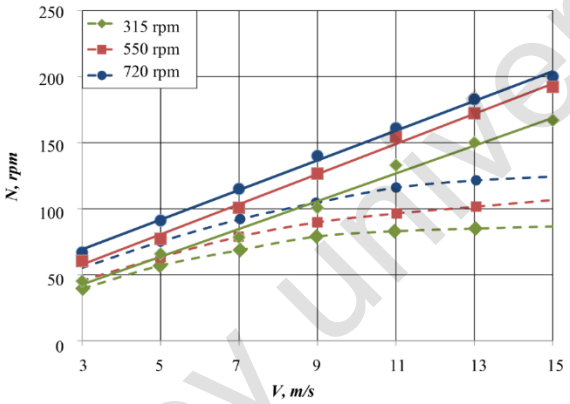

Fig.4.6. Dependence of the wind wheel rotation speed depends on the velocity of the coming stream. The 6DOF method

At a flow rate of 7 m/s, using the 6DOF and sliding grid methods, overestimated values of the rotation speed of the wind wheel were obtained. The explanation for this is the influence of the resistance of the retaining rods and the friction forces in the WPP bearings, which are not taken into account when performing the calculation.

Figure 4.7 demonstrates the dependence of the time-averaged longitudinal force acting on the wind wheel (cylinders and blades) on the velocity of the incoming stream. The time-averaged force value was calculated using the formula:

$$\langle F \rangle = \frac{1}{T} \int_0^T F(t)\,dt$$

The dependence of the averaged longitudinal force acting on the the wind wheel depends on the incoming stream speed and the cylinders rotation speed is approximated by the dependence

$$F_x = A(n)V^{B(n)},$$

where $A(n) = 7.3129 \cdot 10^{-4} n + 5.1188 \cdot 10^{-1}$; n – cylinder rotation speed, rpm; V – the incoming flow velocity, m/s; F_x – lengthwise force, N. $B(n) = -2.4259 \cdot 10^{-4} n + 1.9886$.

As determined from the simulation results of the longitudinal force acting on the wind wheel increases with increasing velocity of the incoming flow as a power function with an exponent close to 2. The cylinders rotation velocity of the slightly increases the longitudinal force acting on the wind wheel, according to the low, near linear, speed of the incoming stream, m/s.

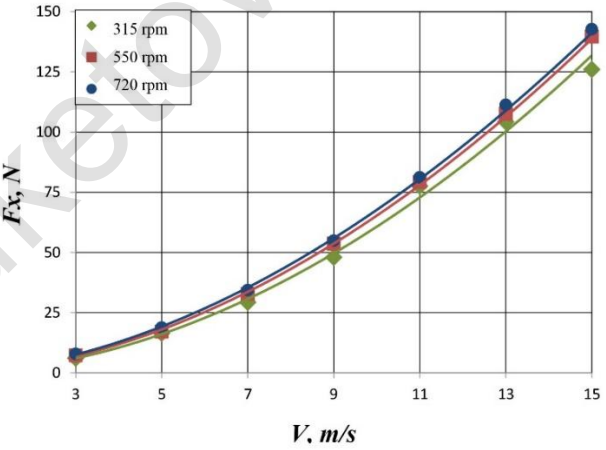

Fig. 4.7. Dependence of the longitudinal force acting on the wind wheel on the velocity of the incoming flow. The 6DOF method

Figure 4.8 demonstrates the time-averaged transverse force acting dependence on the velocity of the incoming flow.

The dependence of the averaged transverse force acting on the wind wheel depends on the velocity is approximated by the dependence:

$$F_y = C(n)V^{D(n)},$$

where

$C(n) = 3.1671 \cdot 10^{-3} n + 1.0115 \cdot 10^{-1}$; $D(n) = -3.6544 \cdot 10^{-4} n + 1.7281$;

n – cylinder rotation speed, rpm; V – incoming stream velocity, m/s; F_y – longitudinal force, N.

Like in the situation with longitudinal force, the dependence of the transverse force. The effect of the cylinder rotation speed on the transverse force acting on the wind wheel is stronger than on the longitudinal force.

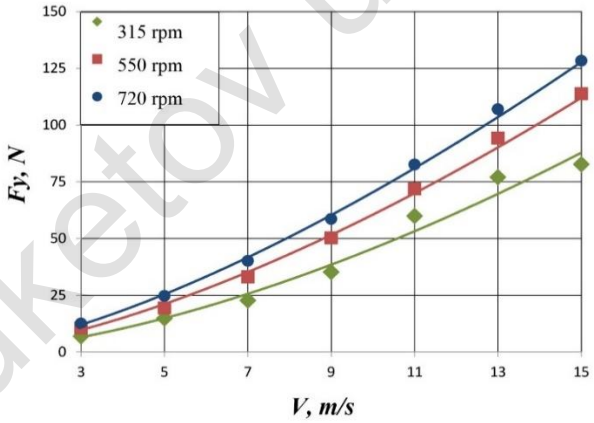

Fig.4.8. Dependence of the transverse force. The 6DOF method

Figures 4.9 – 4.10 show, respectively, the dependences of the time-averaged longitudinal and transverse forces on the velocity of the incoming flow. The qualitative behavior of these dependencies is the same as for the forces acting on the entire wind wheel.

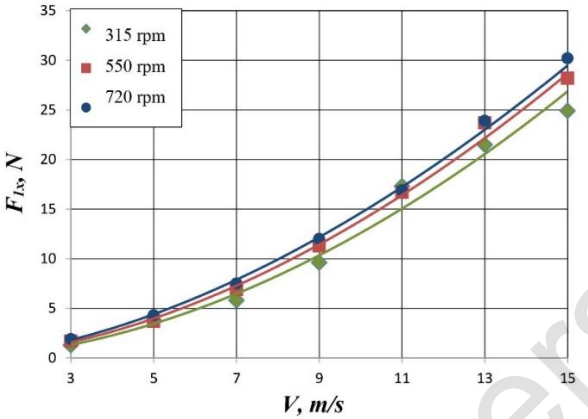

Fig.4.9. Dependence of the lengthwise force acting on the cylinder depends on the velocity of the incoming flow. The method of 6DOF

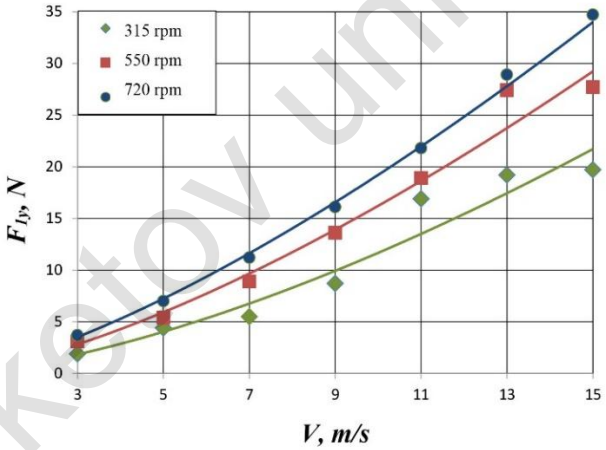

Fig.4.10. Dependence of the lateral force exerted on the cylinder depends on the speed of the oncoming stream. The method of 6DOF

In Fig.4.11 shows the air flow lines in the wind wheel vicinity for flow rates of 3 m/s, 9 m/s, 15 m/s and cylinder rotation speeds of 315 rpm and 720 rpm. The air flow moves from left to right. It is clearly visible that vortex areas are being formed in the vicinity of the blades. An increase in the cylinder rotation speed from 315 rpm

to 720 rpm for an incoming flow velocity of 3 m/s (Fig. 4.11 *a, d*) leads to more intense vortex formation, whereas at a higher flow velocity of 15 m/s, vortex formation is less pronounced (Fig. 4.11 *b, e*).

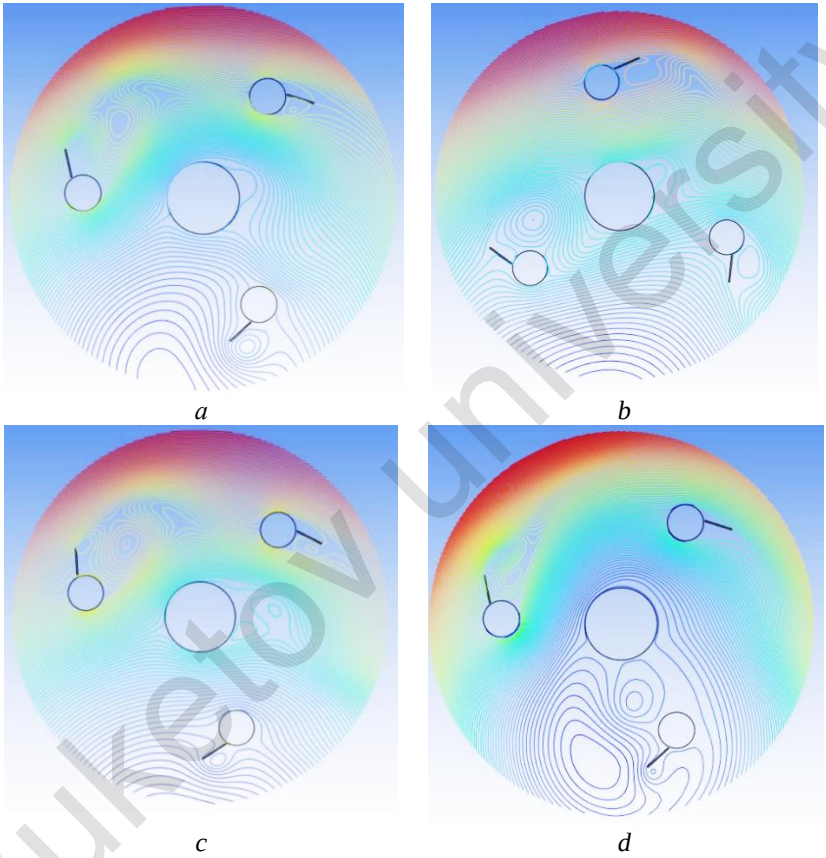

a *b*

c *d*

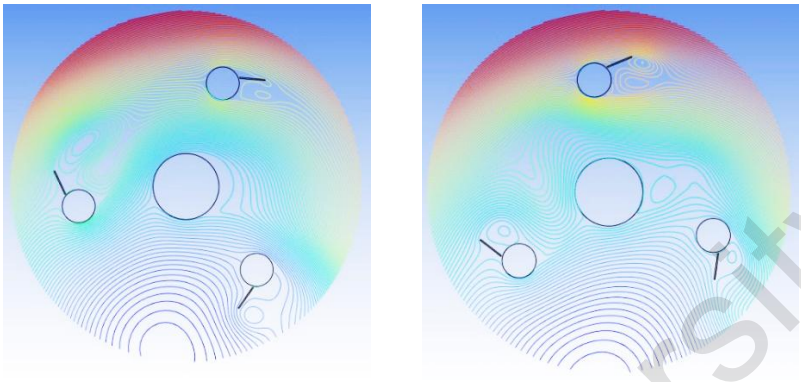

e *f*

Fig. 4.11. Current lines in the wind wheel vicinity
a, *b*, *c* – n=315 rpm, *d*, *e*, *f* – n=720 rpm
a, *d* – V=3 m/s, *b*, *e* – V=9 m/s, *c*, *f* – V=15 m/s

In Fig.4.12 shows the overpressure fields in Pascals. A value of 0 corresponds to 1 atm. A rise in the speed of the oncoming stream leads to an increase in in the pressure drop on the cylinders and blades of the wind wheel. The same effect is observed with a rise in the cylinders rotation velocity. Table 4.1 demonstrates the change in the pressure drop (the difference between the maximum and minimum overpressure) on the structural elements of the wind wheel.

Table 4.1
Pressure drop on the structural elements of the wind wheel, Pa.

N, rpm	3 m/s	9 m/s	15 m/s
315 rpm	62	330	1177
550 rpm	75	370	1541
720 rpm	105	444	1968

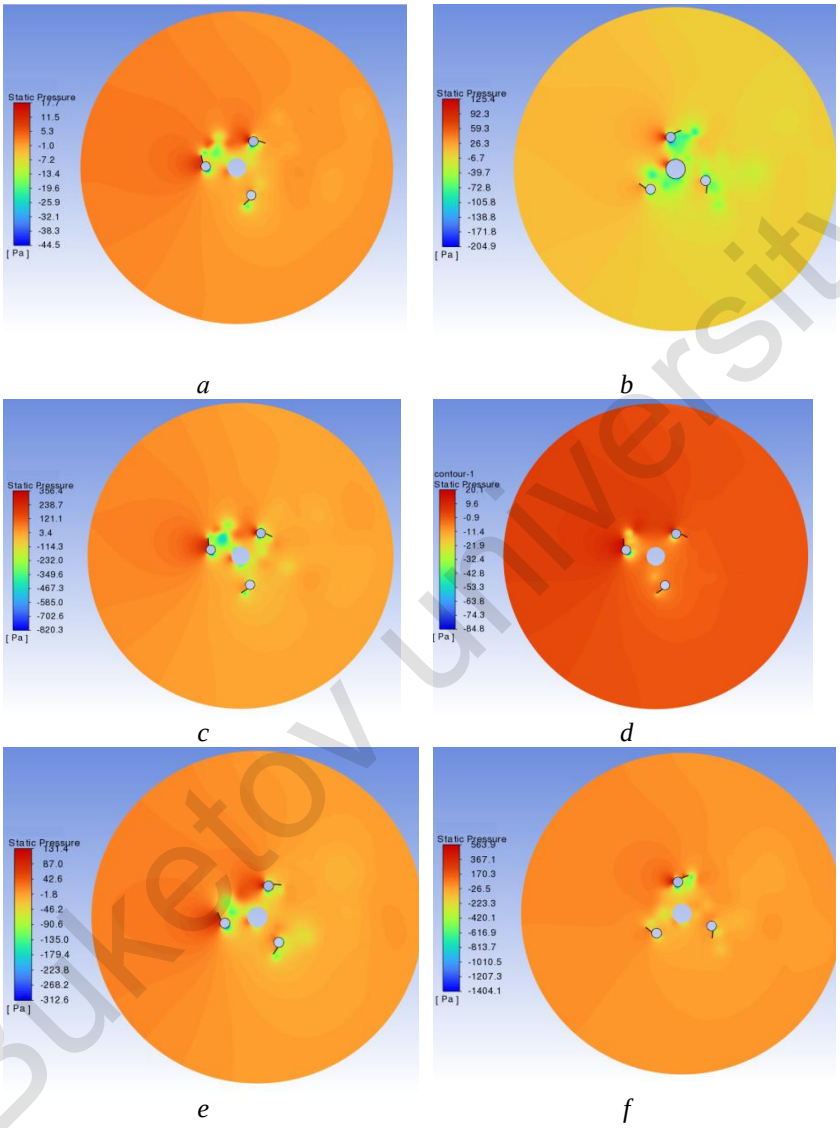

Fig. 4.12. The field of excess pressure: *a*, *b*, *c* – n=315 rpm, *d*, *e*, *f* -n=720 rpm, *a*, *d*-V=3 m/s, *b*, *e*-V=9 m/s, *c*, *f*-V=15 m/s

The calculation results show, Fig.4.12, that to the left of the cylinders, blades and supports, the pressure is increased due to the air flow running into them. In the wind wheel vicinity, areas with reduced pressure are formed, caused by the disruption of vortices from the blades of the wind wheel.

CONCLUSION

Numerical modeling was carried out in order to define the ideal inclination angle fixed blade relative to the cylinder. Preliminary modeling it was conducted using ANSYS WORKBENCH program. Using the COMPASS 3D program, the geometry of 4 blade variants with angles of 0, 30, 45 and 60 degrees was simulated. It is established that when the fixed blade is positioned relative to the cylinder at an angle of 0 degrees, the max lift coefficient value and the min drag coefficient value are obtained: 0.05 and 0.03, respectively. Based on this, in further calculations, a model with a fixed blade located an angle of 0 degrees with respect to the cylinder was employed.

Using the preprocessor of the Design Modeler program, a three-dimensional model of the blade profile was created for further calculation. The combined blade consists of a cylinder and a fixed blade mounted on both sides on a base in the form of a teardrop-shaped disk. To set the boundary conditions around the model under study, a cylindrical subdomain was created to set the rotation conditions. A parallelepiped has been created to simulate a wind tunnel around a cylindrical subdomain.

In the Ansys MESH creation routine, the operation of splitting the model into finite element grids was performed. 3 variants of grids with different numbers of cells were compared in order to define optimal grid in which minimal time resources were spent. A grid with a number of cells of 248723 was selected, which showed more accurate results of the lift coefficient at 9 m/s. The calculation grid consists of tetragonal cells. A Realizable k-ε with two Reynolds-averaged Navier-Stokes equations (RANS) was chosen as the model of turbulence. For the most accurate adjustment of the velocity and pressure fields, as well as to improve convergence, the algorithm of SIMPLE was used.

During numerical simulation at air speeds of 5, 10, 15 m/s and at a velocity of rotation of 300, 500, 700 rpm, three-dimensional patterns of airflow around the blade and the distribution of the pressure field were obtained. Three-dimensional flow patterns provide an explanation for the entire physico-aerodynamic process taking place around the model. From the results obtained, it was

showed that the combined blade produces an effective pressure value. The numerical results obtained will be useful in developing a a wind turbine model with a combined blade.

In the course of numerical studies, a 3D WPP model with two and three blades was created. The WPP model consists of combined blades, a central shaft on which the working power elements are fixed, as well as a mast on which the the major shaft is fixed motionless. To investigation of the inclination angle effect of the fixed blade on the aerodynamic parameters of the entire wind power plant, mathematical models with different positions of the fixed blade have been created (0°, 15°, 30°, 45°, 60°).

A system of formulas that describes the flow of air flowing through around the wind wheel is recorded. The Realizable k-ε turbulence model is chosen as the model. Boundary conditions are set at the entrance, at the exit of the area, as well as on the walls of the area.

A mathematical calculation of the WPP aerodynamic parameters with horizontal axis of rotation under different flow regimes has been performed. The maximum value of 2.1 N thrust force at 12 m/s was obtained when the fixed blade relative to the cylinder was positioned at an angle of 0°. There is a decrease in the thrust force in the range of 0.1-0.05 N, with an increase in the angle by 15 degrees.

A graph of the dependence of the moment of forces acting on a movable wind turbine with two and three blades on the velocity of the incoming flow is constructed. The dependence of the WEUC on the speed (speed coefficient) for two and three-bladed wind turbines is obtained. It was found that the WEUC of a three-bladed wind turbine is almost 7-8% greater than that of a wind turbine with two blade. The speed of wind turbine with three blade is 6-7% lower than a two-bladed one. It is established that each speed value corresponds to a certain value of the wind energy utilization coefficient.

The patterns of the distribution of velocity vectors around a rotating wind wheel with two and three blades at a fixed blade position of 0 and 30 degrees are obtained. When the fixed blade is positioned at an angle of 30 degrees, the flow is disrupted, that is well apparent at the max rotation speed of the blades and the wind wheel. Due to which, a drop in lift is observed, which leads to a

decrease in the wind turbine efficiency. Based on this, the favorable angle of the fixed blade is an angle of 0 degrees for two-bladed and three-bladed wind turbines. The patterns of pressure distribution around a rotating wind wheel with a fixed blade at 0 and 30 degrees are obtained. When the blade is positioned at an angle of 30 degrees due to unfavourable pressure gradient, boundary layer is torn off due to braking of the wind wheel. As a result, it was determined that the location of the fixed blade at an angle of 0 degrees for the entire wind wheel is favorable for obtaining optimal aerodynamic performance of all wind turbines.

A method for solving systems of equations to describe a wind wheel containing cylindrical blades has it was created. On the basis of method developed for modeling the parameters of a wind wheel, using well-known theoretical provisions, a mathematical calculation model based on the dependence of the equation was developed. It is characterized by taking into account the walls movement velocity, depending on the rotation velpcity of the working cylinders around their own vertical axis, as well as the speed of rotation of the cylinders around the wind generator axis . Thanks to this, it is possible to fully reproduce the wind turbines aerodynamics in the numerical section is based on the Magnus effect. Contrary to the existing equations, conventional winged wind turbines are mainly described.

A numerical model was created results of changes in the moment of forces and rotation frequency depending on the wind speed are obtained. The time of change of the moment of force T corresponds to 2 revolutions of the the speed of rotation of the wind wheel in a minute. This occurrence is attributed to the following to the shape of the wind wheel in question and the presence of three combined blades, this leads to deviations from uniform rotation: the wind wheel sometimes accelerates slightly to the maximum value during rotation and slows down to a value that is explained by the effect of the rotating cylinder and the central support.

Computational modeling of a three combined bladed WPP demonstrates the the aerodynamic properties dependence of the turbine on the wind velocity and the angle of rotation of the turbine, as well as alterations in the geometric sizes that define the design of the turbine. The suggested method help to define the optimal rotation

conditions, as well as to calculate the amplitudes of the torque pulses of the wind turbine depends on the angular speed of rotation, the wind speed is taking into account on the model of wind turbines.

Depending on the wind wheel rotation speed, on the velocity of the oncoming stream, it turns out that at a wind speed of at least 3 m/ s, the wind wheel produces 50 revolutions per minute, exceeding conventional wind turbines operating on the the base of Magnus effect by almost 7-10% thanks to the use of wind turbines.

A distinctive feature of the earlier famous advancements of this method were possibility of studying active operating modes that allow you to optimally configure the control system to improve efficiency of both wind turbines with combined blades and hybrid plants in general.

The obtained theoretical data can be applied in the design and WPP construction with combined blades, which work more effectively, in contrast to other types of wind turbines with winged and cylindrical blades, at low speeds of incoming air flow..

For the first time, the obtained the result of numerical simulation of WPP with combined blades, which are presented in this monograph, are an important step and the basis for further research of wind turbines with other configurations and shapes of blades and wind wheels.

List of literature

1. Belov I. A., Isaev S. A. Modeling of turbulent flows: Uch. pos. – St. Petersburg: Baltic State Technical University. Univ., 2001. – 108 p., ill.
2. Plykin M. Creation of prismatic layers and grid optimization in ANSYS ICEM CFD // ANSYS Solutions. Russian edition. - 2006. – No.2. – pp. 31-34.
3. Plykin M. Construction of a hexahedral grid in ANSYS ICEM CFD. Part 2 // ANSYS Solutions. Russian edition. - 2007. – No.4. – pp. 48-51.
4. Patankar S. Numerical methods for solving problems of heat transfer and fluid dynamics: Trans. from English. – M.: Energoatomizdat, 1984. – 152 p., ill.
5. Roach P. Computational fluid Dynamics. – M.: Mir, 1980. – 616p., ill.
6. Stankova E. N., Zatevakhin M. A. Multigrid methods. An introduction to standard methods. – St. Petersburg: Institute of High-Performance Computing and Information Systems, 2003. – 47 pFletcher K. Computational methods in fluid dynamics: In 2 volumes: Vol. 1: Translated from English – M.: Mir, 1991. – 504 p, ill.
7. Fletcher K. Computational methods in fluid dynamics: In 2 volumes: Vol. 2: Translated from English – M.: Mir, 1991. – 552 p, ill.
8. Tricky D., Plykin M. Module Pre/Post ANSYS CFX // ANSYS Solutions. Russian edition. - 2006. – No. 2. – pp. 24-30
9. Advisory Report No. 138 (AGARD-AR-138). Experimental Data Base for Computer Program Assessment. Report of the Fluid Dynamics Panel Working Group 04. - Advisory Group for Aerospace Research and Development, NATO. – 1979. – 642 p.
10. Chung T. J. Computational Fluid Dynamic. – Cambridge: Cambridge University Press, 2002. – 1021 p.
11. Ferziger J. H., Perić M. Computatational Methods for fluid Dynamics. – 3., rev. ed. – Berlin: Springer, 2002. – 423 p.
12. Versteeg H. K., Malalasekera W. An Introduction to Computational Fluid Dynamics. The finite volume method. – London: Longman Scientific & Technical, 1995. – 252 p.
13. ANSYS ICEM CFD v.11. Release. Help manual.
14. ANSYS CFX v.10. Release. Theory Reference.
15. Calautit K. et al. A review of numerical modelling of multi-scale

wind turbines and their environment //Computation. – 2018. – V. 6. – No. 1. – P. 24.
16. Ayhan D., Sağlam Ş. A technical review of building-mounted wind power systems and a sample simulation model //Renewable and sustainable energy reviews. – 2012. – V. 16. – No. 1. – P. 1040-1049.
17. De Santoli L. et al. A preliminary energy and environmental assessment of a micro wind turbine prototype in natural protected areas //Sustainable Energy Technologies and Assessments. – 2014. – V. 8. – P. 42-56.
18. El-Zahaby A. M. et al. CFD analysis of flow fields for shrouded wind turbine's diffuser model with different flange angles //Alexandria Engineering Journal. – 2017. – V. 56. – No. 1. – P. 171-179.
19. Manatbayev R. et al. Numerical simulations on static Vertical Axis Wind Turbine blade icing //Renewable Energy. – 2021. – V. 170. – P. 997-1007.
20. Li J. et al. Numerical simulation and application of noise for high-power wind turbines with double blades based on large eddy simulation model //Renewable Energy. – 2020. – V. 146. – P. 1682-1690.
21. Eltayesh A. et al. Experimental and numerical investigation of the effect of blade number on the aerodynamic performance of a small-scale horizontal axis wind turbine //Alexandria Engineering Journal. – 2021. – V. 60. – No. 4. – P. 3931-3944.
22. Mdouki R. Parametric Study of Magnus Wind Turbine with Spiral Fins using BEM Approach //Journal of Applied Fluid Mechanics. – 2020. – V. 14. – No. 3. – P. 887-895.
23. Massaro D. et al. Direct numerical simulation of the turbulent flow around a Flettner rotor //Scientific Reports. – 2024. – V. 14. – No. 1. – P. 3004.
24. Marzuki O. F. et al. Magnus wind turbine: the effect of sandpaper surface roughness on cylinder blades //Acta Mechanica. – 2018. – V. 229. – P. 71-85.
25. Khadir L., Mrad H. Numerical investigation of aerodynamic performance of darrieus wind turbine based on the magnus effect //The International Journal of Multiphysics. – 2015. – V. 9. – No. 4. – P. 383-396.
26. Lopez N. et al. Design of modified Magnus wind rotors using computational fluid dynamics simulation and multi-response optimization //Journal of Renewable and Sustainable Energy. –

2015. – V. 7. – No. 6.
27. Jureczko M., Pawlak M., .Mężyk A. Optimization of wind turbine blades // Journal of Materials Processing Technology. –2005. – Volume 167. – Issues 2–3. –P. 463-471.
28. Balat M. A Review of Modern Wind Turbine Technology // Energy Sources, Part A: Recovery, Utilization, and Environmental Effects. –2009. –Volume 31 (17) . –P.1561-1572, DOI: 10.1080/15567030802094045
29. Moh M., Saad M., Asmuin N.. Comparison of Horizontal Axis Wind Turbines and Vertical Axis Wind Turbines // IOSR Journal of Engineering (IOSRJEN) . –2014. –Vol. 04. –Issue 08. –P.27-30
30. Tanasheva N.K., Bakhtybekova A.R., Shaimerdenova K.M., Sakipova S.E., Shuyushbaeva N.. Modeling aerodynamic characteristics of a wind energy installation with rotating cylinder blades on the basis of the Ansys suite // Journal of Engineering Physics and Thermophysics. –2022. –95(2). –P. 457–463.
31. Sanusi A., Soeparman S., Wahyudi S., Yuliati L.. Experimental Study of Combined Blade Savonius Wind Turbine // International journal of renewable energy research. –2016. –Vol. 6, No. 2.
32. Dyusembaeva A.N., Tleubergenova A. Zh., Tanasheva N.K., Nussupbekov B.R., Bakhtybekova A.R., Kyzdarbekova Sh.S. Numerical investigation of the flow around a rotating cylinder with a plate under the subcritical regime of the Reynolds number // International Journal of Green Energy. – 2023. – Vol.21. – Issue 5. – P.973-987.
33. Tleubergenova A.Zh., Dyusembaeva A.N., Tanasheva N.K., Minkov L.L., Mukhamedrakhim A.R. Investigation of aerodynamic thrust force of the wind power plant combined blades // Eurasian Physical Technical Journal. – 2023. – Vol.20. – Issue 2(44). – P.65-69.
34. N. K., Bakhtybekova A.R., Shuyushbaeva N. N., Tusupbekova A. K., Tleubergenova A. Zh. Calculation of the aerodynamic characteristics of a wind-power plant with blades in the form of rotating cylinder // Technical Physics Letters. –2022. – No. 2 (22).
35. Tanasheva N.K., Chirkova L.V., Dyusembaeva A.N., Sadenova K.K. Aerodynamic Characteristics of a Rotating Cylinder in the Form of a Truncated Cone // Journal of Engineering Physics and Thermophysics. – 2020. – 93(3) . –P. 551–555
36. A.Zh. Tleubergenova, A.N. Dyusembayeva, N.K. Tanasheva, Sh.S. Kyzdarbekova, A.R. Mukhamedrakhim. Analysis of aerodynamic characteristics of a two-bladed wind power plant

containing combined power elements // Bulletin of the Karaganda University. – Physics Series. – 2023. – №3(111). – P. 143-150.
37. Tanasheva, N., Tleubergenova, A., Dyusembaeva, A., Satybaldin, A., Mussenova, E., Bakhtybekova, A., Shuyushbayeva, N., Kyzdarbekova, S., Suleimenova, S., Tussypbayeva, A. Determination of the aerodynamic characteristics of a wind power plant with a vertical axis of rotation // Eastern-European Journal of Enterprise Technologies. – 2023. - Vol.2. - No.8 (122). - P.- 36–43.
38. Kornilov V. I., Lysenko V. I. Investigation of aerodynamic characteristics of cylindrical bodies in supersonic gas flow // Bulletin of the NSU. Physics series. – 2011. – Volume 6. – Issue 4. – pp.16-24.
39. Tanasheva N.K., Shuyushbaeva N.N., Musenova E.K. Investigation of the dependence of the aerodynamic characteristics of rotating cylinders on the angle of bevel of the air flow // Journal of Technical Physics. – 2018. – 44.
40. Antar E. et al. A Dynamic Rotor Vertical-Axis Wind Turbine with a Blade Transitioning Capability // Energies. – 2019. – Vol. 12. – P. 1-21.
41. Khoziainov B.P. Calculation of the angular velocity of rotation of a wind turbine with a vertical axis // Energetik. – 2011. – No.5. – pp. 28-30.
42. Kusaiynov K.K., Dyusembina A.G., Turgunov M.M., etc. Investigation of aerodynamic parameters of an installation for creating a wind flow in an open space // Bulletin of the Karaganda University. – 2016. – №1(81). – Pp. 57-61.
43. Kusaiynov K., Turgunov M., Dyusembayeva A. Investigation of the drag of a two-bladed wind turbine in operating mode // Bulletin of the Tomsk State University. – 2014. – №4(30). – Pp. 82-88.
44. Kusaiynov K., Kambarova Zh.T., Alibekova A.R., etc. Calculation of the drag force and lifting force of prototypes of wind turbine blades with a dynamically variable shape // Science, education and production – leading factors of the Strategy "Kazakhstan– 2050": tr. international scientific and practical conference - Karaganda, 2014. – pp. 277-280.
45. Kusaiinov K., Shrager E.R., Dyusembayeva A. et al. Experimental study of the drag force of a wind turbine layout in operating mode// Bulletin of Karaganda University. – 2014. – №3(75). – Pp. 47-52.
46. Tanasheva N.K., Nusupbekov B.R., Dyusembayeva A.H., etc. The study of the occurrence of the lifting force of a rotating cylinder //

"Alikhanov readings – 22: sat. mater. International Scientific and Practical Conference – Kokshetau, 2018. – pp. 149-152.
47. Kusaiynov K., Alibekova A.R., Kusaiynov E.K. Aerodynamic parameters of a wind turbine blade with a dynamically variable shape of the working surface // Bulletin of Karaganda University. – 2014. – №3(75). – Pp. 52-57.
48. Tanasheva N.K., Dyusembayeva A.N., Bagdatova S.B., etc. Investigation of the aerodynamic characteristics of rotating cylinder systems based on the Magnus effect // EXPO-2017: technologies of the future: Republic Scientific and Practical Conference – Karaganda, 2016. – pp. 41-46.
49. Bachant P., Wosnik M. Performance measurements of cylindrical- and spherical-helical cross-flow marine hydrokinetic turbines, with estimates of exergy efficiency, Renew // Energy. – 2015. – Vol. 74. – P. 318-325.
50. Levitsky I.A. Mathematical modeling of gas dynamics and heat transfer in industrial furnaces: application of Ansys Fluent for modeling gas dynamics and heat transfer. – M.: NUST, 2019. – 274 p.
51. Ouro P., Stoesser T. An immersed boundary-based large-eddy simulation approach to predict the performance of vertical axis tidal turbines // Comput. Fluids. – 2017. – Vol. 152. – P. 74-87.
52. Tahani M., Rabbani A., Kasaeian A. et al. Design and numerical investigation of Savonius wind turbine with discharge flow directing capability // Energy. – 2017. – Vol. 130. – P. 327-338.
53. Kumar P.M., Kulkarni R., Srikanth N. et al. Performance Assessment of Darrieus Turbine with Modified Trailing Edge Airfoil for Low Wind Speeds // Smart Grid Renew. – 2017. – Vol. 8. – P. 425-439.
54. Asr M.T., Nezhad E.Z., Mustapha F. et al. Study on start-up characteristics of H-Darrieus vertical axis wind turbines comprising NACA 4-digit series blade airfoils // Energy. – 2016. – Vol. 112. – P. 528-537.
55. Elkhoury M., Kiwata T., Aoun E. Experimental and numerical investigation of a three-dimensional vertical-axis wind turbine with variable-pitch // J. Wind Eng. Ind. Aerodyn. – 2015. – Vol. 139. – P. 111-123.
56. Hu R., Wang L., Fu S. Improved Delayed Detached Eddy Simulation of Flow Structures behind A Backward-Facing Step // Procced. 54th AIAA Aerospace Sciences Meeting. – Reston: American Institute of Aeronautics and Astronautics, 2016. – 1104 p.

57. Lei H., Zhou D., Bao Y. et al. Three-dimensional Improved Delayed Detached Eddy Simulation of a two-bladed vertical axis wind turbine // Convers. Manag. – 2017. – Vol. 133. – P. 235-248
58. Li C., Zhu S., Xu Y.-L. et al. 2.5 D large eddy simulation of vertical axis wind turbine in consideration of high angle of attack flow // Renew. Energy. – 2013. – Vol. 51. – P. 317-330.
59. Yemelyanova S.V. Information technologies and computing systems: mathematical modeling. Computer systems. Nanotechnology. Applied aspects of computer science. – M.: Lenand, 2012. – 108 p.
60. Zolotareva D.A., Kravtsova K.E. Development of methodological recommendations for modeling paraboloids and hyperboloids using the Compass-3D program // Engineering graphics and three-dimensional modeling: young. scientific and practical conference – Novosibirsk: SGUGiT, 2017. – pp. 26-38.
61. Loseva E.S., Simakov E.E. Investigation of the properties of surfaces of rotation using modeling in CAD "Compass" // Young scientist. – 2017. – №3(12). – Pp. 6-18.
62. Yemelyanova S.V. Information technologies and computing systems: information processing and data analysis. Software engineering. Mathematical modeling. Applied aspects of computer science. – M.: Lenand, 2015. – 104 p.
63. Yemelyanova S.V. Information technologies and computing systems: mathematical modeling. Internet technologies. Computer graphics. Intelligent text analysis. Applied aspects of computer science. Bioinformatics and medicine. – M.: Lenand, 2013. – 104 p.
64. Tande J.J. CFD Study of a 10 MW Offshore Horizontal Axis Wind Turbine Blade. – Trondheim: NTNU, 2011. – 117 p.
65. Zwierzchowski J., Laski P.A. et al. Model tests of wind turbine with a vertical axis of rotation type Lenz // EPJ Web of Conferences. – 2017. – Vol. 143. – P. 02150.
66. Rezaeiha A., Kalkman I., Blocken B. CFD simulation of a vertical axis wind turbine operating at a moderate tip speed ratio: Guidelines for minimum domain size and azimuthal increment // Renew. Energy. – 2017. – Vol. 107. – P. 373-385.
67. Ferrari G., Federici D., Schito P. et al. CFD study of Savonius wind turbine: 3D model validation and parametric analysis // Renew. Energy. – 2017. – Vol. 105. – P. 722-734.
68. Balduzzi F., Bianchini A., Maleci R. et al. Critical issues in the CFD simulation of Darrieus wind turbines. Renew. Energy 2016,

85, 419–435.
69. Stefania Castelletto, Albert Boretti. Simulations of energy storage requirements of wind energy facilities // Energy Storage. – 2021. – Vol. 3. – P. 1-11.
70. Bazilevs Y., Korobenko A., Deng X. et al. Fluid–structure interaction modeling of vertical-axis wind turbines // Journal of Applied Mechanics. – 2014. – Vol. 81(8). – P. 821-833.
71. Maıtre T., Amet E., Pellone C. Modeling of the flow in a Darrieus water turbine: Wall grid refinement analysis and comparison with experiments // Renew. Energy. – 2013. – Vol. 51. – P. 497-512.
72. Wenehenubun F., Saputra A., Sutanto H. An Experimental Study on the Performance of Savonius Wind Turbines Related With The Number Of Blades // Energy Procedia. – 2015. – Vol. 68. – P. 297-304.
73. Ali M.H. Experimental Comparison Study for Savonius Wind Turbine of Two and Three Blades at Low Wind Speed // Int. J. Modern Eng. Research. – 2013. – Vol. 3, Issue 5. – P. 2978-2986.
74. Roy S., Saha U.K. Wind tunnel experiments of a newly developed two-bladed Savonius-style wind turbine // Applied Energy. – 2015. – Vol. 137(1). – P. 117-125.
75. Shaha S.R., Kumarb R. et al. Design, modeling and economic performance of a vertical axis wind turbine // Energy Reports. – 2018. – Vol. 4. – P. 619-623.
76. Belov N.N., Kopanitsa D.G., Yugov N.T. Mathematical modeling of the dynamic strength of structural materials: textbook – M.: DIA, 2013. – 562 p.
77. Vysotsky L.I., Copernicus G.R., Vysotsky I.S. Mathematical and physical modeling of potential fluid flows: textbook – St. Petersburg: Lan, 2014. – 64 p.
78. Sonki S.M. Mathematical and physical modeling of potential fluid flows: textbook – St. Petersburg: Lan, 2014. – 64 p.
79. Formalev V.F., Kolesnik S.A. Mathematical modeling of conjugate heat transfer between viscous gas-dynamic flows and anisotropic bodies. – M.: Lenand, 2019. – 316 p.
80. Yaglom I.M. Mathematical structures and mathematical modeling. – M.: Lenand, 2018. – 144 p.
81. Burlando M., Ricci A., Freda A. et al. Numerical and experimental methods to investigate the behaviour of vertical-axis wind turbines with stators // Journal of Wind Engineering and Industrial Aerodynamics. – 2015. – Vol. 144. – P. 125-133.
82. Shahzad A., Asim T., Mishra R. et al. Performance of a Vertical

Axis Wind Turbine under Accelerating and Decelerating Flows // Procedia CIRP. – 2013. – Vol. 11. – P. 311-316.
83. Park K.S., Asim T., Mishra R. Computational Fluid Dynamics based fault simulations of a Vertical Axis Wind Turbine // Journal of Physics. – 2012. – Vol. 364. – P. 250-256.
84. Kumara R., Raahemifarb K., Fung A.S. A critical review of vertical axis wind turbines for urban applications // Renewable and Sustainable Energy Reviews. – 2018. – Vol. 89. – P. 281-291.

Scientific publication

Dyusembaeva Ainura Nurtaevna

MATHEMATICAL MODELING OF WIND POWER PLANTS WITH COMBINED BLADES

Monograph

ISBN 978-601-7611-21-7

9 786017 611217

Printed from the author's original
Signed to the press on 10.09.2024
The paper size is 60x84 1/16.
The Times headset.
Volume 6.67 p.l. Circulation 500 copies.

010000, Astana, Qaramende bi Shaqauly str., 4.
Published by Altyn Kitap
Tel. +77025485841.
E-mail: altynkitap@mail.ru